5
Multipass-Tungsten Inert Gas (M-TIG) Welding Technique

This chapter deals with the use of different filler metals to fabricate the dissimilar weld joint (DWJ) between P91 steel and Incoloy 800HT using a multipass-tungsten inert gas welding (M-TIG) process. Also, optimal filler metals are used in successfully utilizing the buttering layer welding technique to fabricate the same DWJ.

5.1 USING AWSER90S–B9 FILLER (P91)

5.1.1 Macroscopic Observations

The fabricated DWJ is shown in Figure 5.1(a). The macroscopic image of the weld bead cross-section is shown in Figure 5.1(a). The heat affected zone (HAZ) was found to be around 8.15 mm wide. The DWJ fabricated was defect-free.

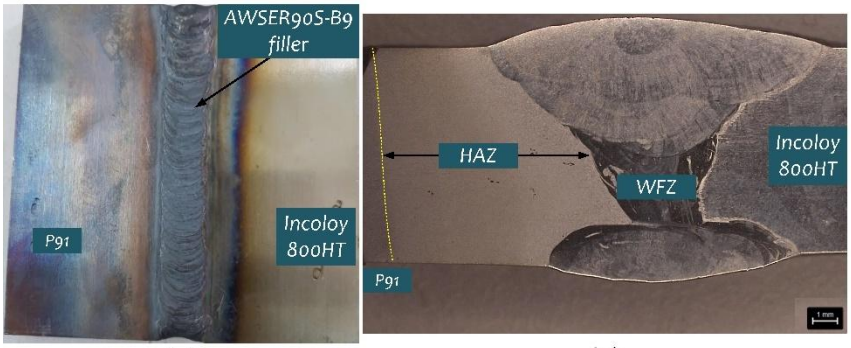


Figure 5.1 : (a) Welded plate (b) weld bead macrograph

5.1.2 Weld Interface and Weld Fusion Zone (WFZ) Microstructure Characterization

The weld interface characterization is crucial as the weld interface reflects on the solidification of weld metal and the strength of the joint. In Figure 5.2(a) P91 weld interface observed under an optical microscope was in the AW state. The P91 weld interface seems to be sharp and free of macrosegregation. The welding with similar AWSER90S-B9 filler metal has smoothly provided a proper mixing and solidification of weld metal at the interface. In WFZ, quenched martensite laths are witnessed. Also, near the weld interface, directional growth and solidification of martensitic lath might have occurred, differentiating the microstructure at the P91 weld interface.

In contrast, the Incoloy 800HT weld interface in the AW state is observed with improper mixing near the Incoloy 800HT weld interface with the visible formation of a partially mixed zone (PMZ) in Figure 5.2(b). The P91 and Incoloy 800HT have a difference in their coefficient of thermal expansion (CTE), which causes a chemical potential gradient, and a C-enriched PMZ is formed due to the migration of carbon (DuPont et al., 2018). After PWHT in Figure 5.2(c), heavy precipitation of C-rich precipitates was found in the P91 weld interface region. Figure 5.2(d) micrograph of Incoloy 800HT weld interface after PWHT depicts heavy precipitation of fresh C-rich precipitates near the weld interface. Figure 5.2(d) shows

prominent grain growth following recrystallization under high welding temperatures in Incoloy 800HT HAZ adjacent to the weld interface. Also, it can be observed that precipitates dissolved during the welding resurfaced dominantly on grain boundaries. Similar observations were made by (Sireesha et al., 2005) in alloy 800 HAZ of a dissimilar metal weld. In Figure 5.2(d), a small unmixed zone/island, which is a type of macrosegregation, is witnessed near the thick weld interface formed at the Incoloy 800HT side.

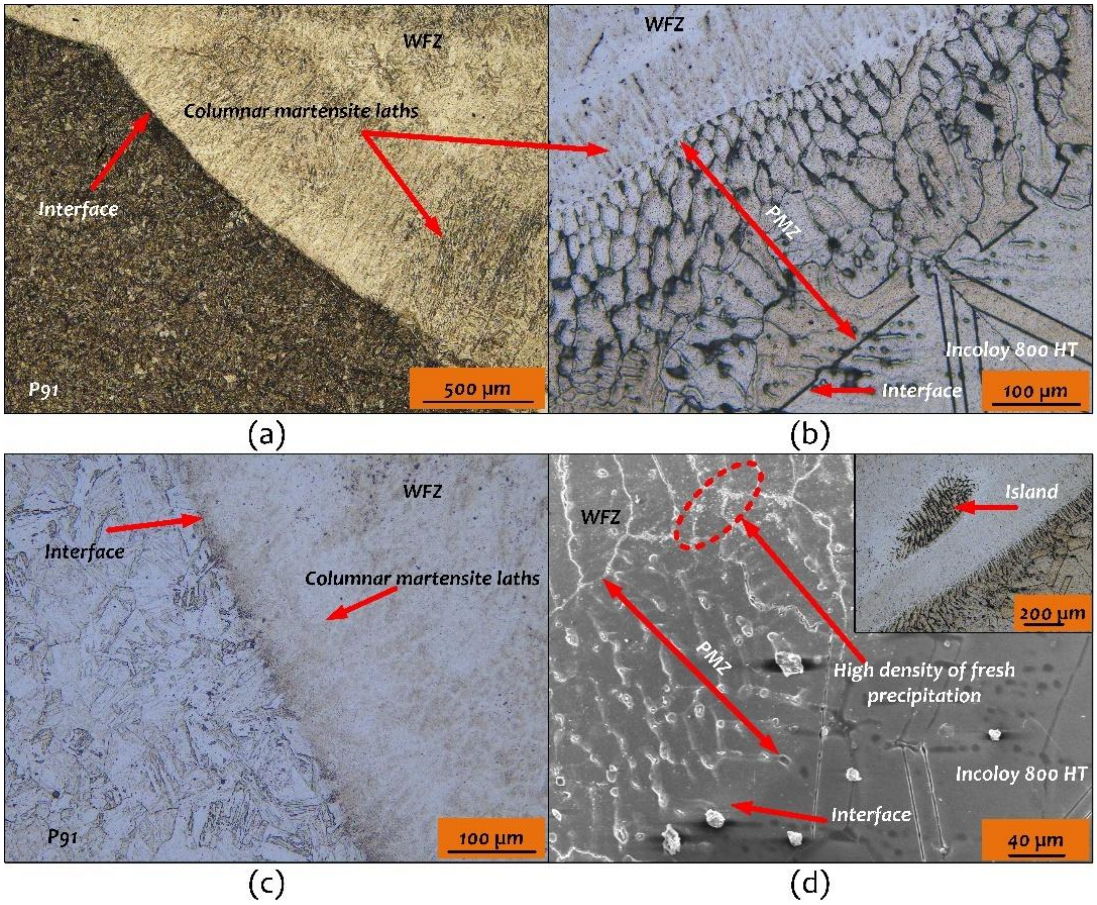


Figure 5.2 : (a) Optical image of P91 weld interface in AW state (b) optical image of Incoloy 800HT weld interface in AW state (c) optical image of P91 weld interface in PWHT state (d) SEM image of Incoloy 800HT weld interface in PWHT state

Further line mapping across the weld interfaces in the AW state was performed. The line mapping was done to trace the variation of compositional elements across the weld. In Figure 5.3(a), the P91 weld interface had a smooth and minimum variation in the composition of elements across the interface with no abnormality or sudden change. Since P91 steel and AWSER90S-B9 filler metal share a similar composition, it eliminates the possibility of heavy diffusion or microsegregation of elements across the weld interface. Figure 5.3(b) traces the elements across the Incoloy 800HT weld interface along with the formed PMZ. The weld interface on the Incoloy 800HT side has diffusion and heavy variation of elements across it. The diffusion of elements across the PMZ zone formed near the Incoloy 800HT weld interface can also be seen. The elemental density of Fe was found higher in the WFZ compared to Incoloy 800HT HAZ, while Ni and Cr density was higher on the Incoloy 800HT side, owing to the base metal composition differences between them. The PMZ seems to be Cr and Ti-depleted and C-enriched. C percentage is slightly higher in PMZ due to the chemical potential of the carbon gradient caused by the CTE mismatch. Ti depletion could have to be accounted for the Ti deposition on grain boundaries of Incoloy 800HT. The Nb and Mo distribution across the weld interface on the Incoloy 800HT side was almost uniform and unchanged.

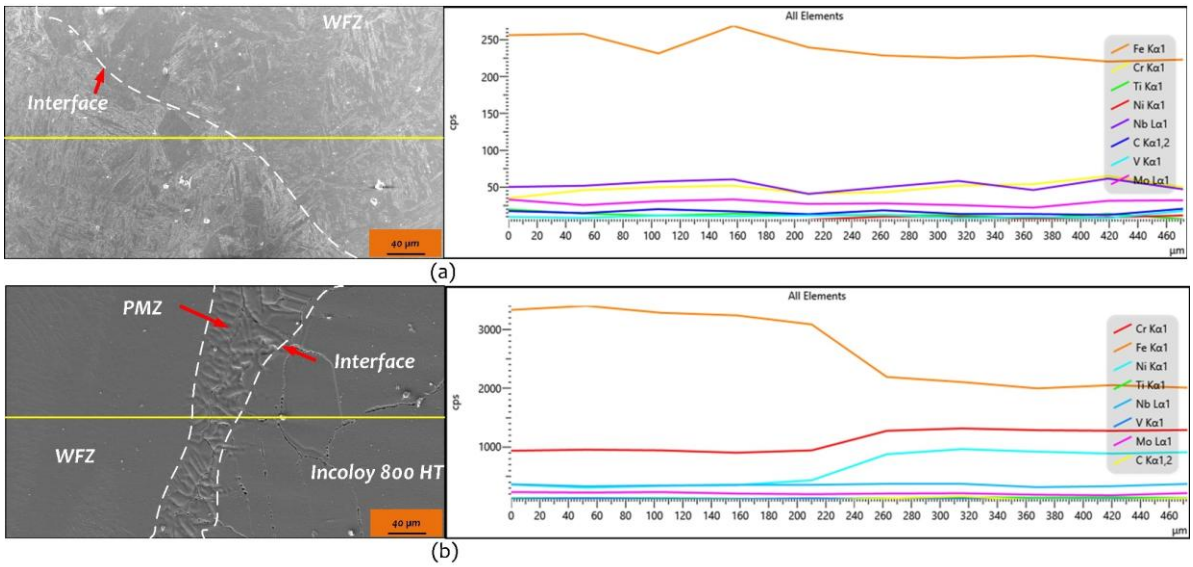


Figure 5.3 : (a) Line mapping spectrum in the SEM image of the P91 weld interface in the AW condition (b) SEM image of Incoloy 800HT weld interface in AW state with line mapping spectrum

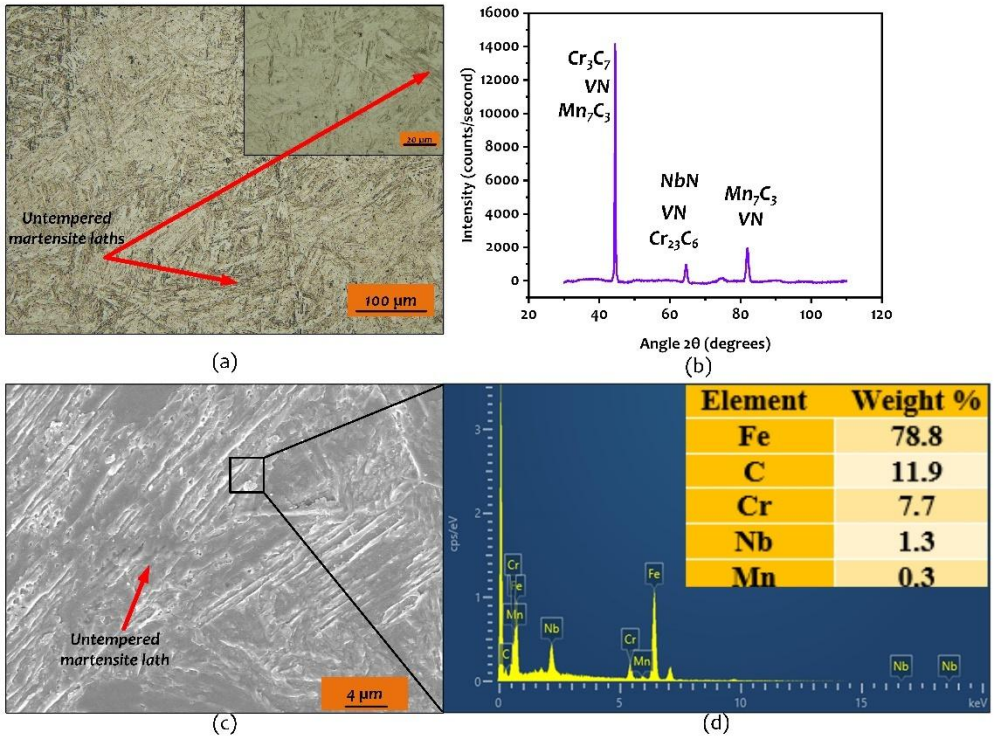


Figure 5.4: (a) Optical view of WFZ in the AW condition (b) WFZ XRD-diffractogram in the AW state (c) SEM image of WFZ in AW state (d) EDS spectrum of the marked small area in the WFZ

Figure 5.4(a-d) shows the WFZ in the AW condition. The microstructure observed in the AWSER90S-B9 filler WFZ shows quenched martensite laths with PAGB and precipitates. The observed WFZ has limited precipitation due to the dissolution of precipitates in high temperatures generated while welding. (Pandey et al., 2018b) reported the presence of δ-ferrite in WSER90S-B9 filler WFZ, while no such formation of δ-ferrite was witnessed in the present study. The $M_{23}C_6$ and MX precipitates tend to diffuse into the martensite when exposed to high welding temperatures of up to 3000 °C. When precipitates dissolve into the matrix, the percentage C percentage increases and causes an increase in brittleness and microhardness of the WFZ; a possible explanation for the few precipitates in the WFZ is the tempering influence that the temperature cycle of the weld passes has on the previously deposited passes. Martensite laths appear to have solidified in an extended path

perpendicular to the weld contact in the vicinity of the P91 weld interface. The WFZ chemical composition was analyzed through OEM. The weight percentage of elements was as follows: Carbon (C): 0.12, Manganese (Mn): 0.41, Molybdenum (Mo): 0.80, Titanium (Ti): 0.001, Iron (Fe): 88.90, Silicon (Si): 0.25, Chromium (Cr): 8.30, Nickel (Ni): 0.31, Niobium (Nb): 0.05, and Copper (Cu): 0.05. Further, the Cr_{eq} was determined using equation (5.1) w, which contains austenite stabilizers, and Ni_{eq} was calculated from equation (5.2), which contains ferrite stabilizers. The Schaeffler diagram (Schaeffler, 1949) is used to plot the Cr_{eq} and $Ni_{eq,}$ which helps predict the WFZ microstructure, as shown in Figure 5.5.

$$\%Cr_{eq} = \%Cr + 2\%Si + 1.5(\%Mo) + 5(\%V) + 5.5(\%Al) + 1.75(\%Nb) + 1.5(\%Ti) + 0.75\ (\%W) \quad (5.1)$$

$$\%\ Ni_{eq} = \%Ni + \%Co + 30(\%C) + 25(\%N) + 0.5(\%\ Mn) + 0.3(\%Cu) \quad (5.2)$$

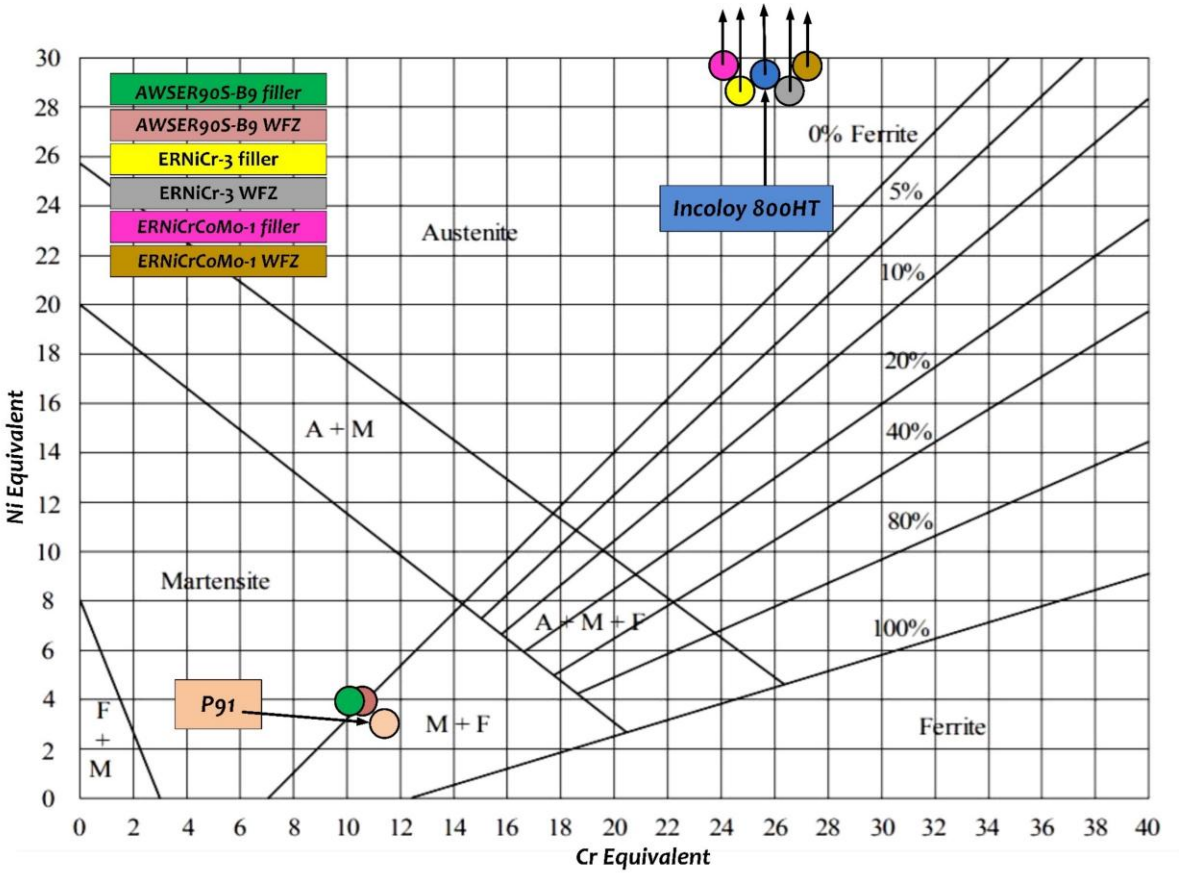


Figure 5.5 : Schaeffler plot to predict the WFZ microstructure (Schaeffler, 1949)

However, in the weld center, equiaxed PAGBs were witnessed. This behavior in the martensite lath structure could be due to rapid cooling and solidification of the martensite near the weld interface, while due to high peak temperature in the weld center, a comparatively slower cooling rate of the weld center region causes multiple nucleation sites and the formation of equiaxed PAGBs. The XRD diffractogram shown in Figure 5.4(b) confirms the presence of the NbN, VN, Mn_7C_3, $Cr_{23}C_6$, and Cr_7C_3 phases in the WFZ region. Figure 5.4(c) shows an SEM micrograph of AW state WFZ with martensite laths and no precipitates. The EDS spectrum in Figure 5.4(d) shows the chemical chemistry of the marked area in the WFZ; Cr, Nb, and C percentages were found higher.

Figure 5.6(a) illustrates the different features of the WFZ observed in the PWHT state; transformation after PWHT is much clearer in Figure 5.6(b) with the presence of white precipitates in large amounts. The microstructure observed is tempered martensite laths with heavy precipitation. PWHT temperature and duration are crucial for enhancing the mechanical characteristics of the WFZ because tempering simulates a diffusion controlled

process. The PWHT at 760 °C for two hours demonstrated the effectiveness of tempering the martensite laths and reprecipitating the carbides and carbonitrides in the AWSER90S-B9 filler weld, which is identical to P91 HAZ. Figure 5.6(b) illustrates the distribution of these re-evolved white precipitates over the PAGBs and lath boundaries in the WFZ. The area mapping of the precipitates that have reappeared in the WFZ is depicted in Figure 5.6(c). The area map gives a qualitative observation of elemental distribution around evolved features. The presence of abundant carbon across the precipitates, as shown by the area map, confirms that they are carbides. A slight percentage of V was also found in those precipitates.

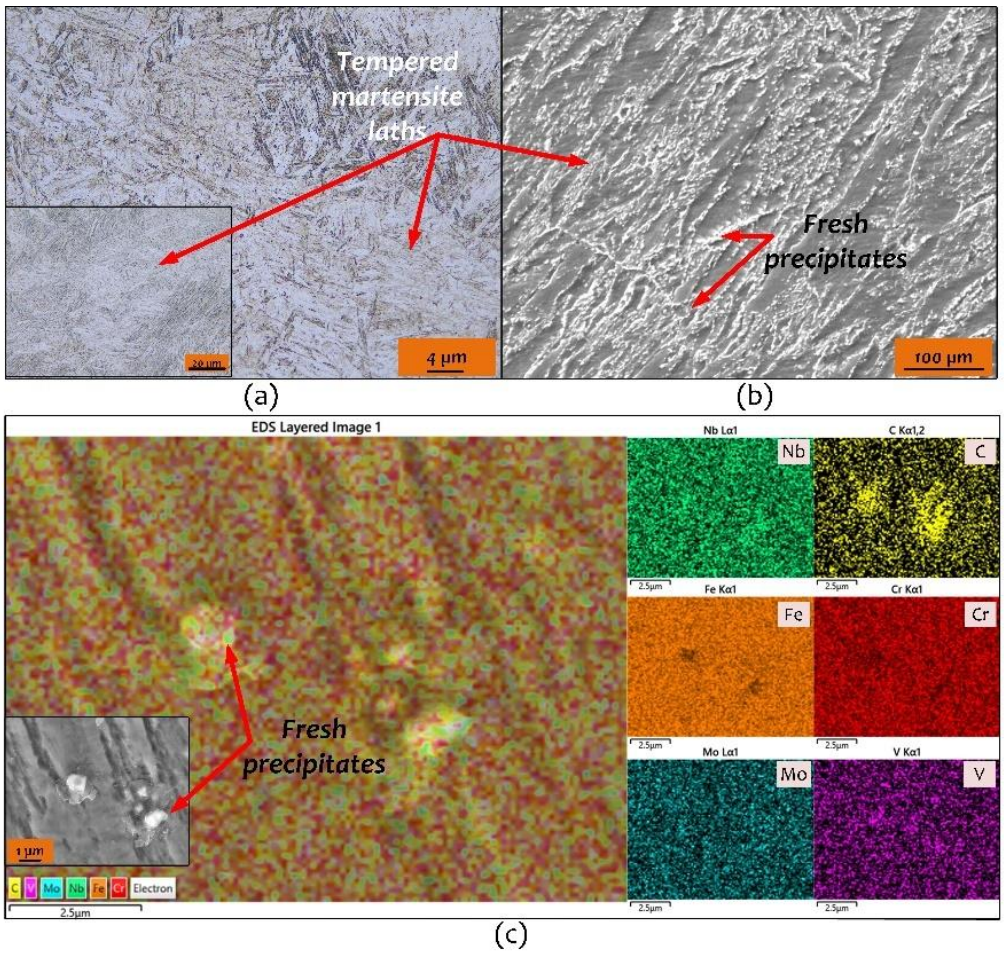


Figure 5.6 : (a) PWHT-state optical representation of WFZ (b) SEM image of WFZ in AW state (c) after PWHT, the new precipitates in the WFZ were mapped out using area mapping

5.1.3 Residual Stresses

The DHD technique of determining the residual stress below the surface is a well-trusted technique as it gives realistic data at a precise location (Skouras et al., 2013). The volumetric transformations, phase transformations, and transformation induced plasticity are strong determinants of the kind and degree of residual stresses produced during weld solidification. Figure 5.7 shows the longitudinal and transverse residual stresses for the WFZ in the AW and PWHT states. The longitudinal stresses in the AW state WFZ were measured at a high of -120 MPa compressive residual stresses at the weld face and 52 MPa tensile residual stresses close to the weld root. The transition of compressive to tensile nature along the depth of the weld can be attributed to the V-groove weld. The weld root bears minimum levels of residual stresses as a lesser amount of WFZ is deposited in the root. Also, multiple thermal cycles may have caused tempering and precipitation in the region, helping in relieving compressive stresses and transforming them into tensile stresses. Transverse residual stresses were majorly in tension and nearly neutral in the weld root region; the maximum level recorded was 42 MPa. The buildup of tensile stresses in the WFZ is the

consequence of angular distortion. The martensitic phase change creates compressive stresses in the WFZ, whereas tension stresses are created when the WFZ solidifies. The longitudinal residual stresses were close to the neutral axis in the weld root region after PWHT, and they were slightly relaxed in the weld top region. The transverse residual stresses were found to be affected by the tempering as they almost changed their nature. Near the weld center and weld root, the residual stresses were transformed into a compressive nature, which could be due to the relieving of tensile stresses in the surroundings, such as P91 HAZ, and inducing compressive stresses in return. However, the residual stress levels were neutralized after PWHT to acceptable levels.

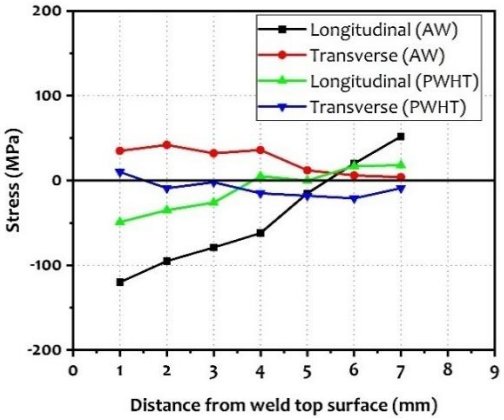


Figure 5.7 : Residual stress distribution plot observed for WFZ in AW and PWHT states

5.1.4 Tensile Properties

Table 5.1 lists the observations made during the tensile testing of prepared tensile specimens. The prepared specimens before and after fracture are shown in Figure 5.8(a-b). The AW standard tensile specimen before fracture gave a UTS of 538 MPa and a YS of 168 MPa. The typical tensile specimen broke after heavy necking in the Incoloy 800HT base metal side with 40% elongation. The WFZ provided a UTS of 609 MPa when the AW subsize tensile specimen was implemented to test its tensile strength, but it failed from the WFZ with a minimum elongation of just 30%. When compared to UTS of P91 and Incoloy 800HT base metal (673 MPa and 593 MPa, respectively), the obtained UTS values for AW subsize and the standard tensile specimen is comparable to the base metal's strength. Although UTS in the subsize specimen is somewhat lower than the base metal UTS of P91, this may be because the precipitates have completely dissolved into the matrix. The standard PWHT tensile specimen failed from the weld interface on the Incoloy 800HT side. It yielded UTS of 525 MPa and YS of 156 MPa. Before failing, the PWHT standard tensile specimen gave a decent elongation of 37%. Failure at the weld interface in the PWHT state may be caused by grain boundary liquation in the HAZ and PMZ development at the weld interface of Incoloy 800HT. Finally, the PWHT subsize specimen produced a UTS of 620 MPa and failed from the WFZ; it gave a limited elongation of 33%. The pinning action from the resurface precipitates in the WFZ after PWHT is attributed to providing strength to it, and hence, PWHT proved beneficial in slightly increasing the tensile strength of the WFZ and reducing its brittleness.

Table 5.1 : Tensile properties observed for different specimens

Specimens	*UTS (MPa)*	*YS [offset 0.2%] (MPa)*	*Elongation (%)*	*Reduction in the area (%)*	*Failure site*
AW (Standard specimen)	538 ± 5	168 ± 10	40 ± 2	71 ± 2	Incoloy 800HT base metal

AW (Subsize specimen)	609 ± 5		30 ± 2	41 ± 3	Incoloy 800HT weld interface
PWHT (Standard specimen)	525 ± 5	156 ± 10	37 ± 2	58 ± 3	Incoloy 800HT weld interface
PWHT (Subsize specimen)	620 ± 5		33 ± 3	45 ± 3	Incoloy 800HT weld interface

In Figure 5.8(b), both the AW and PWHT state subsize specimens showed sudden failure as the WFZ was highly brittle, and even PWHT could not impart sufficient ductility. The lack of ductility in the weld could be detrimental to in-service life as it will make it difficult to detect the failure, and sudden failure will occur. (Chen and Yamashita, 2012) also found similar results and supported the observations made in the present study. The PWHT increased the tensile strength and conversely affected the Charpy impact toughness. Fractography was also performed for the broken tensile surfaces of the PWHT standard and subsize specimen, as shown in Figure 5.8(c-d), respectively. The failure mode appears to be a hybrid, i.e., both ductile and brittle modes of failure occurred. On observation, it is witnessed that failure occurred on an almost inclined plane. Macro and micro-sized voids are clearly visible with big-sized dimples non-uniformly distributed, hinting at the shear ductile mode of failure (Abbasi et al., 2018). Large cleavage facets are also observed, and deep tear ridges suggest the brittle mode of failure at places, possibly due to sudden crack growth or improper bonding at the weld interface. Figure 5.8(e) presents the engineering stress-strain curve for the base metal and DWJ tensile specimens.

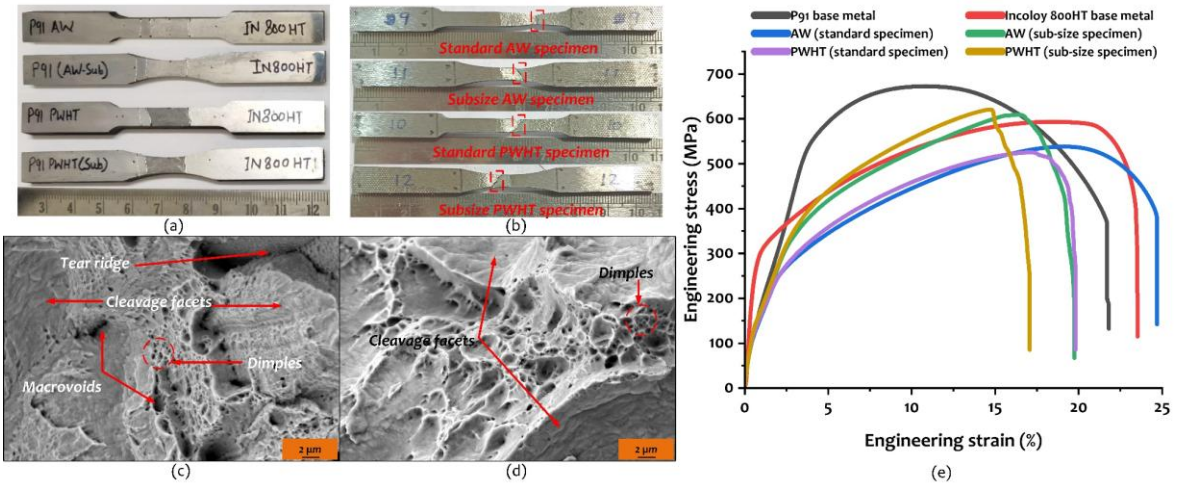


Figure 5.8 : (a) Extracted tensile specimens before tensile testing (b) broken tensile specimens after tensile testing marked with the location of failure (c) PWHT state standard tensile specimen SEM fractography image (d) PWHT state subsize tensile specimen SEM fractography image (e) engineering stress-strain curves for specimens subjected to tensile testing

5.1.5 Microhardness Properties

The approach for taking the micro-indents is presented in the schematic in Figure 5.9. With a force of 0.5 kgf and a dwell duration of 10 seconds, each micro-indent was made at intervals of 0.5 mm. The lowest microhardness of 205 HV was obtained by the P91 HAZ in AW, presumably because of over-tempering. The AW stage FGHAZ region in the P91 HAZ side has an average microhardness of 283 HV, and it gradually ranges from 299 HV to 381 HV towards the CGHAZ region because it has been established that precipitates are the region get dissolved in the matrix. Due to the precipitates' total dissolution and increase of C and N percentages in the region with the coarsening of the grain, the AW CGHAZ

displayed an average microhardness of 430 HV and a peak value of 460 HV. At the P91 interface, the microhardness was marked at 431 HV. The microhardness in the WFZ then varied from 418 HV to 470 HV, with an average microhardness of 441 HV. Because the carbide precipitates in the large coarse grains of the WFZ were completely dissolved with the carbonitride precipitates, the untempered martensite present in the area was observed to be harder than P91 HAZ in AW. The PMZ region near the weld interface of AW Incoloy 800HT was 440 HV, while at the weld interface, it was 177 HV. The microhardness ranges from 153 HV to 189 HV for the AW Incoloy 800HT HAZ and base metal side, respectively.

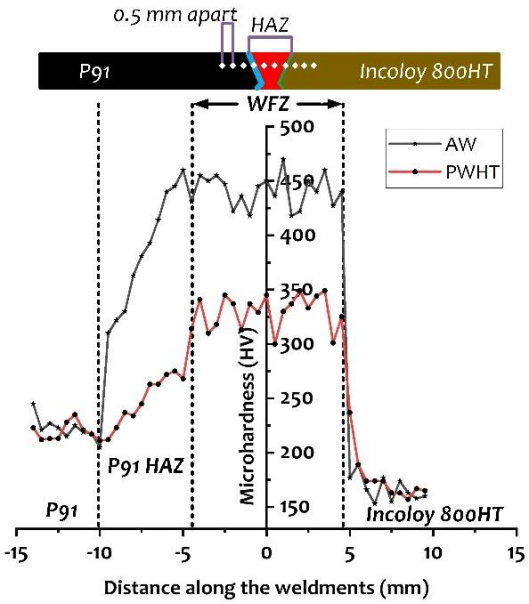


Figure 5.9 : Microhardness variation profile of the weldment in AW and PWHT states

The hard untempered martensite in AW P91 HAZ and AWSER90S-B9 filler WFZ demands PWHT to reduce the detrimental brittleness and hardness in the region. PWHT provides tempering and produces fresh precipitates on the grain boundaries and matrix (Pandey et al., 2019c). Precipitation of carbides and carbonitrides will reduce the matrix's C and N percentages, drastically reducing the region's hardness. Thus, following PWHT, ICHAZ was noted with a little increase in microhardness, with the measured value being 211 HV. The FGHAZ region witnessed a drastic reduction in microhardness as the average value dropped to 230 HV. The CGHAZ also experienced a massive relief in microhardness, and the average value of microhardness in the region dropped to 270 HV with a peak microhardness of 275 HV only. Similarly, the WFZ also witnessed a drastic reduction, but the microhardness observed in the WFZ was still higher than the peak microhardness observed in the P91 HAZ region after PWHT. The nature of the welding could account for this difference, as the WFZ is just like a solidified casting and is different from the processed P91 metal. The reduced average microhardness of the WFZ due to PWHT was 330 HV, and the value ranged from 300 HV to 349 HV. The microhardness of the P91 weld interface after PWHT was detected to be 314 HV, while the microhardness of the Incoloy 800HT weld contact in the PMZ area was 325 HV and 301 HV.

At last, the Incoloy 800HT HAZ and base metal region did not respond to PWHT, and the microhardness in the region remained unchanged. Figure 5.9 shows a graph exhibiting the microhardness distribution over the weldment in both the AW and the PWHT states. (Thakare et al., 2019) used AWSER90S-B9 filler to make a dissimilar weld between SS304L and P91 and discovered comparable changes in the microhardness of the P91 HAZ and the WFZ, which was attributed to the martensitic structure softening and the loss of solid solution hardening.

5.1.6 Charpy Impact Toughness

The Charpy impact toughness specimens with V-notches underwent the Charpy impact toughness test in the AW and PWHT states. The WFZ has the V-notch machined along it, as shown in Figure 5.10(a). The impact caused ductile and brittle mixed modes of fracture in the specimens. The Charpy impact toughness of the AWSER90S-B9 filler WFZ in the AW condition was 96 J. The Charpy impact toughness of the region after PWHT was lowered to 80 J. The reduction was justified as the tensile strength was increased on PWHT. Compared to the Charpy impact toughness of P91 and Incoloy 800HT base metal, the Charpy impact toughness obtained for WFZ is low. Figure 5.10(b) shows the major deformation during the fracture that occurred from the Incoloy 800HT side in both cases, which suggests that the Incoloy 800HT side must have absorbed the major blow and resisted the fracture. Hence, welding of P91 and Incoloy 800HT can be considered to achieve better impact toughness as (Thakare et al. 2019) reported poor Charpy impact toughness in AW state WFZ, but the contracting present study observed an increase in Charpy impact toughness after PWHT. According to (Arivazhagan et al., 2009), the WFZ's low Charpy impact toughness is caused by a high concentration of Nb and V. The lateral contraction in the damaged specimens in Figure 5.10(b) is evidence of the ductile failure mechanism. Due to the WFZ's big coarse martensitic grains, failure takes on a brittle aspect. Fractography of the AW specimen in Figure 5.10(c) shows dimples spread uniformly, with cleavage facets and tear ridges. Similarly, the fractography micrograph in Figure 5.10(d) shows large cleavage facets, macro voids, and non-uniform, but the presence of dimples suggests a mixed fracture mode.

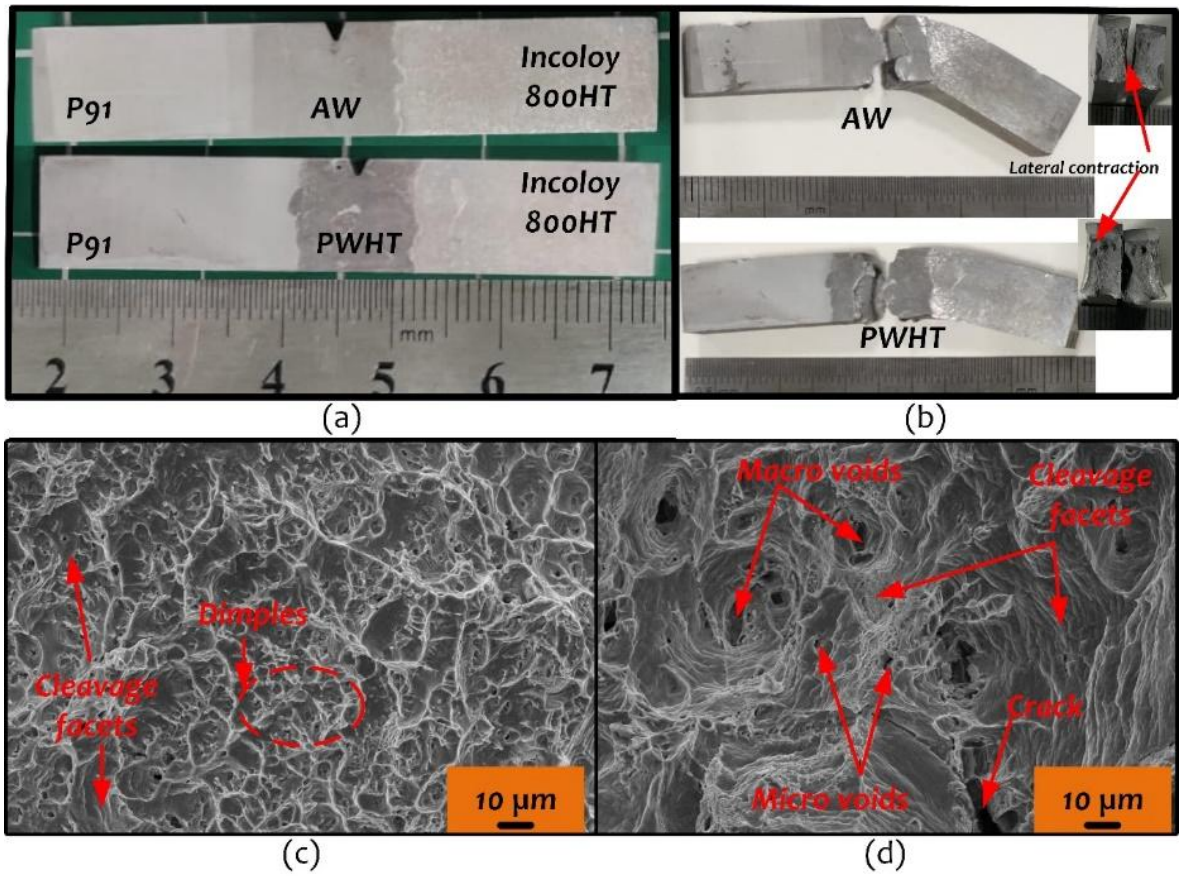


Figure 5.10 : (a) Extracted tensile specimens before tensile testing (b) broken tensile specimens after tensile testing marked with the location of failure (c) PWHT state standard tensile specimen SEM fractography image (d) PWHT state subsize tensile specimen SEM fractography image

5.2 USING ERNiCr-3 (INCONEL 82)

5.2.1 Macroscopic Observations

The welded plate is shown in Figure 5.11(a), and the weld was observed for macrostructural examination under a stereo-zoom microscope, as shown in Figure 5.11(b). The macrostructure of the weld reveals the weld interfaces and weld fusion zone. The capping pass and backing pass are also clearly visible in Figure 5.11(b), and the capping pass affects the consequent passes beneath. The uneven melting and cooling of layers beneath leads to distortion and piling up of residual stresses. The backing pass involves different morphology, and it may also exhibit different microstructural and corresponding mechanical characteristics as base metals are mixed in the weld root region. The observed HAZ for P91 is more expansive and observable owing to its higher thermal conductivity. The HAZ for the P91 side is measured to be approximately 4.2 mm without any presence of δ-ferrite. The HAZ was not observed with any distinct or significant changes, and the features were the same as will be discussed ahead in section 5.4.2. The weld interface at both the base metals shows complete fusion. The stitched microscope image of different P91 HAZ regions formed is shown in Figure 5.12, where different grain size gradients can be easily observed. The Schaeffler diagram is also used to predict the weld fusion zone microstructure. The equivalents of chromium (Cr_{eq}) and nickel (Ni_{eq}) were calculated per equations (5.1) and (5.2), respectively, and plotted on the Schaeffler diagram. The

With the help of OES, the elemental composition of the weld fusion zone was obtained. The weight percentage of elements was as follows: Carbon (C): 0.01, Manganese (Mn): 3.0, Molybdenum (Mo): 0.6, Aluminum (Al): 0.19, Titanium (Ti): 0.035, Tungsten (W): 0.003, Iron (Fe): 4.27, Silicon (Si): 0.1, Chromium (Cr): 20.1, Nickel (Ni): 68.3, Niobium (Nb): 2.24, Vanadium (V): 0.03, and Copper (Cu): 0.04. The average angular distortion (θ) measured was 3.2 degrees. The angular distortion in the weld plate was measured as per the schematic in Figure 5.13 at six different locations along the length of the welded plate using the following equation:

$$\theta = \sin^{-1}\frac{y_i}{x_i} \tag{5.3}$$

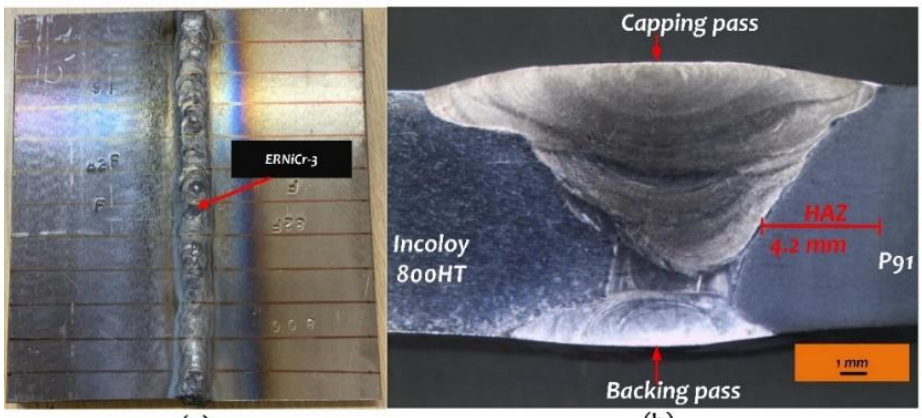


Figure 5.11 : Microstructure of the weld bead in the as-welded condition



Figure 5.12 : Optical images showing different HAZ subzones in AW condition

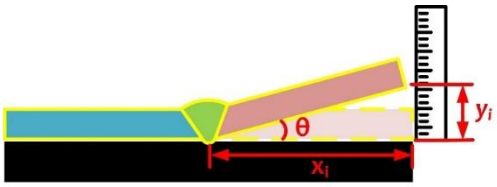


Figure 5.13 : Schematic representing angular distortion method

5.2.2 Weld Interface and Weld Fusion Zone (WFZ) Microstructure Characterization

The weld interface between ERNiCr-3 WFZ and P91, shown in Figure 5.14(a,c), is observed with a thicker weld interface. The weld Incoloy 800HT weld interface (Figure 6.17(b,d)) shows complete fusion owing to the near melting point of ERNiCr-3 to the Incoloy 800HT. The HAZ of Incoloy 800HT in Figure 5.14(c) represents liquation and extensive melting of the grain boundary with cellular and columnar dendritic growth in the weld fusion zone. The WFZ in Figure 5.14(a) also shows the presence of SGBs and MGBs with mixed equiaxed and columnar dendritic structures. Figure 5.14(b) shows the formation of the unmixed zone, type II boundary, and macrosegregation (island formation). The presence of the type II boundary suggests the transition of solidification behavior from ferritic to austenitic and allotropic transformation on the P91 side (Sireesha et al., 2000). SGBs of mixed lengths were observed at Incoloy 800HT and P91 weld interfaces. Since at the P91 interface, unmixed zone formation took place, which led to uneven cooling at the interface, causing more shorter length SGB to appear at the P91 interface. Since the solidification of the liquid weld starts from the partially melted base metal, the growth of the dendrites is determined by the rate of cooling. The capping pass, which cooled at a faster pace if compared to the passes beneath, majorly showed the presence of an equiaxed dendritic structure. Obtaining an equiaxed structure is ideal for obtaining a weld with optimum strength. However, the multiple heat cycles during the welding process in multipass GMAW cause delayed and uneven cooling in the prior laid passes, causing the formation of columnar dendritic growth. Hence, solidification occurs with the heterogeneous distribution of equiaxed, cellular, and columnar dendrites.

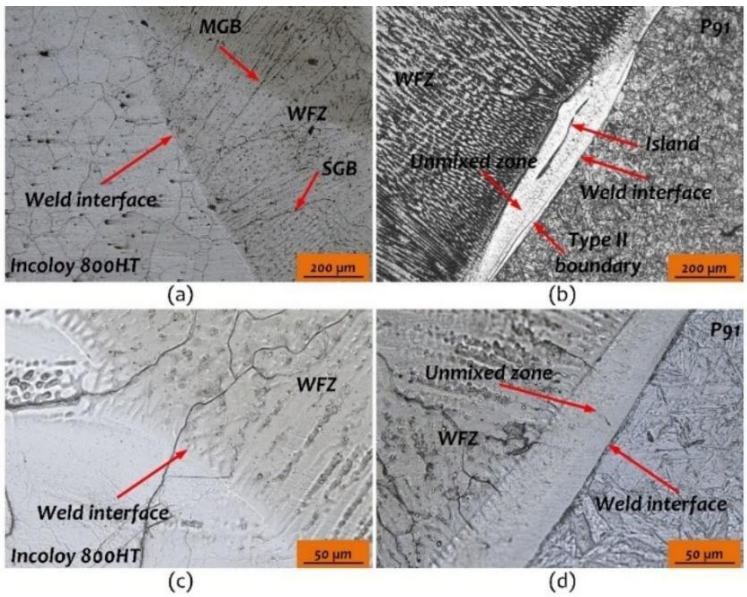


Figure 5.14 : Weld interface optical images of (a) AW Incoloy 800HT (b) AW P91 (c) AW Incoloy 800HT AW at higher magnification (d) AW P91 at higher magnification

Further, for detailed analysis regarding the elemental distribution across the weld interfaces, EDS line spectra and EPMA analysis were performed. In the EDS line spectra of the P91 weld interface in Figure 5.15(a), clear iron, nickel, and chromium variation can be witnessed over the interface and unmixed zone. These variations are merely due to the

compositional differences; however, no prominent segregation across interfaces for other elements was observed. For EPMA across the P91 weld interface (Figure 5.15(b)), similar variation can be observed for Fe, Ni, and Cr again, and a slight variation for Mo can be observed in the unmixed zone. No significant variation could be found for V and Al. Niobium variation in the WFZ could be indicating its segregation in the dendritic region and formation of Nb-rich phases. Titanium bright spots also might suggest segregation along the dendritic region, but it probably indicates the formation of Ti-rich precipitates in the WFZ.

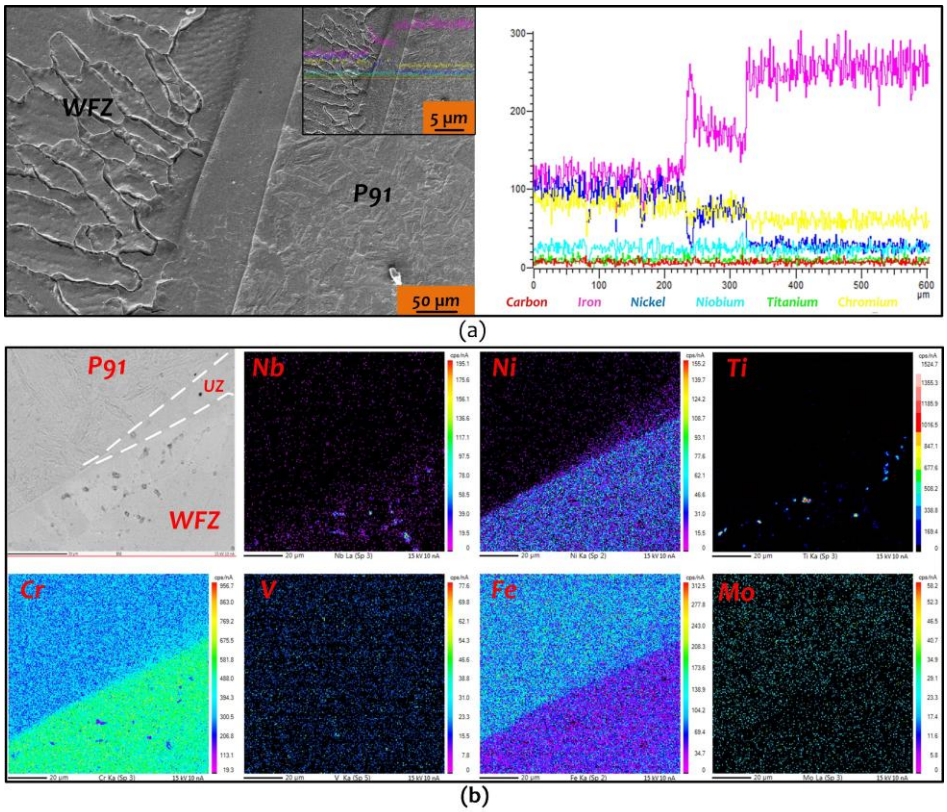


Figure 5.15 (a) SEM image for AW P91 weld interface (b) Line map EDS analyses across the P91weld interface (d) EPMA analysis for P91 weld interface

In Figure 5.16(a), the Incoloy 800HT weld interface indicates the variation in iron, nickel, chromium, and niobium due to compositional differences. Nb peak suggests the presence of Nb-rich precipitate near the interface. No segregation of carbon or other elements was witnessed. In detailed EPMA analysis (Figure 5.16(b)), Cr, Ti, and Nb segregation can be observed around the dendritic region in WFZ, and Fe deficiency is witnessed in the Cr, Ti, and Nb-rich regions. The bright spot of Ti and Nb in WFZ also indicates the presence of Ti or Nb rich precipitates majorly in the WFZ.

The Cr_{eq} and Ni_{eq} of P91 base metal, Incoloy 800HT base metal, ERNiCr-3 filler metal wire, and ERNiCr-3 WFZ are plotted on the Schaeffler diagram plot. On the Schaeffler diagram, the predicted solidification structure of the WFZ is austenitic, as shown in Figure 5.5. Further, in Figure 5.17(a), a fully austenitic solidification structure can be seen in the WFZ. In the optical image (Figure 5.17(a,b)), the SGBs and SSGBs are observed with the equiaxed dendritic structure. The PWHT does not have any practical effect on the WFZ (Bhaduri et al., 1995). In Figure 5.17(c), the line EDS spectra along the WFZ clearly show the segregation of Nb, Al, C, Ni, Cr, and Fe along the SGBs. The titanium did not show any significant segregation; however, a sudden peak over the cuboidal precipitate confirms the presence of Ti(C,N) in the WFZ. The heavy segregation in the WFZ along SGBs and dendritic region is due to the rapid solidification of the weld.

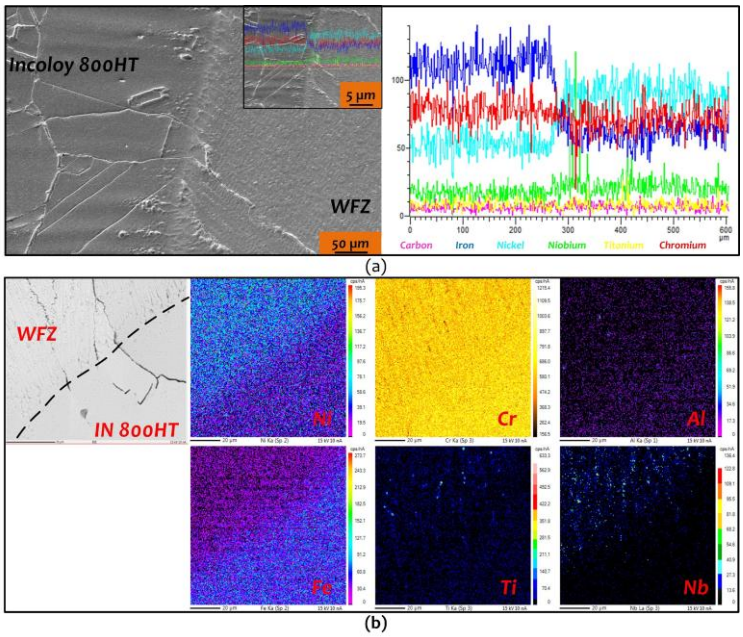


Figure 5.16 : (a) SEM image for AW Incoloy 800HT weld interface (b) Line map EDS analyses across Incoloy 800HT weld interface (d) EPMA analysis for P91 weld interface

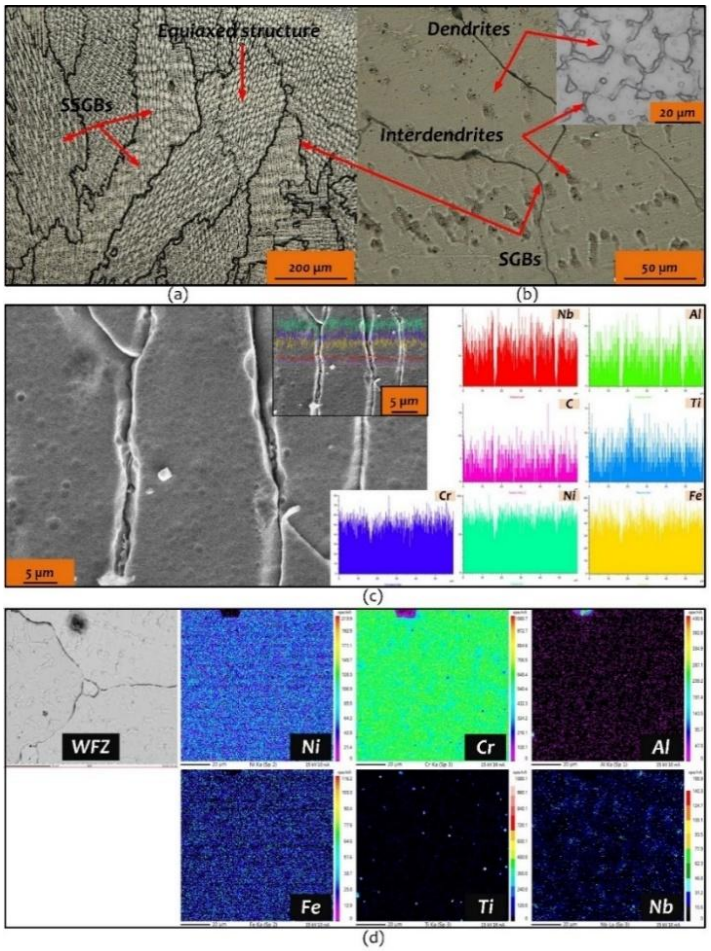


Figure 5.17 : ERNiCr-3 filler-based DWJ: (a) WFZ optical image (b) WFZ optical image at higher magnification (c) SEM micrograph of WFZ and line EDS spectra across the interdendritic region (d) EPMA analysis of weld fusion zone

The EPMA analysis of the WFZ in Figure 5.17(d) clearly indicates the segregation of Cr and Nb into the matrix. Slight segregation of Ni can also be confirmed, and no significant variation in Fe is observed. But Ni, Cr, Fe, and Nb are in minimum concentration at the

possible oxide precipitate at the top. The variation in weld fusion zone microstructure is caused by the segregation of alloying elements such as Fe, Cr, Nb, and Ni. The segregation of such elements leads to the formation of secondary phases like NbC and gamma prime (γ'). The increase in Al at the top spot is a possible indication of the presence of oxide of Al. Since Ni is absent, the possibility of the gamma prime phase there is eliminated. The bright spots of Ti and Nb confirm the presence of Ti and Nb-rich precipitates in the WFZ. Nb is highly susceptible to segregation witnessed, which might also make the weld prone to solidification cracks.

5.2.3 Residual Stresses

The data was obtained for WFZ through the DHD residual stress measuring technique, as shown in Figure 5.18(a). The peak longitudinal and transverse residual stress levels reached 412 MPa and 360 MPa at a depth nearing 3 mm. After PWHT, the peak longitudinal and transverse residual stresses were relieved significantly by 48% and 52%, respectively. The WFZ of ERNiCr-3 induced residual stresses due to multiple thermal passes during welding, and it is witnessed here that responded to PWHT, and residual stresses were reduced to a level near the neutral axis. The WFZ solidified into the austenitic structure, which is associated with shrinkage and hence introduces the tensile residual stresses. Also, the Incoloy 800HT HAZ residual stress data, as shown in Figure 5.18(b), depicted a similar trend as ERNiCr-3 based WFZ, and Incoloy 800HAZ comes from the Inconel family of alloys. The reduction in residual stresses was slightly low for the top surface and center of the plate. However, the stresses fall up to the neutral axis after PWHT transverse residual stresses turned compressive, showing residual stress of -45 MPa. This is attributed to the possible increase in grain size in Incoloy 800HT HAZ. The P91 HAZ for most of the depth from the weld face had compressive residual stresses induced due to the formation of HAZ during welding owing to its higher thermal conductivity. The HAZ formation in P91 is well known for the microstructural changes involving grain coarsening and precipitated dissolution. The data for P91 HAZ in Figure 5.18(c) shows tensile residual stresses were absent, and in AW condition, comparatively higher compressive stresses were present near the bottom surface. The longitudinal and transverse residual stresses were compressive for most of the top surface up to 6 mm depth and were reduced in the bottom after PWHT. The increase in compressive stresses significantly in the longitudinal direction is due to phase changes in P91 HAZ and the relaxation of stresses in WFZ during PWHT. A similar increase in compressive levels after PWHT was observed in a study conducted in the past (Chuvas et al., 2015).

The DHD operation for measuring the residual stresses in P91 and Incoloy 800HT HAZ required half of the core column containing the reference hole also to cover the WFZ, which would have influenced the data obtained. However, the DHD technique fails to give the data for a precise location as it measures average values for a small sampling volume. However, it can give realistic and consistent measurements for the induced residual stresses during DWJ (Skouras et al., 2013).

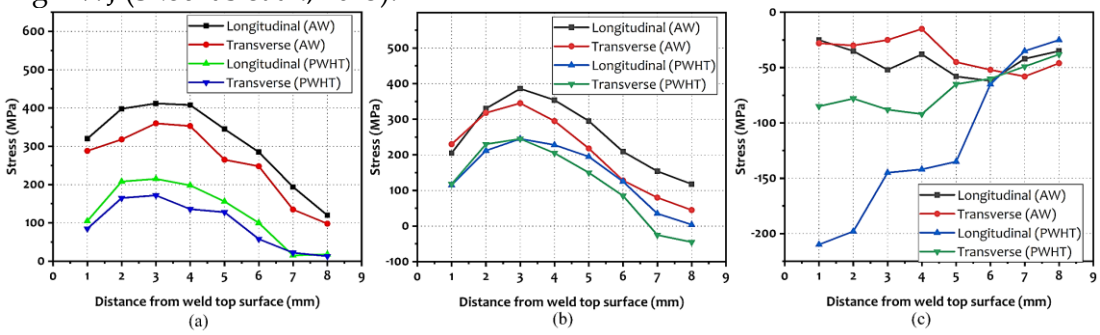


Figure 5.18 : Residual stress variation profiles for (a) WFZ in AW and PWHT states (b) Incoloy 800HT HAZ in AW and PWHT states (c) P91 HAZ in AW and PWHT states

5.2.4 Tensile Properties

The tensile testing for the prepared tensile specimen was conducted at room temperature to observe the yield strength, ultimate tensile strength, percentage elongation, and percentage reduction in area in AW and PWHT conditions. Apart from standard flat tensile samples, subsize tensile samples were prepared to get the weld tensile properties as standard tensile samples observed are bound to fail at base metal. As listed in Table 5.2, the significant observation made is the increase in tensile strength and decrease in yield strength. As observed from Figure 5.19, the failure occurred either at Incoloy 800HT base metal or WFZ. The failure from Incoloy 800HT is expected due to the lower tensile strength of the base metal. In terms of the location of the failure, the results obtained are similar to a recent study made for a similar DWJ (Lakshmanan et al., 2019). Interestingly, the observation contrasts with another study where failure was observed from the P91 side (Bhaduri et al., 1995). In the PWHT standard tensile specimen, the increased tensile strength of 650 MPa exceeds the base metal Incoloy 800HT observed tensile strength. It can be due to observed fine particle carbide precipitations in the Incoloy 800 HT side after the PWHT, which could have imparted more strength. A similar observation made for the subsize tensile samples where tensile strength increased from 570 MPa in the AW state to 578 MPa in the PWHT state suggests that PWHT has had a significant effect on the weldment. The weld of P91 and Incoloy 800HT is witnessed to respond to PWHT as precipitation occurred in the process, imparting strength and reducing the residual stresses. The reduction in residual stresses can be verified in the residual stresses observed in the discussion above. The percentage elongation observed for the samples is below the base metal percentage elongation as ductility is lost due to rapid cooling and heating during welding, and further PWHT seems to also negatively affect the ductility opposite to the trend. On average, the reduction in the area was well over 50%, suggesting tensile samples had appreciable plastic deformation before failure, even surpassing the base metals. Interestingly, the yield strength in AW and PWHT conditions is 161 MPa and 200 MPa, respectively, which is significantly lower than the base metals. The engineering stress-strain curves obtained for the tests are shown in Figure 5.19.

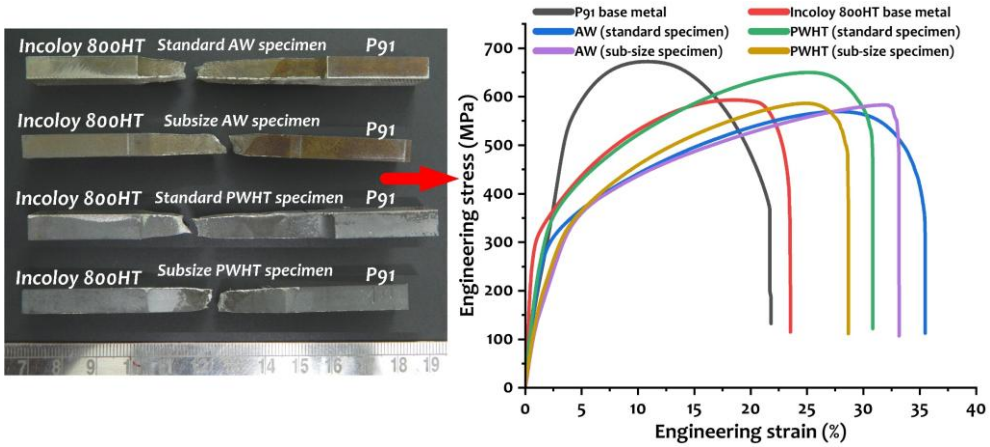


Figure 5.19 : Fractured tensile samples and engineering stress-strain curves for different specimens

In Figure 5.20(a,b), the fractography results for AW and PWHT standard tensile samples for which failure occurred from Incoloy 800HT base metal complete ductile mode of failure can be observed. The presence of dimples, tear ridges, and voids are inhomogeneously distributed. For Figure 5.20(a,b), cleavage facets are clearly observed for the AW and PWHT conditions samples that failed from WFZ. Also, the presence of dimples, striations, cleavage facets, and voids represents the hybrid mode of failure. The striations depict the slow growth of crack due to the growth and termination of crack nucleation. The presence of micro and macro dimples accounts for the dominant ductile nature of the failure. At the same time, cleavages account for brittle nature, which also accounts for the lower yield strength of the WFZ. The significant formation of microvoids that nucleate around

inclusions. The presence of voids also indicates the shear ductile mode of fracture, in which the slip band formation on inclusions is restricted, producing localized strain and void nucleation (Abbasi et al., 2018).

Table 5.2 : Tensile properties for different weld specimens

Specimens	*UTS (MPa)*	*YS [offset 0.2%] (MPa)*	*Elongation (%)*	*Reduction in area (%)*	*Failure location*
AW (Standard specimen)	570 ± 4	252 ± 6	35 ± 2	72 ± 2	Incoloy 800HT BM
AW (Subsize specimen)	583 ± 5	161 ± 6	33 ± 2	62 ± 3	WFZ
PWHT (Standard specimen)	650 ± 4	274 ± 6	31 ± 2	57 ± 3	Incoloy 800HT BM
PWHT(Subsize specimen)	587 ± 4	200 ± 6	29 ± 3	55 ± 3	WFZ

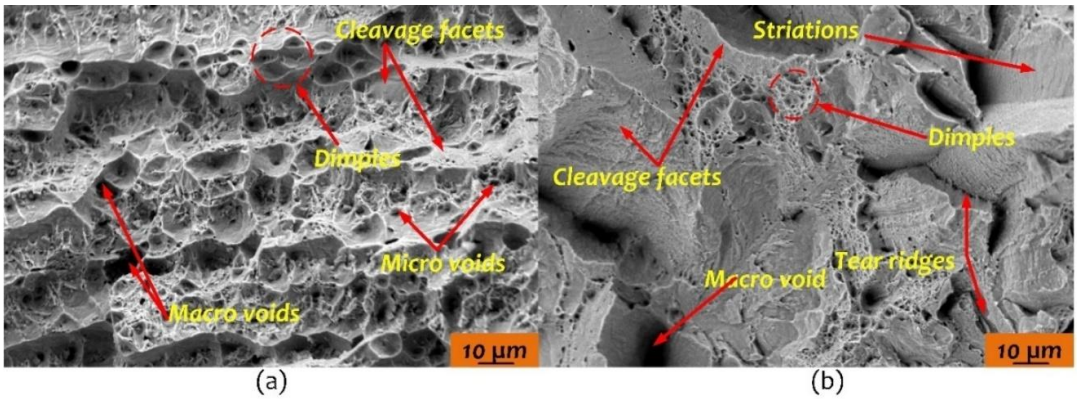


Figure 5.20 : Fractured tensile specimen surface of (a) standard AW tensile specimen (b)subsize AW tensile specimen

5.2.5 Microhardness Properties

The heat-affected zones formed due to heat transfer during welding are characterized through microhardness study. For the presented microhardness study, the microhardness indents were taken in fashion across and along the WFZ at a gap interval of 0.25 mm. The microhardness profile is characterized in both AW and PWHT states. For AW state, as shown in Figure 5.21(a), an inhomogeneous trend of variation in hardness is observed. The microhardness observed for base metal P91 and Incoloy 800HT was 217 ± 10 HV and 171 ± 10 HV, respectively. The WFZ was observed with a comparatively lower microhardness of 169 ± 8 HV. The difference in the constitutional cooling rate at the center of WFZ and WFZ near the weld interface boundary causes the segregation of alloying elements, which determines the austenitic nature of the weld fusion zone observed in the present study. The austenitic microstructure of the WFZ is attributed to the lower microhardness. Also, Incoloy 800HT HAZ showed a comparable range of variation in its microhardness of 175 ± 4 HV and 176 HV at its weld interface. The HAZ of Incoloy 800HT does not show any significant variation with the homogeneous trend, so it is not easy to differentiate its HAZ from base metal. The Incoloy 800HT side witnessed the microhardness varying from 140 HV to 152 HV. The P91, being martensitic, is bound to have higher microhardness than the austenitic Incoloy 800HT. The presence of elements like W, C, Mo, and N in the alloying composition of P91 also gives it strength and hardness. The P91 weld interface was marked with a microhardness of 180 HV, and at the unmixed zone (peninsula) in the WFZ, it was 220 HV. The P91 HAZ has exhibited an inhomogeneous variation, with CGHAZ showing a peak value of 482 HV. The increase in hardness in CGHAZ is well reported in various reported studies and is attributed to the complete dissolution of $M_{23}C_6$ and MX precipitates under the higher temperature (>>A_{c3}) experienced during welding

(Pandey and Mahapatra, 2016). The dissolution of the precipitates in CGHAZ increases the carbon and nitrogen percentages in the solution matrix, which increases the hardness by solid solution strengthening. The FGHAZ after CGHAZ showed lower hardness varying from 411 HV to 328 HV due to incomplete dissolution of the precipitates at lower peak temperature ($\geq A_{c3}$). The ICHAZ showed a minimum microhardness of 184 HV as the region experiences the temperature between A_{c3} and A_{c1}. The retempering of martensite and coarsening of precipitates in the P91 ICHAZ region is attributed to its significantly low microhardness.

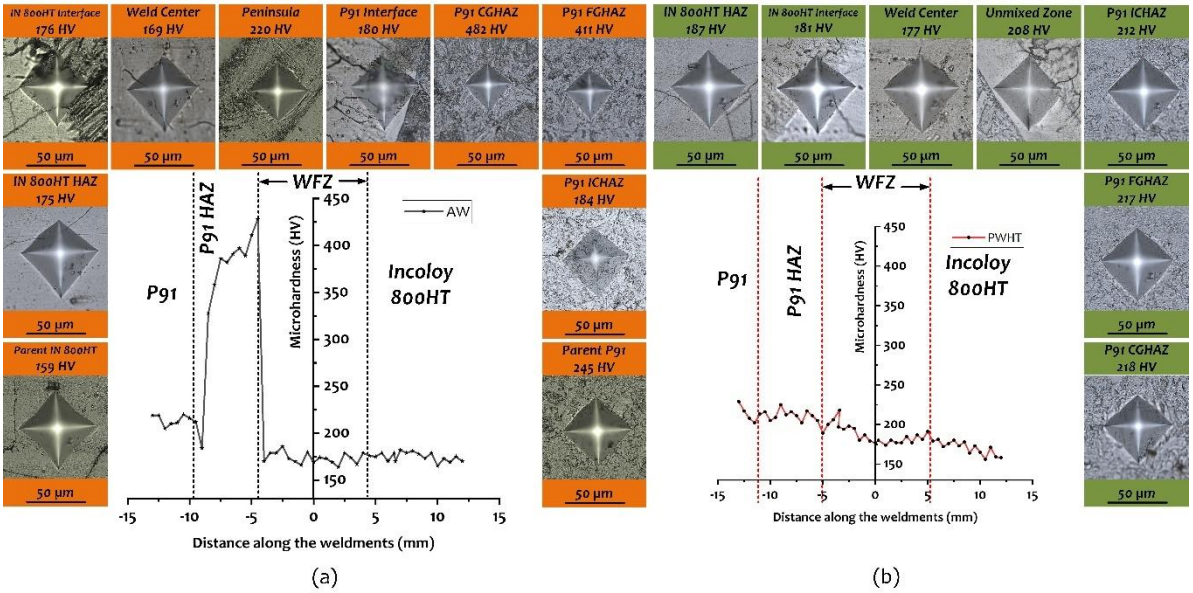


Figure 5.21 : Microhardness variation obtained for (a)AW condition across the P91-Incoloy 800HT DWJ (b) PWHT condition across the P91-Incoloy 800HT DWJ

As recommended to reduce the variation observed in P91 HAZ, PWHT analysis justified the reduction in microhardness, as shown in Figure 5.21(b). The tempering unexpectedly also showed a slight increase in microhardness in WFZ and Incoloy 800HT that might be due to precipitation of Ni_3T, $M_{23}C_6$, and NbC, which also account for the increased tensile strength (Sireesha et al., 2005). The microhardness range observed for the Incoloy 800HT side after PWHT was 156 HV to 191 HV. The unmixed zone near the P91 weld interface showed microhardness of 208 HV as the unmixed zone is formed due to improper mixing of base metal and filler metal for the difference in their melting and solidification temperature. The P91 CGHAZ microhardness value dropped to 218 HV as fresh MX and $M_{23}C_6$ and dissolved precipitates reappeared on tempering. Similarly, a significant drop in FGHAZ microhardness was measured to 217 HV. The ICHAZ showed microhardness of 212 HV, and the improvement is due to the complete tempering of martensite on PWHT. The conclusive observation is that the PWHT successfully reduced the microhardness in the P91 martensitic HAZ. However, austenitic WFZ and Incoloy 800HT responded to PWHT with a slight increase in microhardness.

Further, in the observation made for the microhardness variation along the WFZ, the variation is observed in Figure 5.22. The microhardness seems to be low at the weld top and weld bottom while being highest at the center of WFZ for both AW and PWHT states. The PWHT observation showed a slight increase in microhardness, again accounting for the precipitation in the austenitic matrix of ERNiCr-3 filler.

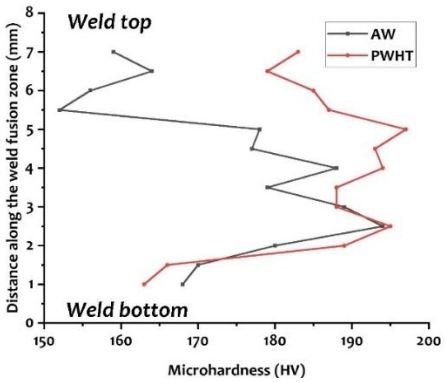


Figure 5.22 : Microhardness variation obtained for WFZ (top to bottom) in both AW and PWHT states

5.2.6 Charpy Impact Toughness

The Charpy impact toughness was obtained for only WFZ in AW and PWHT conditions, as shown in Figure 5.23(a,b). The toughness measured for WFZ at room temperature in the AW condition was 86.2 ± 10 J, and in the PWHT condition, it was 84.2 ± 5 J. Since hardness and tensile increased due to PWHT, it was expected for toughness to decrease. However, the decrease in toughness is significantly less, which is positive in terms of the mechanical strength of the DWJ. In comparison to base metal P91 (104 J) and Incoloy 800HT (102 J) toughness, the WFZ is less. This could be due to the segregation of the alloying elements in the interdendritic region during solidification (Dehmolaei et al., 2009). The presence of precipitates also hinders the dislocation movements, lowering the toughness (Sireesha et al., 2000). The obtained toughness for the DWJ is well above the benchmarked toughness standards. Figure 5.23(b) depicts the lateral contraction occurring for both states with corresponding later expansion. In a similar study, the low toughness after thermal exposure at 625 °C was attributed to the formation of small-sized intermetallic phases introducing the internal notch effect (Sireesha et al., 2005). Also, the dull lustre on the fractured surface indicates the ductile mode of failure. Further, in fractography study of the fractured samples showed the presence of dimples in the direction of failure, confirming the plastic deformation as shown in Figure 5.24(a,b). The dimples were found inhomogeneously distributed and of varying sizes. The presence of cleavage facets, voids, and inclusions can be observed for fractured surfaces of both AW and PWHT specimens.

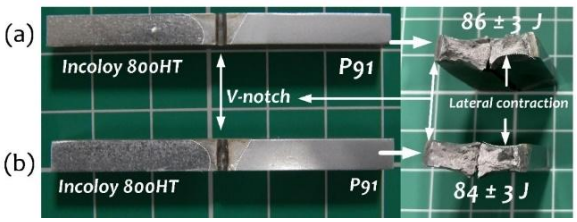


Figure 5.23 : (a) Position of the notch in WFZ in AW state specimen and after fracture specimen (b) position of the notch in WFZ in PWHT state specimen and after fracture specimen

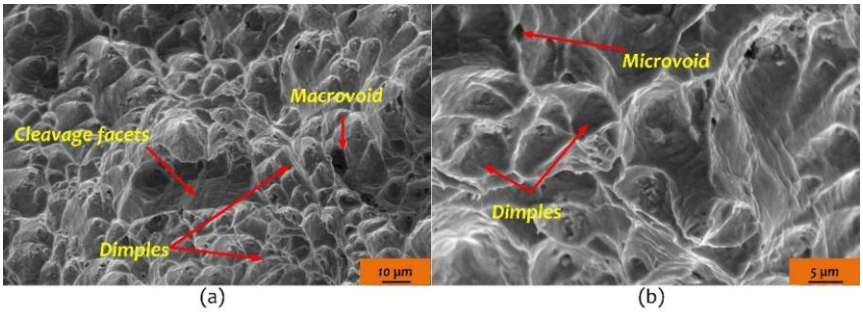


Figure 5.24 : Fractured Charpy impact toughness specimens (a) AW condition surface (b) AW condition surface at higher magnification (a) PWHT condition surface (b) PWHT condition surface at higher magnification

5.3 USING ERNiCrMo-3 (INCONEL 625)

5.3.1 Macroscopic Observations

The ERNiCrMo-3 filler-based DWJ and macrostructure have been shown in Figure 5.25(a-b). The macrostructure revealed the weld interfaces and weld fusion zone. The capping pass and backing pass are also clearly visible in Figure 5.25(b), and the capping pass affects the consequent passes beneath. The uneven melting and cooling of layers beneath leads to distortion and piling up of residual stresses. The welds observed were free of any observational defects and showed complete penetration. The HAZ observed for P91 was more expansive and observable due to its higher thermal conductivity. The HAZ for the P91 side is measured to be approximately 4.4 mm for the ERNiCrMo-3 weld. The HAZ was not observed with any distinct or significant changes, and the features were the same as will be discussed ahead in section 5.4.2. The weld interface at both the base metals in both the welds witnesses complete fusion. The weight percentage of elements was as follows: Carbon (C): 0.01, Manganese (Mn): 0.05, Molybdenum (Mo): 9.05, Aluminum (Al): 0.06, Titanium (Ti): 0.25, Tungsten (W): 0.06, Iron (Fe): 6.00, Silicon (Si): 0.04, Chromium (Cr): 23.3, Nickel (Ni): 58.24, Niobium (Nb): 2.90, Vanadium (V): 0.03, and Copper (Cu): 0.01. The stitched microscope image of different P91 HAZ and Incoloy 800HT HAZ regions has been shown in Figure 5.26 for ERNiCrMo-3 filler-based DWJ.

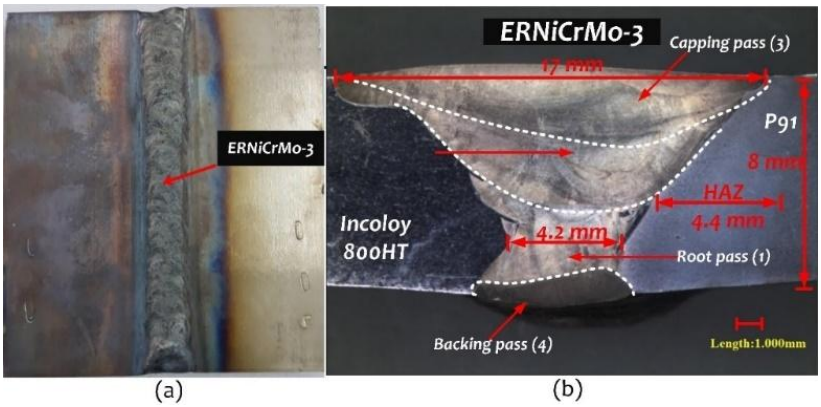


Figure 5.25 : (a) ERNiCrMo-3 filler-based DWJ in AW condition (b) ERNiCrMo-3 filler-based DWJ macrostructure



Figure 5.26 : Stitched optical images of different HAZ subzones in AW condition

5.3.2 Weld Interface and Weld Fusion Zone (WFZ) Microstructure Characterization

The ERNiCrMo-3 filler-based DWJ optical shown in Figure 5.27 depicts the P91 and Incoloy 800HT weld interfaces. Compared to the discussed ERNiCr-3 filler-based DWJ weld interfaces, the ERNiCrMo-3 filler-based DWJ P91 side weld interface also significantly formed the unmixed zone. Incoloy 800HT seemingly has heavy macrosegregation, partially mixed zone formation, and the absence of an unmixed zone. The further analyses of the ERNiCrMo-3 filler-based DWJ P91 weld interface, the line map EDS spectra, as shown in Figure 5.28(a), represent major composition elements (Fe, Ni, Cr, Mo) variation across the weld interface. The variation gradients near the P91 unmixed zone show the diffusion of elements near the weld interface. Similarly, the Incoloy 800HT weld interface analyses, as shown in Figure 5.28(b), confirm the elemental variation across the weld interface and macrosegregation.

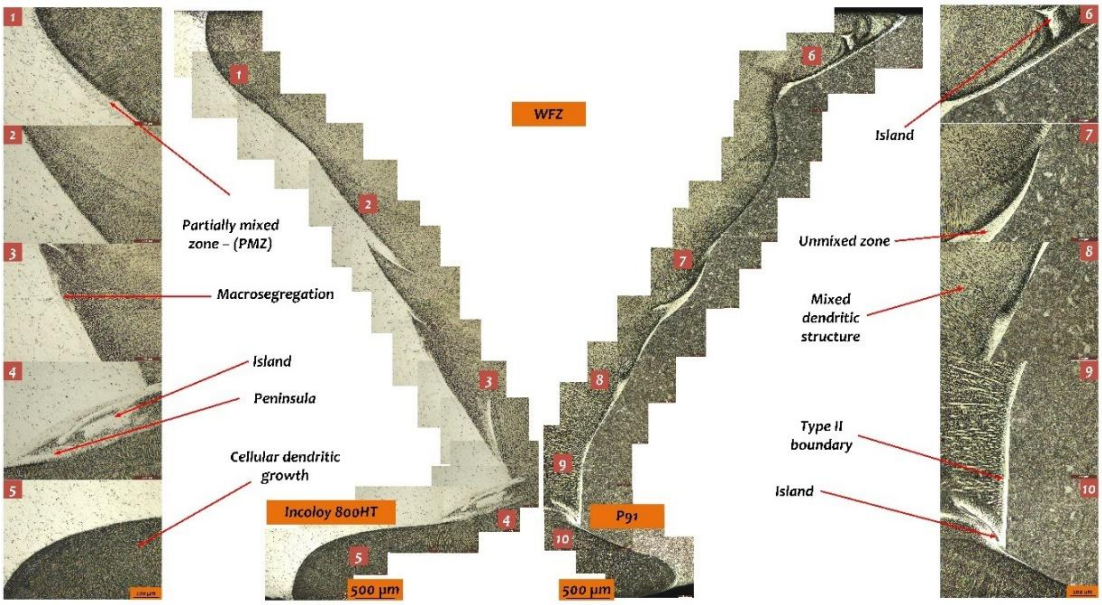


Figure 5.27 : Stitched optical image of Incoloy 800HT weld interface and P91 weld interface of ERNiCrMo-3 filler-based DWJ in AW condition

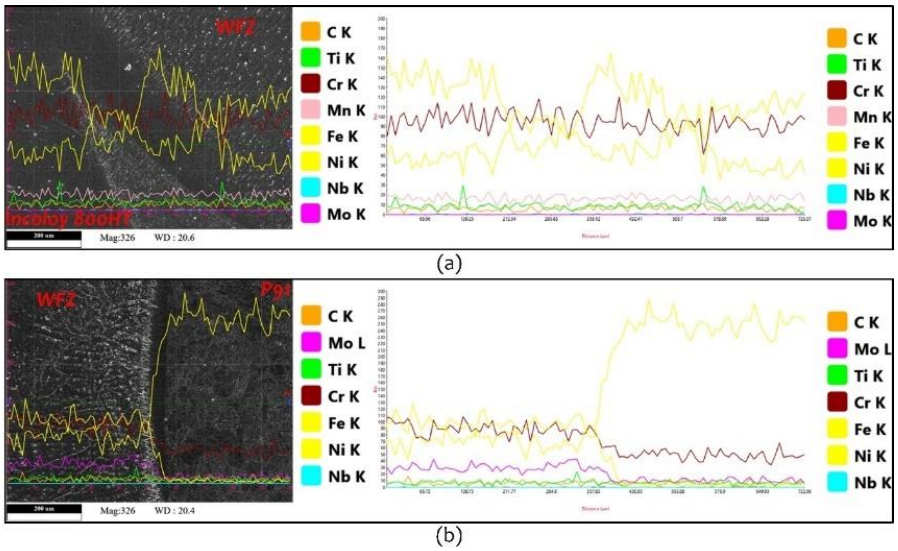


Figure 5.28 : (a) SEM micrograph for AW P91 weld interface of ERNiCrMo-3 filler-based DWJ with line map EDS analysis across the P91weld interface (b) SEM micrograph for AW Incoloy 800HT weld interface of ERNiCrMo-3 filler-based DWJ with line map EDS analysis across Incoloy 800HT weld interface

The Cr_{eq} and Ni_{eq} of P91 base metal and Incoloy 800HT base metal are plotted on the Schaeffler diagram plot. Also, the ERNiCrMo-3 filler metal wire and ERNiCrMo-3 WFZ Cr_{eq} and Ni_{eq} were marked on the Schaeffler diagram. On the Schaeffler diagram, the predicted solidification structure of the WFZ is austenitic for ERNiCrMo-3 filler-based DWJ, as shown in Figure 5.5. Figure 5.29(a-c) shows that the WFZ of ERNiCrMo-3 filler-based DWJ in the AW state has been observed with partially developed SGBs and SSGBs. MGB formation was witnessed near the columnar dendritic packets. The WFZ had the inhomogeneous distribution of equiaxed, cellular, and columnar dendritic packets. As shown in Figure 5.29(a-c), the interdendritic regions have visible precipitation due to the occurrence of microsegregation in the region during weld solidification. Nb and Mo were found heavily segregated into the interdendritic region, causing the precipitation hardening. In Figure 5.29(d-f), the PWHT did not have any observable effect on the WFZ since ERNiCrMo-3 does not respond to the PWHT temperature of 760 ℃. The formation of Ni, Nb, Mo, and Ti-rich precipitates in the WFZ increases the hardness in the region and promotes the laves phase formation during service at high temperatures.

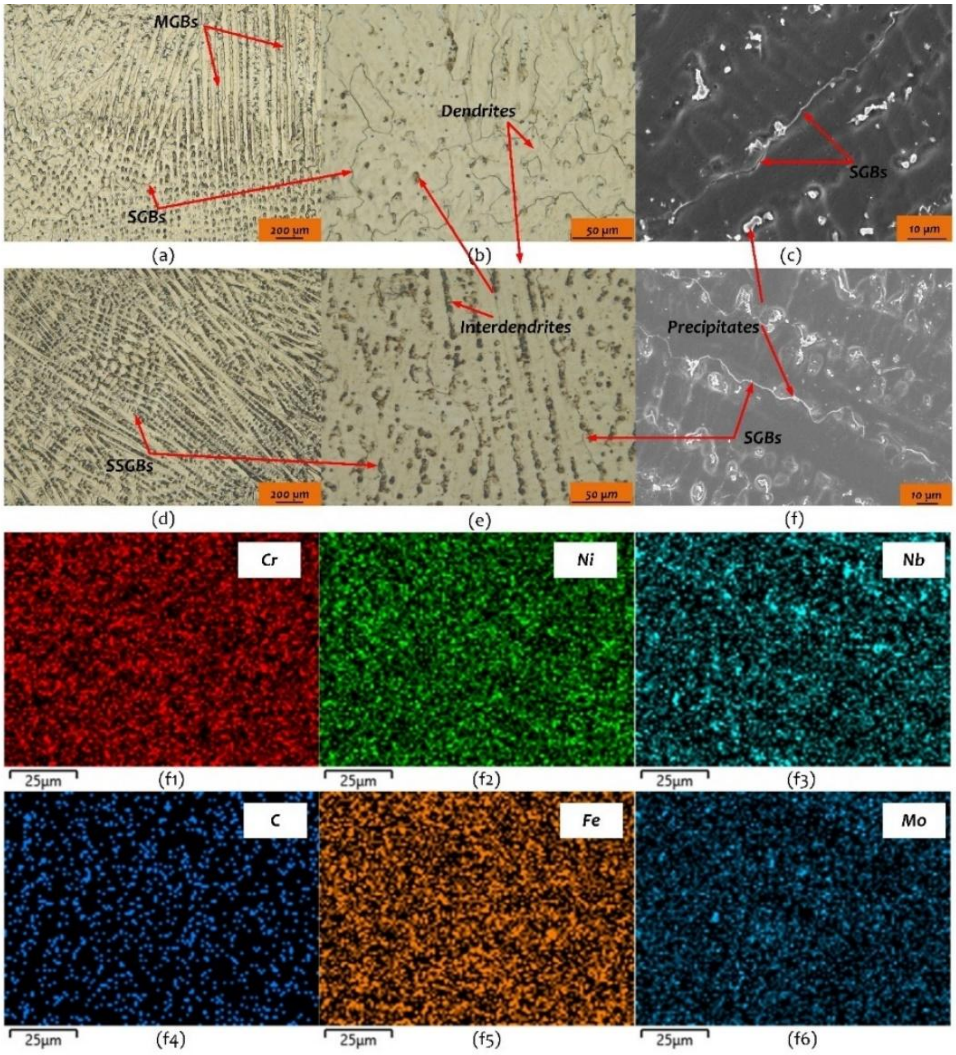


Figure 5.29 : ERNiCrMo-3 filler (a-b) AW WFZ optical image (c) AW WFZ SEM image (d-e) PWHT WFZ optical image (f) PWHT WFZ SEM image (f1-6) EDS /elemental mapping images

5.3.3 Residual Stresses

The residual stress data were obtained for WFZ through the DHD residual stress measuring technique, as shown in Figure 5.30. The DHD technique fails to give the data for a precise location as it measures average values for a small sampling volume. However, it has given realistic and consistent measurements for the induced residual stresses during DWJ (Skouras et al., 2013).

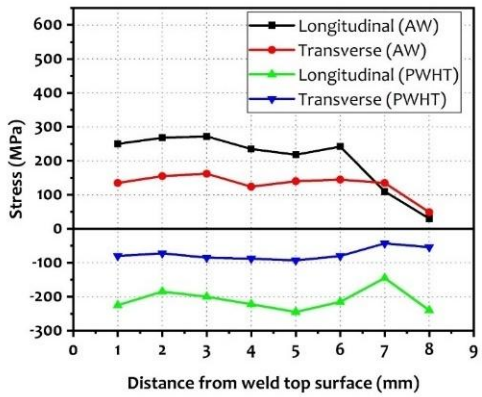


Figure 5.30 : Residual stress variation profiles for WFZ in AW and PWHT states of ERNiCrMo-3 filler-based DWJ

For the ERNiCrMo-3 filler-based DWJ, the residual stress measurement was done only for the WFZ. The WFZ of ERNiCrMo-3 filler-based DWJ had the maximum longitudinal residual stress of 272 MPa at the 3 mm depth. Similarly, the maximum transverse residual stress was 162 MPa at the same depth. Both the stresses were compressive, transverse residual stresses were less severe, and the minimum stresses were observed near the weld root, i.e., 30 MPa along the weld and 49 MPa in the transverse direction. The results have a similar trend compared to the observations made for the AW state WFZ of ERNiCr-3 filler-based DWJ, but ERNiCrMo-3 filler-based WFZ has developed less residual stress overall. Interestingly PWHT resulted in a completely new set of residual stress, tensile and unharmful. The transverse residual stress distribution in PWHT WFZ was almost constant, ranging from -80 MPa (weld top) to -43 MPa (weld root), as shown in Figure 5.30. At the same time, the longitudinal stresses were minimum at the weld center at -245 MPa and maximum near the weld root at -145 MPa. The higher coefficient of expansion leads to tensile longitudinal stresses. In DWJ, the multiple thermal cycles for filler deposition, different cooling rates, and phase transformation highly affect the differential contraction and expansion of the WFZ.

5.3.4 Tensile Properties

Table 5.3 contains the recorded tensile strength measurements for the tested specimens. In contrast to the ERNiCr-3 filler-based DWJ, the ERNiCrMo-3 filler-based DWJ showed relatively poor results. The standard AW standard tensile specimen had a UTS of 554 MPa, and the PWHT standard tensile specimen witnessed a UTS of 564 MPa, a slight increase. The AW standard tensile specimen failed from Incoloy 800HT base metal, and the PWHT standard tensile specimen failed from WFZ, as shown in Figure 5.31(a). The engineering stress-strain curves obtained from the tensile tests conducted have been shown in Figure 5.31(b). The PWHT seems to have increased the UTS, but the ERNiCrMo-3 filler metal reportedly has significantly higher UTS ("From Special Metals.," 2004). The YS for AW and PWHT standard tensile specimens was 241 MPa and 240 MPa, respectively. Further, to determine the tensile strength of WFZ, subsize tensile specimens were tested in both AW and PWHT states. Both AW and PWHT subsize specimens failed from the Incoloy 800HT weld fusion zone, which had the prominent presence of PMZ and heavy macrosegregation. The UTS for AW and PWHT subsize specimens was 510 MPa and 679 MPa, respectively. (Sirohi et al., 2021) also reported an increase in UTS after PWHT, mainly due to the formation of secondary phase particles. The maximum elongation of 28% was observed in the standard AW specimen and a minimum of 21% in the AW subsize specimen, and analogous was the reduction in area percentage.

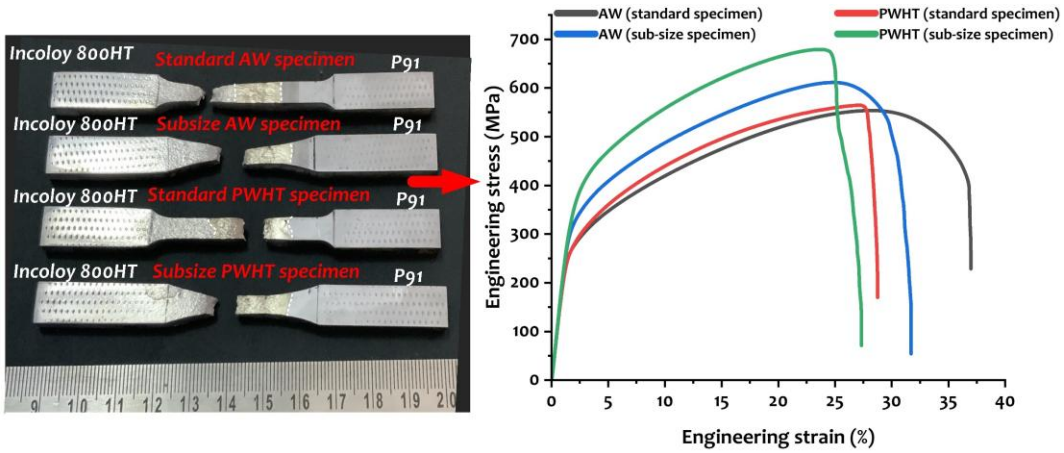


Figure 5.31 : ERNiCr-3 filler-based DWJ fractured tensile and engineering stress-strain for different specimens of ERNiCrMo-3 filler-based DWJ

Figure 5.32(a) shows a significant formation of micro-voids that nucleate around inclusions for the subsize AW tensile specimen of ERNiCrMo-3 filler-based DWJ. The presence of voids also indicates the shear ductile mode of fracture, in which the slip band formation on inclusions has been restricted, producing localized strain and void nucleation (Abbasi et al., 2018). Figure 5.32(b) shows the failure in PWHT ERNiCrMo-3 filler-based DWJ from the WFZ. The presence of dimples over the large area suggests a dominating ductile mode of failure, and the presence of Nb and Mo-rich phases in the ERNiCrMo-3 filler WFZ resulted in the highest UTS.

Table 5.3 : Tensile properties for different weld specimens

Specimens	*UTS (MPa)*	*YS [offset 0.2%] (MPa)*	*Elongation (%)*	*Reduction in area (%)*	*Failure location*
AW (Standard specimen)	554± 4	241 ± 6	28 ± 2	55 ± 3	Incoloy 800HT BM
AW (Subsize specimen)	510 ± 5	-	21 ± 2	29 ± 2	Incoloy 800HT interface
PWHT (Standard specimen)	564± 4	240 ± 6	27 ± 2	47 ± 3	Incoloy 800HT BM
PWHT (Subsize specimen)	679± 4	-	24 ± 3	28 ± 3	WFZ

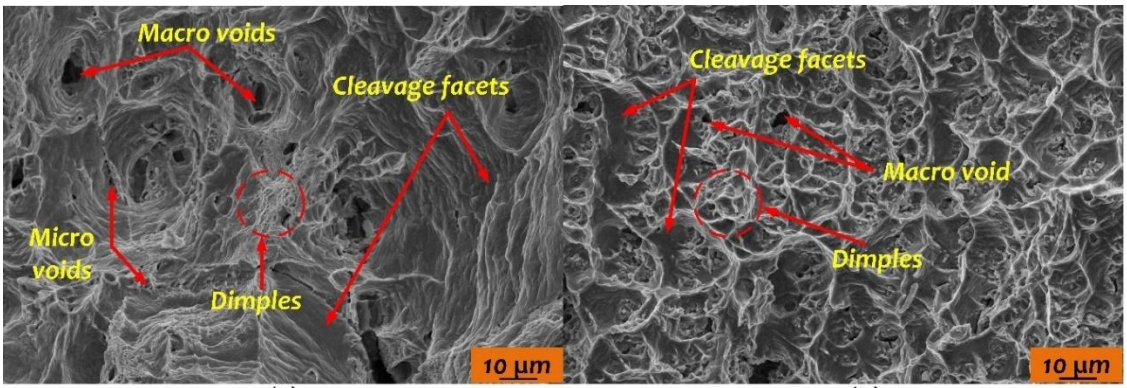


Figure 5.32 : Fractured tensile specimen surface of (a) subsize AW tensile specimen of ERNiCrMo-3 filler-based DWJ (b) standard PWHT tensile specimen ERNiCrMo-3 filler-based DWJ

5.3.5 Microhardness Properties

The microhardness indents were taken in fashion across and along the WFZ at a gap interval of 0.25 mm. The characterization of the microhardness profile has been presented in both AW and PWHT states. The ERNiCrMo-3 filler-based DWJ in the AW state has shown a variation in microhardness, as depicted in Figure 5.33(a). The minimum microhardness of 220 HV was observed in the ICHAZ region of the P91 side, and a maximum microhardness of 427 HV was obtained in the CGHAZ region. FGHAZ region had an average microhardness of 361 ± 24 HV. The WFZ in the AW state showed an average microhardness of 228 ± 12 HV. The Incoloy 800HT HAZ had an average microhardness of 173 ± 15 HV. In the PWHT state, as shown in Figure 5.33(b), the variation in P91 HA microhardness was reduced due to tempering and freshly evolved. The ICHAZ and FGHAZ combined had an average microhardness of 246 ± 18 HV. The CGHAZ microhardness was also reduced to an average of 239 ± 10. WFZ zone did not show any appreciable response to PWHT, and the average microhardness was 222 ± 9 HV. Also, the Incoloy 800HT HAZ region remained unresponsive, with an average HAZ region microhardness of 170 ± 7 HV.

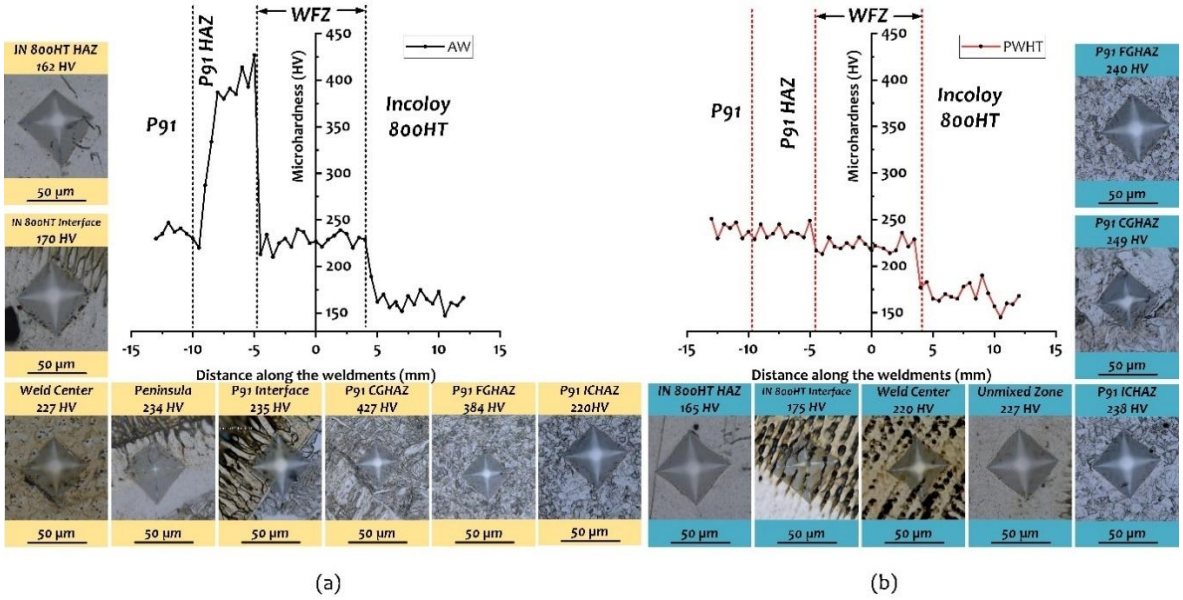


Figure 5.33 : Microhardness variation obtained for (a) ERNiCrMo-3 filler-based DWJ in AW condition across the P91-Incoloy 800HT DWJ (b) ERNiCrMo-3 filler-based DWJ in PWHT condition across the P91-Incoloy 800HT DWJ

5.3.6 Charpy Impact Toughness

The Charpy impact toughness for the WFZ of ERNiCrMo-3 filler-based DWJ was obtained, as shown in Figure 5.34(a-b). The WFZ of ERNiCrMo-3 filler-based DWJ had a Charpy impact toughness of 47 ± 10 J in the AW state and 41 ± 10 J in the PWHT state. As already discussed, the formation of Nb-based secondary carbide phases in the interdendritic regions increases hardness and brittleness in the WFZ. Though PWHT has a trivial effect on WFZ, the impact of toughness decreased slightly may be due to the formation of detrimental secondary phases during PWHT or multiple thermal cycles for filler deposition. Overall, ERNiCrMo-3 filler-based DWJ fails to qualify the benchmark of Charpy impact toughness standards. (Kumar et al., 2021) also raised similar concerns related to the poor and deteriorating Charpy impact toughness of ERNiCrMo-3 filler-based DWJ.

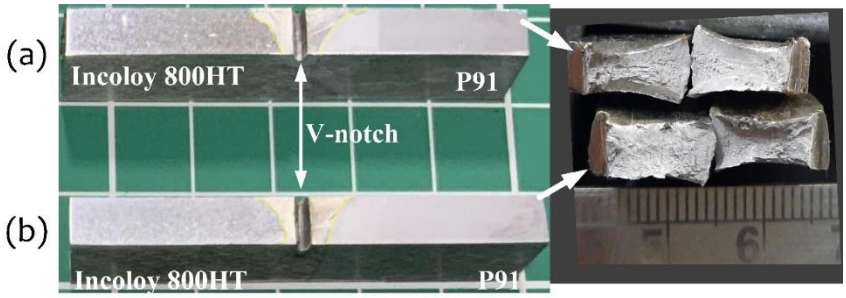


Figure 5.34 : (a) V- notch at ERNiCrMo-3 filler WFZ in AW state specimen and after fracture specimen (b) V-notch at ERNiCrMo-3 filler WFZ in PWHT state specimen and after fracture specimen

Further, in fractography study of the fractured specimens showed the presence of dimples in the direction of failure, confirming the plastic deformation as shown in Figure 5.35(a-b). The dimples were found inhomogeneously distributed and of varying sizes. The stretched-out dimples result in an increase in toughness. Cleavage facets, voids, and inclusions have been observed for fractured surfaces of both AW and PWHT specimens. The ERNiCrMo-3 filler WFZ fractured in ductile mode. However, the comparatively lower Charpy impact toughness to ERNiCr-3 filler DWJ cannot be justified based on fractography

results. Since, the inherited residual and thermal stresses during the welding with different phase transformations affect the material's mechanical properties.

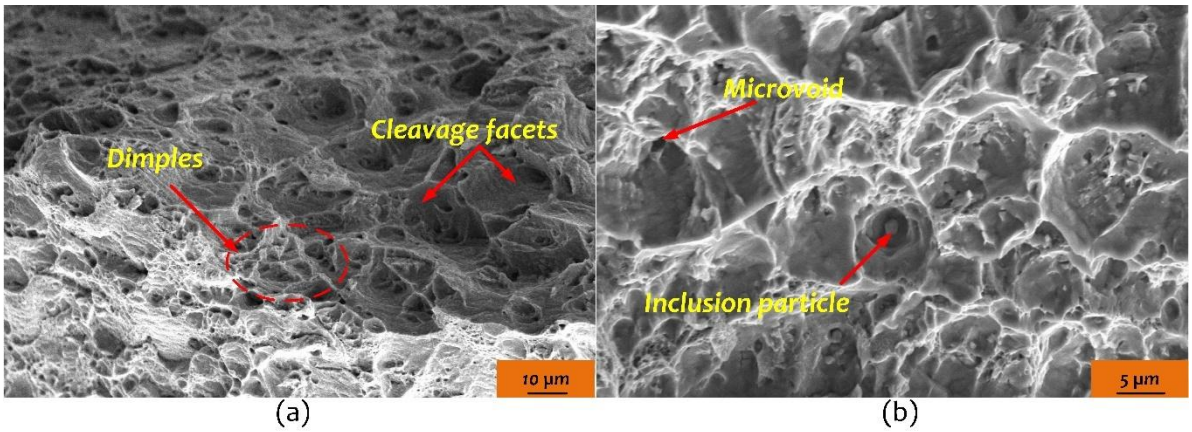


Figure 5.35 : Fractured Charpy impact toughness specimen surface of (a) AW ERNiCrMo-3 filler WFZ (b) PWHT ERNiCrMo-3 filler WFZ

5.4 USING ERNiCrCoMo-1 (INCONEL 617)

5.4.1 Macroscopic Observations

In the first macro-observation made after extracting the weld specimen, as shown in Figure 5.36(a-b), the macrostructure of the weld clearly shows proper filler metal deposition into the groove prepared. The plate of 8 mm thickness seemed successfully welded without any macro defects observable to the naked eye under a microscope. The different filler metal deposition passes made during the weld, such as the root pass, filling pass, capping pass, and backing pass was, deposited well without any clear distinction of layer between them. The P91 weld interface suggests incomplete diffusion and unmixed zone (UZ) formation. The weld interface was thinner in the macro-observation made for the Incoloy 800HT side, and macrosegregation was visible at the P91 and Incoloy 800HT weld interfaces. The DWJ was made in unconstrained conditions to observe the angular distortion (θ) produced with the presented V-groove geometry and to compute the residual stresses produced in the unconstrained as-welded (AW) state. The angular distortion was measured to account for the deformation that occurred in the welded plate due to thermal strains produced by welding thermal cycles. The average angular distortion of 2.8° was measured for different locations.

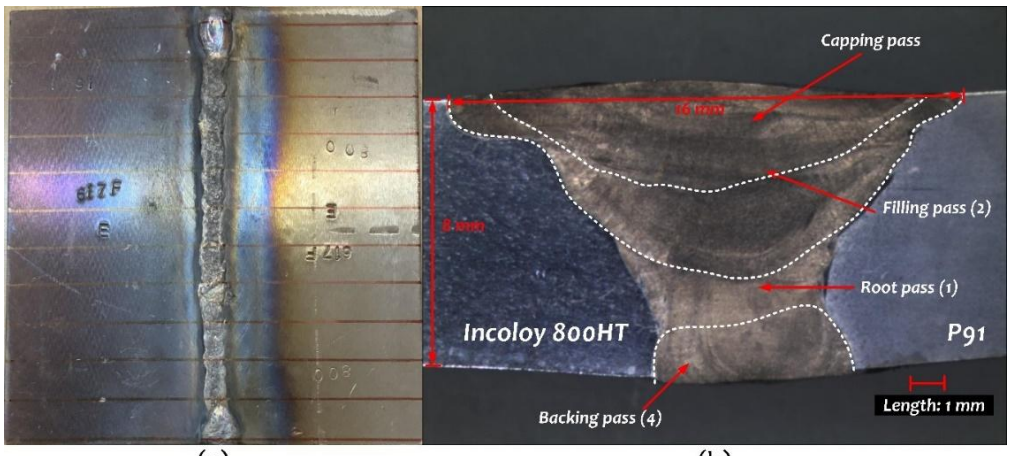


Figure 5.36 : (a) Welded plate in as-welded (AW) state (b) Macrostructure of the weld bead in the as-welded condition

5.4.2 Heat Affected Zone (HAZ) Microstructure Characterization

The base metals and filler metals generally melt at around 1538 ℃. The temperature can reach up to 3000 ℃ during GTAW in a localized region. The base metals near the weld interface were exposed to different thermal peak temperatures during the welding. Exposure to different peak temperatures leads to the formation of HAZ. The CGHAZ was formed just near the weld interface of P91. CGHAZ formation has been accounted for due to exposure above the Ac_3 transformation temperature. The CGHAZ region in AW condition was observed with untempered lath martensite. Since the temperature in the CGHAZ region is much above the transformation temperature, the observed precipitates, such as M23C6 and MC, get dissolved into the matrix, and grain boundaries coarsened. Due to the dissolution of the precipitates in the region, the pinning action on grain boundaries gets reduced, and PAGB grows. The same can be observed in the optical and FESEM micrograph in Figure 5.37(a, d). Some undissolved precipitates were spotted in the inset FESEM micrograph, which could be M_3C and NbX phases as they dissolve at a temperature higher than 1200 ℃, as reported by (Yoshino et al., 2005). Further, far away from the P91 weld interface and adjacent to the CGHAZ region, FGHAZ was formed as it was exposed to a temperature just above Ac_3. The FGHAZ region was found with a low length to width ratio of martensite blocks in the fine PAGBs. The low temperature in the FGHAZ restricts the PAGB growth as precipitates were only partially dissolved, and the undissolved coarsened precipitates provided the pinning action at PAGBs. The FGHAZ microstructure features like PAGBs and precipitates can be observed in Figure 5.37(b,e). ICHAZ was observed further away from the P91 weld interface adjacent to FGHAZ. ICHAZ region was exposed to temperatures between Ac_1 and Ac_3. The ICHAZ region (Figure 5.37(c,f)) was observed with the formation of untempered lath martensite, partially dissolved precipitates at PAGBs, coarsened precipitates, and over-tempered martensite. ICHAZ had a higher density of precipitates when compared to FGHAZ or CGHAZ. It was observed that the ICHAZ region and over-tempered base metal region were very narrow in the range of only a few hundred micrometers. Hence, it is difficult to distinguish and identify the precise region. Table 5.4 describes the point analysis EDS spectra obtained for different locations and precipitates observed in AW CGHAZ, FGHAZ, and ICHAZ regions.

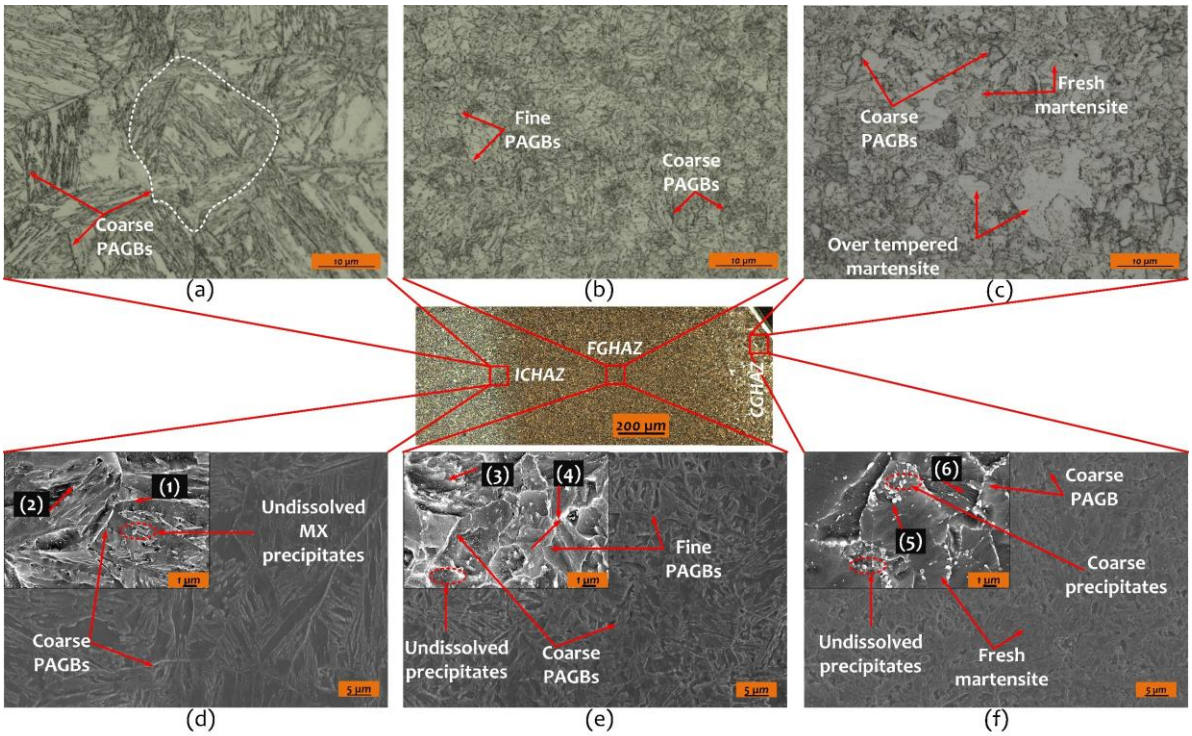


Figure 5.37 : Optical and SEM micrographs of different zones of AW P91 HAZ (a,d) CGHAZ (b,e) FGHAZ (c,f) ICHAZ

Table 5.4 : EDS spectra for positions observed in Figure 5.37

Element Weight %	*C*	*V*	*Cr*	*Mn*	*Fe*	*Nb*	*Mo*	*W*
Matrix at position [1]	10.52	0.65	15.89	0.69	78.74	0.24	3.15	0.12
Precipitate at position [2]	6.98	0.21	7.91	0.46	83.36	0.08	0.75	0.25
Matrix at position [3]	8.62	0.18	8.27	0.44	81.36	0.06	0.92	0.15
Precipitate at position [4]	11.45	0.72	18.52	0.77	75.86	0.15	2.45	0.08
Matrix at position [5]	12.25	0.82	16.26	0.63	76.49	0.29	2.86	0.4
Precipitate at position [6]	10.25	0.17	8.48	0.48	79.26	0.1	0.88	0.38

It is recommended to put the P91 HAZ to post-weld heat treatment (PWHT) to homogenize the microstructure features observed in the AW condition. The PWHT was carried at an Ac_1 temperature of 760 ℃ for 2 hours to eliminate any drastic effect of the microstructure features developed in the AW state. The PWHT does not produce any observable change in grain size. CGHAZ region of P91 after PWHT showed the presence of fresh fine precipitates on PAGBs, martensite lath boundaries, and matrix, as shown in Figure 5.38(a). The tempering at 760 ℃ satisfactorily tempered all untempered martensite present in the AW P91 HAZ. After PWHT, FGHAZ, and ICHAZ, due to their smaller grain size, displayed a more dense evolution of fresh fine precipitates on PAGBs and matrix, as shown in Figure 5.38(b,c). Table 5.5 describes the point analysis EDS spectra obtained for different locations and precipitates observed in CGHAZ, FGHAZ, and ICHAZ regions. (Fei et al., 2020) also observed similar changes in P91 HAZ in AW and PWHT states, supporting the present study's observations. Figure 5.39(a,b) shows the normal distribution of grain size in CGHAZ in AW and PWHT states. The CGHAZ region suffers a nonuniform increase in grain size due to high heat input. The average grain size observed in AW and PWHT states was 35 µm and 39 µm, respectively. The grain size variation has been reported to be in the range of 5-80 µm for T91 CGHAZ (Kumar et al., 2022). Also, Figure 5.39(c,d) shows the denser distribution of the FGHAZ grain size gradient. The FGHAZ in AW and PWHT state observations had an average grain size of 11 µm and 11 µm, respectively. FGHAZ was a broad region with a fine grain size gradient. And, ICHAZ in AW and PWHT state (Figure 5.39(e,f)) had grain sizes of 12 µm and 13 µm, respectively. The PWHT does not have any observable effect on the grain size. The grain size of FGHAZ and ICHAZ were comparable to the average grain size observed for P91 base metal.

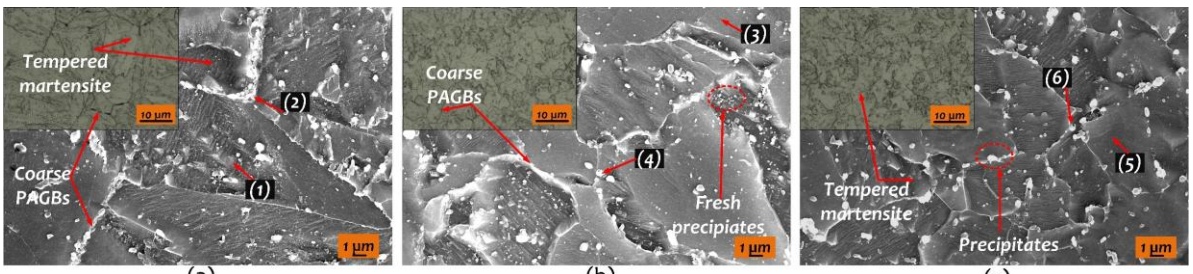


Figure 5.38 : Optical and SEM micrographs of different zones of PWHT P91 HAZ (a) CGHAZ (b) FGHAZ (c) ICHAZ

Table 5.5 : EDS spectra for positions observed in Figure 5.38

Element Weight %	*C*	*V*	*Cr*	*Mn*	*Fe*	*Nb*	*Mo*	*W*
Matrix at position [1]	6.95	0.36	8.6	0.48	82.11	0.08	0.88	0.54
Precipitate at position [2]	8.18	0.62	18.52	0.74	66.79	0.74	3.52	0.89

Matrix at position [3]	9.94	0.23	7.28	0.53	80.62	0.06	0.82	0.52
Precipitate at position [4]	10.36	0.48	16.13	0.72	68.79	0.65	2.18	0.69
Matrix at position [5]	5.68	0.15	7.94	0.64	84.23	0.15	0.76	0.45
Precipitate at position [6]	9.71	0.64	18.92	0.82	65.68	0.67	2.68	0.88

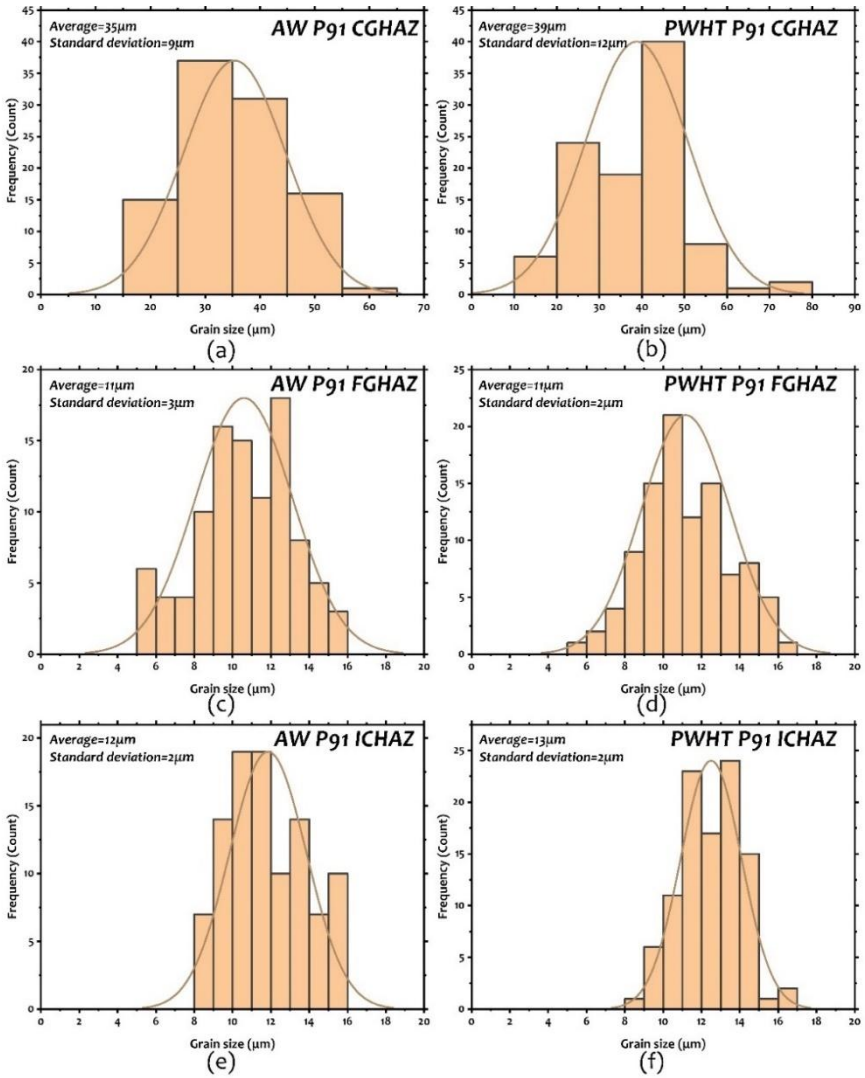


Figure 5.39 : Normal distribution of grain size observed in (a) AW P91 CGHAZ (b) PWHT P91 CGHAZ (c) AW P91 FGHAZ (d) PWHT P91 FGHAZ (e) AW P91 ICHAZ (f) PWHT P91 ICHAZ

Incoloy 800HT was observed with austenite microstructure due to the presence of a high weight percentage of Ni and Nb in the base metal composition. The Incoloy 800HT HAZ near weld interface in AW state was difficult to distinguish even from the base metal. A similar observation was made in a similar study where HAZ did not display any significant change in grain size, although phase transformation was witnessed (Palanivel et al., 2021). Due to the low conductivity of Incoloy 800HT, the HAZ formed is narrower when compared to the P91 HAZ width. However, the austenitic grains are just near and adjacent to the Incoloy 800HT weld interface in the AW state, as shown in Figure 5.40(a,c). The grain size was found to increase for the grains near the weld interface. Precipitates were coarsened in the observed HAZ region. Also, limited thickening of some grain boundaries very near the weld interface was observed. The thickening was reported by Lippold (Lippold, 1984) and (Saito et al., 1987) due to the deposition of Ti at grain boundaries from the austenitic matrix. In the AW state, the Incoloy 800HT HAZ had cuboidal precipitates (Ti(C,N)), which are stable at high temperatures, but carbide precipitates were dissolved into the matrix.

Incoloy 800HT has a very stable microstructure and generally does not respond to the PWHT at Ac_1 temperature. However, after PWHT, fresh carbide particle ($M_{23}C_6$) precipitation was observed in Incoloy 800HT HAZ as the Ti deposited over the grain boundaries provides rapid cooling and extensive precipitation Figure 5.40(b,d). This also leads to coarsening of grain boundaries, but no significant coarsening of grain boundaries was observed after PWHT. Table 5.6 provides the point analysis EDS spectra obtained for different locations and precipitates observed in Incoloy 800HT HAZ in AW and PWHT states. The grain size distribution observed for Incoloy 800HT HAZ in the PWHT state had a negligible effect on the grain size, as the average grain was 181m in the AW state and 180m in the PWHT state.

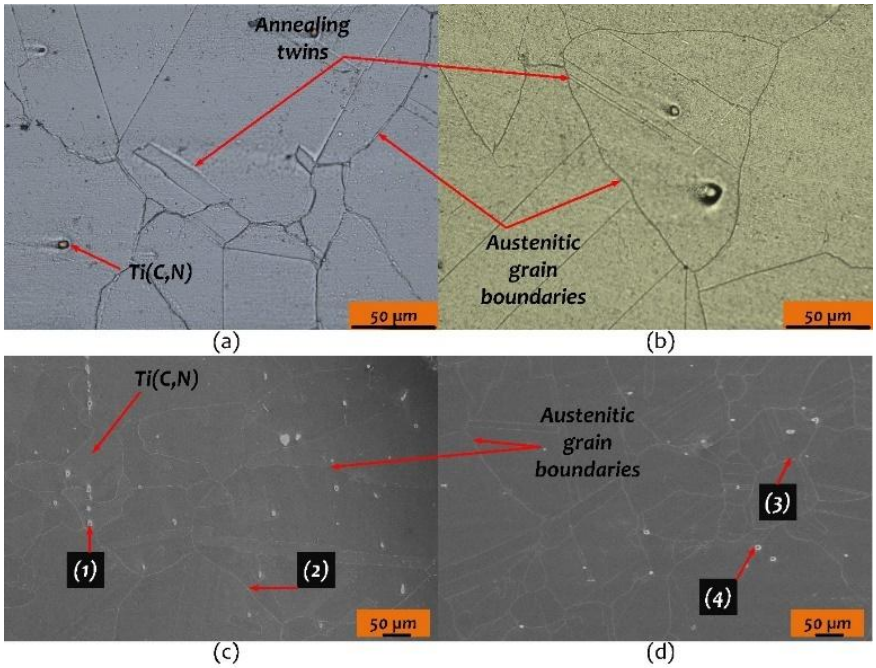


Figure 5.40 : (a) Optical image of Incoloy 800HT HAZ in AW condition (b) Optical image of Incoloy 800HT HAZ in PWHT condition (c) SE image of Incoloy 800HT HAZ in AW (d) SE image of Incoloy 800HT HAZ in PWHT condition

Table 5.6 : EDS spectra for positions observed in Figure 5.40

Element Weight %	*C*	*Si*	*Ti*	*Cr*	*Mn*	*Fe*	*Ni*	*Nb*
Precipitate at position [1]	3.33	0.76	19.42	16.48	0.96	32.70	22.65	3.69
Grain boundary at position [2]	0.01	0.98	0.94	20.94	1.38	41.97	31.10	29.54
Precipitate at position [3]	-	-	51.04	11.19	-	18.56	13.90	5.31
Grain boundary at position [4]	9.97	-	9.88	25.10	2.42	37.84	14.41	0.38

5.4.3 Weld Interface and Weld Fusion Zone (WFZ) Microstructure Characterization

Despite designing a V-groove and using matching filler metal, it is complicated to predict the location of weld interface formation. Based on the AW P91 weld interface observation shown in Figure 5.41, incomplete fusion was witnessed along the major part of the P91 weld interface. This was due to the difference in thermophysical properties of P91 base metal and ERNiCrCoMo-1 filler metal. The difference in melting temperatures, solidification temperatures, coefficient of thermal expansion (CTE), and chemical composition hinders in melting of the base metal and fuse into the weld. So, the incomplete mixing of base metal with filler metal leads to the formation of UZ. The UZ can be observed as a narrow zone along with the P91 weld interface. Further, macrosegregation was observed, i.e., solute segregation at a macroscopic level. Macrosegregation is the term used to describe the UZ features. These filler deficient features observed in Figure 5.41 are island

and peninsula. Peninsulas and islands are formed when the base metal experiences a liquidus temperature higher than the bulk WFZ liquidus temperature. (Soysal et al., 2016) described the macrosegregation mechanism and reported its tendency to reduce toughness and introduce stress-corrosion cracking. Type II boundary was also seen running parallel to the P91 weld interface. (Sireesha et al., 2000) described that the presence of a type II boundary indicates the transition of solidification behavior from ferritic to austenitic and allotropic transformation on the P91 side. The weld interface is a critical region. The grain growth and structure at the weld interface directly impact the mechanical properties of the weld. At the weld interface, the solidification mechanics come into play where the microstructure of the WFZ is dependent on the temperature gradient (G)(℃/m) in the weld pool and growth rate (R)(μm/s) of the solidifying cell or dendrite. The G/R ratio determines the solidification mode, length, and spacing of cells and dendrites. In relation to the present study, low G/R ratios are observed generally, and the presence of high solute concentration gives cellular, equiaxed, or columnar dendritic growth. Since, in M-TIG, multiple welding thermal passes affect the solidification rate and temperature gradient for interpass layers, which may lead to the formation of mixed grain structure in the weld pool. Based on the described phenomenon, the cellular, columnar, and equiaxed dendritic growth was observed heterogeneously distributed in the WFZ near the P91 weld interface. In the line map, the EDS spectrum shown in Figure 5.42 for the P91 weld interface in the AW state, variation in Fe, Cr, and Ni was observed. In contrast, minor constituents do not show any significant variation. The UZ shows the distribution of the elements similar to P91 base metal. In EPMA analysis at the P91 interface, as shown in Figure 5.43, the back-scattered electron (BSE) image of P91 suggests segregation around the precipitates. The EPMA results show the elemental composition differences across the P91 weld interface. Fe, Ni, and Cr diffusion was confirmed near the weld interface. WFZ seems to have Ti-rich precipitates distributed near the weld interface. No significant diffusion across the weld interface was observed, though Al-rich precipitates in the P91 matrix suggest the presence of rare AlN particles. However, Mo tends to segregate across the grain boundaries, but no active diffusion can be confirmed based on the qualitative EPMA analysis. Co-rich and Mo-rich phases were sparsely distributed in the matrix.

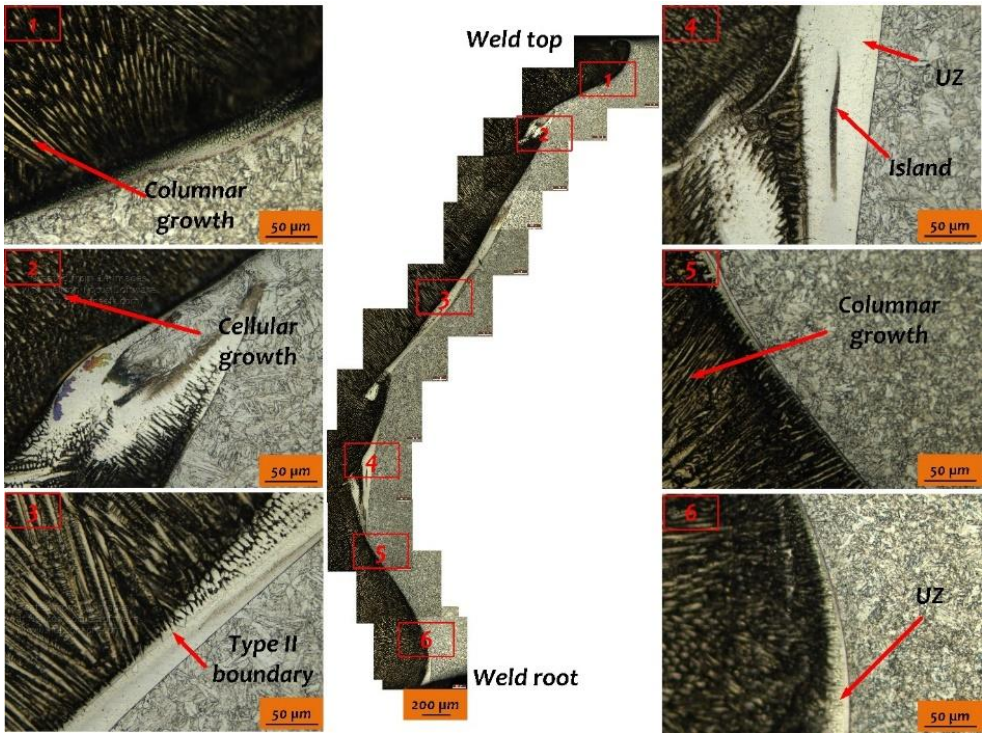


Figure 5.41 : P91 weld interface in AW state optical images

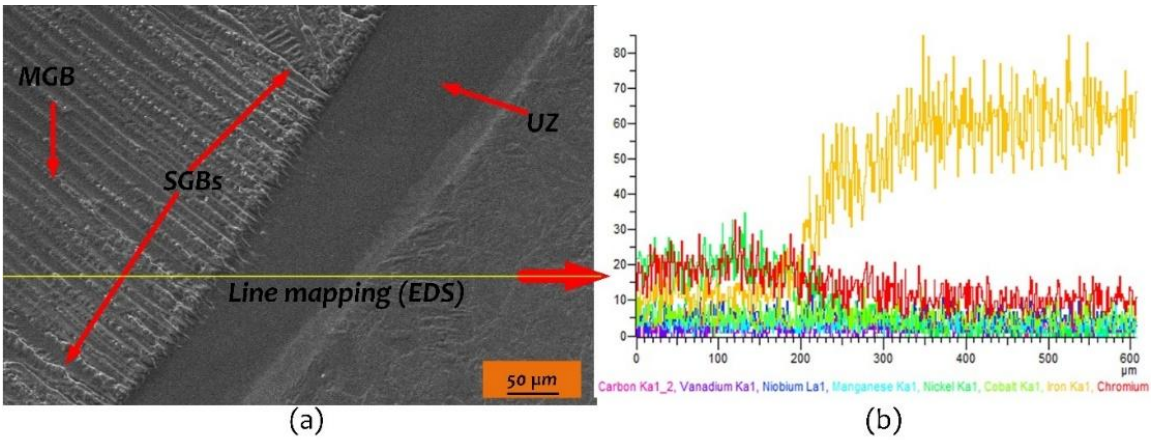


Figure 5.42 : (a) SEM image for AW P91 weld interface (b) Line map EDS analyses along the P91weld interface

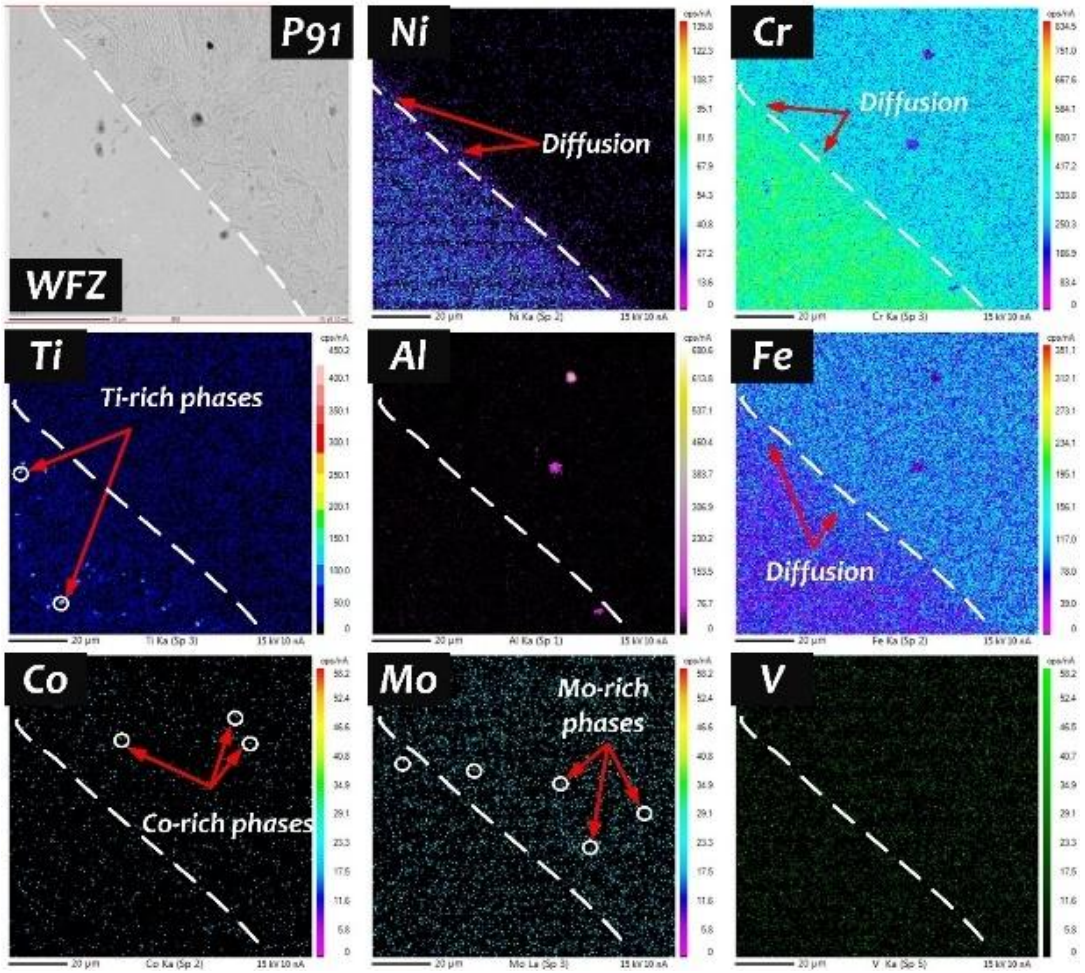


Figure 5.43 : EPMA analysis for P91 weld interface

The AW Incoloy 800HT weld interface is shown in Figure 5.44. The ERNiCrCoMo-1 filler metal has properties more inclined with Incoloy 800HT, so better fusion was observed at the Incoloy 800HT weld interface. The partially mixed zone (PMZ) formation was observed immediately outside the WFZ. PMZ is formed due to incomplete mixing of the liquated weld pool and resolidifying near the weld interface. PMZ deteriorates the mechanical properties of the DWJ and is prone to heavy segregation due to differences in concentration gradients in the PMZ. The Incoloy 800HT and ERNiCrCoMo-1 filler metal both have fcc crystal order and hence, the Incoloy 800HT weld interface has shown epitaxial growth. The epitaxial growth in WFZ starts from the partially melted Incoloy 800HT grains

at the weld interface. Again, macrosegregation, the filler deficient zones were observed at the Incoloy 800HT weld interface. Near the weld interface of Incoloy 800HT (Figure 5.45(a)), cellular, equiaxed, and columnar dendritic growth packets were located and randomly distributed with different orientations. The line map EDS spectra (Figure 5.45(b)) across the AW Incoloy 800HT weld interface show composition elemental variation across the weld interface for Fe, Ni, and Mo. No significant variation was observed for minor constituent elements. The EPMA analysis for the Incoloy 800HT weld interface has been shown in Figure 5.46. The BSE image of the weld interface shows heavy precipitation and coarsening at the Incoloy 800HT HAZ grain boundary. The presence of Al, Ti-rich precipitate hints at the presence of the γ'-phase, which is the primary strengthening phase in Ni-based alloys. EPMA analysis confirmed heavy Ti-concentration over the Incoloy 800HT grain boundary in the HAZ region. Also, WFZ has a significant number of Ti-rich precipitates with Cr segregation in the interdendritic regions. Also, the diffusion of Fe into WFZ was clearly confirmed in EPMA analyses.

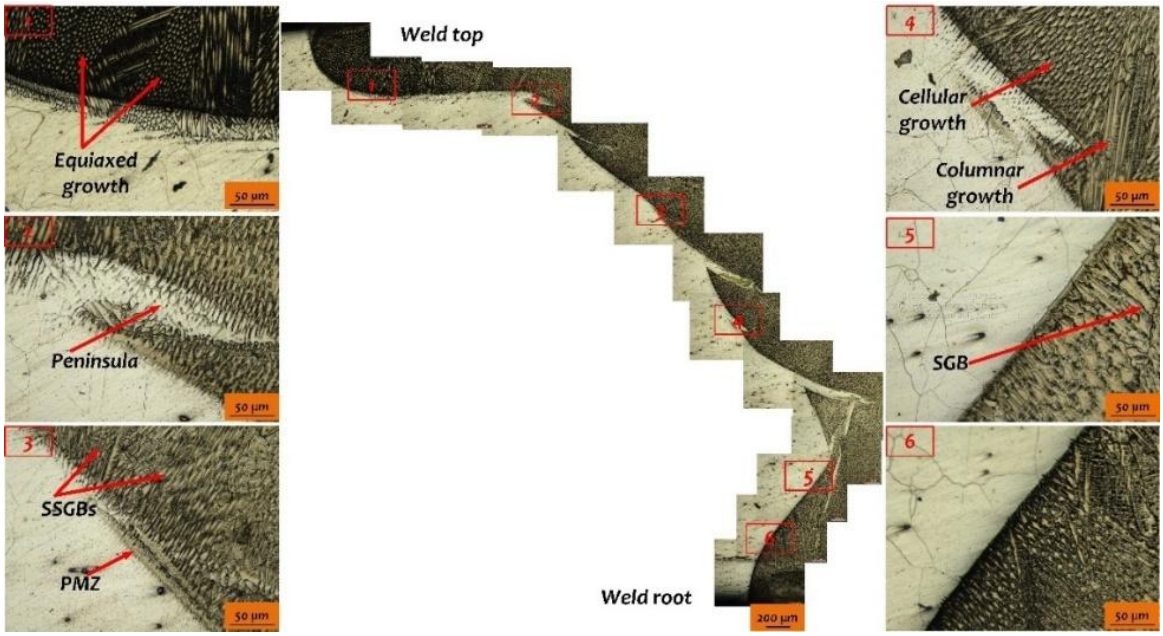


Figure 5.44 : Incoloy 800HT AW state weld interface optical images

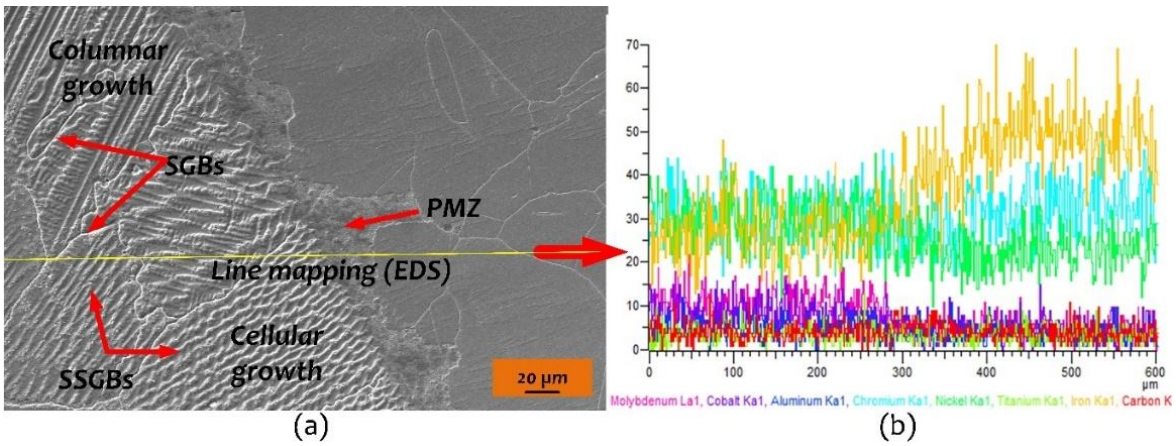


Figure 5.45 : (a) FESEM image for AW Incoloy 800HT weld interface (b) Line map EDS analyses along Incoloy 800HT weld interface

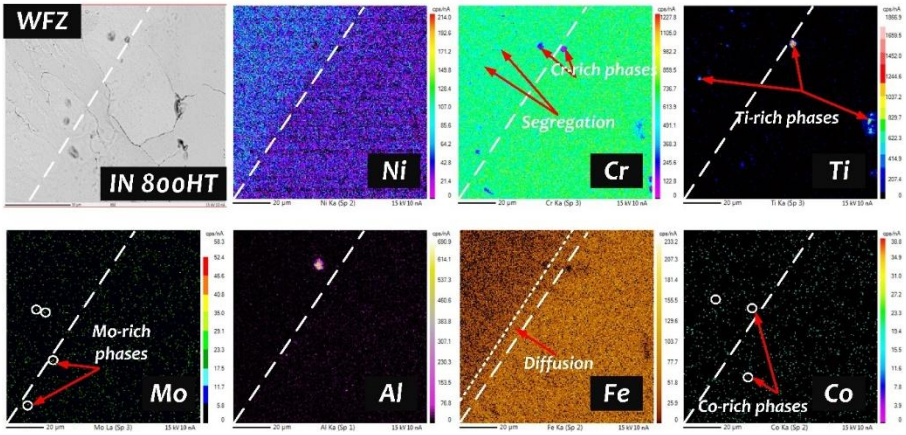


Figure 5.46 : EPMA analysis for P91 weld interface

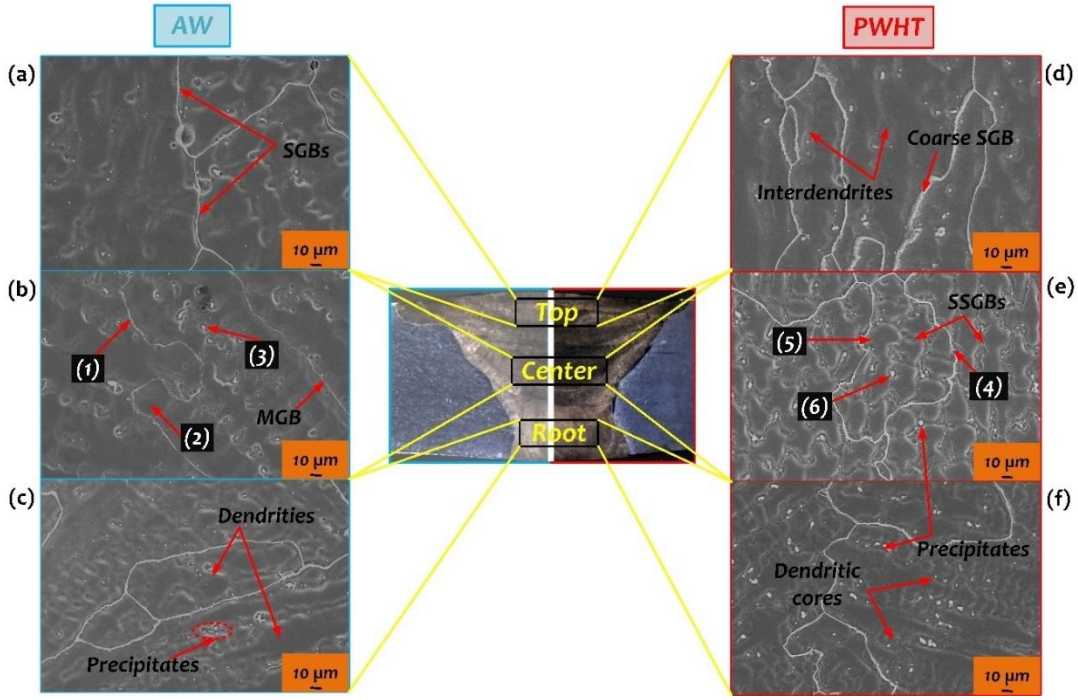


Figure 5.47 : SEM micrograph of WFZ taken at (a) top AW WFZ region (b) center of AW WFZ (c) root of AW WFZ (d) top PWHT WFZ region (e) center of PWHT WFZ (f) root of PWHT WFZ

The Schaeffler diagram has also been used to predict the mode of solidification. The Cr_{eq} and Ni_{eq} were calculated using equations (5.1) and (5.2) and then plotted on the Schaeffler diagram, as shown in Figure 5.5. The elemental composition of WFZ was obtained using OES. The weight percentage of elements was as follows: Carbon (C): 0.06, Manganese (Mn): 0.1, Molybdenum (Mo): 9.2, Aluminum (Al): 2.1, Titanium (Ti): 0.39, Tungsten (W): 0.14, Iron (Fe): 4.4, Silicon (Si): 0.08, Chromium (Cr): 21.3, Nickel (Ni): 51.5, Niobium (Nb): 0.01, Vanadium (V): 0.035, and Cobalt (Co): 10.1. The higher weight percentage of Ni in Incoloy 800HT base metal and filler metal deposited in WFZ gives a high $Ni_{eq,}$ which was extrapolated and fall in the austenitic region of the Schaeffler plot. The WFZ has an austenitic solidification mode. As in Figure 5.47(a-f), the WFZ has cellular, equiaxed, and columnar dendritic growth. Now, the weld solidifies into subgrain in the form of cells or dendrites. These cell packets and dendrite packets are separated by the boundaries known as SGBs or high-angle grain boundaries. At the end of solidification, MGBs are formed due to the migration of the high-energy crystallographic component of SGB away from its compositional component. While SSGBs are the product of solute redistribution during solidification. SSGB represents the boundary separating the adjacent cell or dendrite, and the compositional difference can be found at an SSGB. Table 5.7 gives the point analyses EDS

spectrum for different locations and precipitates observed in the WFZ in AW and PWHT states. PWHT does not significantly affect WFZ and Incoloy 800HT HAZ as Incoloy 800HT and ERNiCrCoMo-1 do not respond to PWHT at 760 ℃. This can be supported by the work of (Bhaduri et al., 1995). But, at this temperature, carbide ($M_{23}C_6$) precipitation has been expected to occur in WFZ and Incoloy 800HAZ.

Table 5.7 : EDS spectra for positions observed in Figure 5.47

Element weight %	*C*	*Al*	*Ti*	*Cr*	*Fe*	*Co*	*Ni*	*Nb*	*Mo*
SGB at position [1]	5.82	1.14	0.39	21.25	12.38	7.31	42.49	0.28	8.94
Dendrite at position [2]	4.25	0.54	0.16	20.16	14.52	9.82	46	0.18	4.37
Precipitate at position [3]	8.25	0.93	1.85	20.82	9.45	7.18	24.52	0.48	26.52
SGB at position [4]	6.25	0.89	0.42	22.37	13.88	8.17	38.56	0.14	9.32
Dendrite at position [5]	3.97	0.44	0.28	19.01	17.43	9.66	43.27	0.12	5.82
Precipitate at position [6]	10.85	0.61	2.12	21.85	7.85	6.52	21.06	0.62	28.52

Further, with the solidification of the molten weld pool in WFZ, it is impossible to avoid the microsegregation phenomenon from occurring. Microsegregation can occur even at room temperature, but it is rare to observe this phenomenon in a solid state or at Ac_1 temperature. Again, in a study by Caron and Sowards (Caron and Sowards, 2014), microsegregation has accounted for the compositional difference between the dendritic core and interdendritic regions (with more solute). The EPMA analysis to observe the microsegregation across the cell boundary has been shown in Figure 5.48. The Cr was observed clearly segregated into dendritic cores. No segregation was witnessed for Mo, but it was uniformly distributed. Ti-rich precipitates were found well distributed in WFZ and Incoloy 800HT HAZ. Further, Al seems to have segregated into interdendritic regions and possibly formed γ'-phase. Mo and Co were uniformly present in the matrix, with their precipitates distributed randomly.

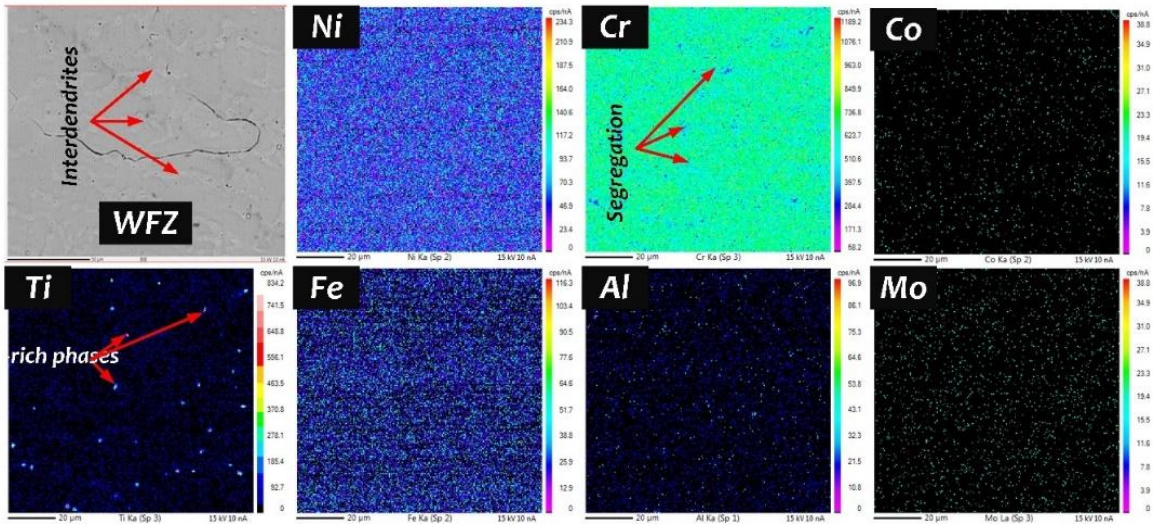


Figure 5.48 : EPMA analysis for ERNiCrCoMo-1 WFZ of P91-Incoloy 800HT DWJ

5.4.4 Residual Stresses

The subsurface residual stresses in the WFZ were observed using the deep hole drilling (DHD) method. The data obtained have been plotted and shown in Figure 5.49. The peak longitudinal and transverse residual stress observed in AW state WFZ at a depth of approximately 2 mm were 195 MPa and 135 MPa, respectively. From the top face of WFZ to

a depth of 5 mm, tensile levels of residual stresses were recorded in the WFZ. The WFZ mode of solidification was austenitic, which is associated with shrinkage and producing tensile residual stresses. However, as the angular distortion was observed due to multiple welding thermal cycles, it put the face of WFZ in dominant compression residual stress, and eventually, the WFZ root was put in compression. The longitudinal and transverse residual stress in the AW state WFZ root was a minimum of -35 MPa and -20 MPa, respectively. After PWHT, the residual stresses were completely compressive for the whole observable depth. Stresses were relaxed and were brought nearer to the neutral axis. PWHT changed the longitudinal and transverse to a minimum of -105 MPa and -66 MPa at an approximate 5-6 mm depth. PWHT has been found necessary for improving weld performance (Chen et al., 2020; Dak and Pandey, 2020). At a depth of 7 mm, all the residual stresses were almost relaxed and were nearest to the neutral axis. After PWHT, compressive stresses might have developed due to phase transformation in the P91 HAZ, and as a result, WFZ experienced overall compression. The DHD method fails to give data for a precise location, but it can give realistic and consistent measurements for the residual stresses induced during welding, as reported by (Skouras et al., 2013). The development of welding residual stresses has been observed to be highly influenced by volumetric transformations and transformation induced plasticity (TRIP) during weld solidification (Li et al., 2021).

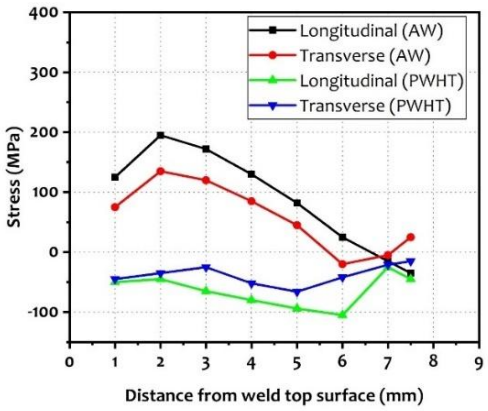


Figure 5.49 : Residual stress variation profiles for WFZ in AW and PWHT states

5.4.5 Tensile Properties

The ultimate tensile strength (UTS), yield strength (YS), elongation percentage, and reduction in area percentage were observed in cross-weld tensile testing at room temperature. Table 5.8 has the details of the tensile testing results obtained for the prepared specimens. A general observation was the failure occurring from base metal Incoloy 800HT in standard tensile specimens for both AW and PWHT conditions, but the AW and PWHT state subsize tensile specimen failed from WFZ (Figure 5.50). In standard tensile specimen failure from base metal, Incoloy 800HT was expected since it has a lower tensile strength in comparison to P91 base metal. At the same time, subsize tensile specimens were prepared such that failure occurred from WFZ to observe the WFZ tensile strength. A similar study conducted for a dissimilar weld between a superalloy Incoloy 825 and AISI 321 SS failure was observed at SS base metal, confirming the greater tensile strength of the weld fusion zone (Sayyar et al., 2020). The UTS observed for AW standard tensile specimen and PWHT standard tensile specimen was 532 MPa and 544 MPa, respectively, with a standard deviation of 4 MPa. The increase in tensile strength after PWHT might be due to the precipitation of fresh carbides in the Incoloy 800HT base metal. Coherently, the elongation percentage dropped from 40% to 32%. The elongation percentage is significantly higher than that observed for base metal Incoloy 800HT, which might be attributed to exposure to high peak temperature during welding, possibly increasing the grain size. The YS for the AW standard tensile specimen was 230 MPa, and the PWHT standard tensile specimen increased

to 239 MPa. (Lakshmanan et al., 2019) also observed the failure of Incoloy 800HT base metal in a similar study. The AW subsize tensile specimen witnessed a UTS of 550 MPa with a standard deviation of 5 MPa, while the PWHT subsize tensile specimen's UTS increased significantly to 584 MPa with a standard deviation of 4 MPa. The PWHT was observed with the highest UTS, and this value is comparable to the UTS observed by (Shah Hosseini et al., 2011) for a similar filler metal. The observed carbide precipitation and presence of the γ'-phase in WFZ imparts the observed strength. WFZ seems to respond to PWHT, which could have possibly precipitated more carbides. After PWHT, for subsize specimens, the elongation percentage dropped from 57% to 33%. The WFZ tensile strength observed was low but comparable to the tensile strength of the Incoloy 800HT base metal. Also, it is important to notice that standard tensile specimens in both AW and PWHT state failed from base metal Incoloy 800HT side with UTS of 532 MPa and 544 MPa, respectively, while subsize specimens failed from WFZ, witnessing a comparably higher UTS in both cases. In support of the observed results, (Pavan et al., 2015) also observed the failure at the base metal side during tensile testing, and the tensile strength of WFZ was reported to be higher than the base metal. ("ASTM A335 / A335M - 21 Standard Specification for Seamless Ferritic Alloy-Steel Pipe for High-Temperature Service," 2003) and (ASTM B409, 2011) recommend the minimum elongation to failure of 30% for both P91 and Incoloy 800HT, respectively. And the observed minimum elongation percentage was for PWHT standard tensile specimen 33%, so the DJW qualifies as per the ASTM standards. The engineering stress-strain curves obtained have been plotted in Figure 5.50.

Table 5.8 : Tensile properties for different weld specimens

Specimens	*UTS (MPa)*	*YS [offset 0.2%] (MPa)*	*Elongation (%)*	*Reduction in area (%)*	*Failure location*
AW (Standard specimen)	532 ± 4	230 ± 5	40 ± 2	77 ± 2	Incoloy 800HT BM
AW (Subsize specimen)	550 ± 5	-	57 ± 2	69 ± 3	WFZ
PWHT (Standard specimen)	544 ± 4	239 ± 6	32 ± 2	74 ± 3	Incoloy 800HT BM
PWHT (Subsize specimen)	584 ± 4	-	33 ± 3	57 ± 3	WFZ

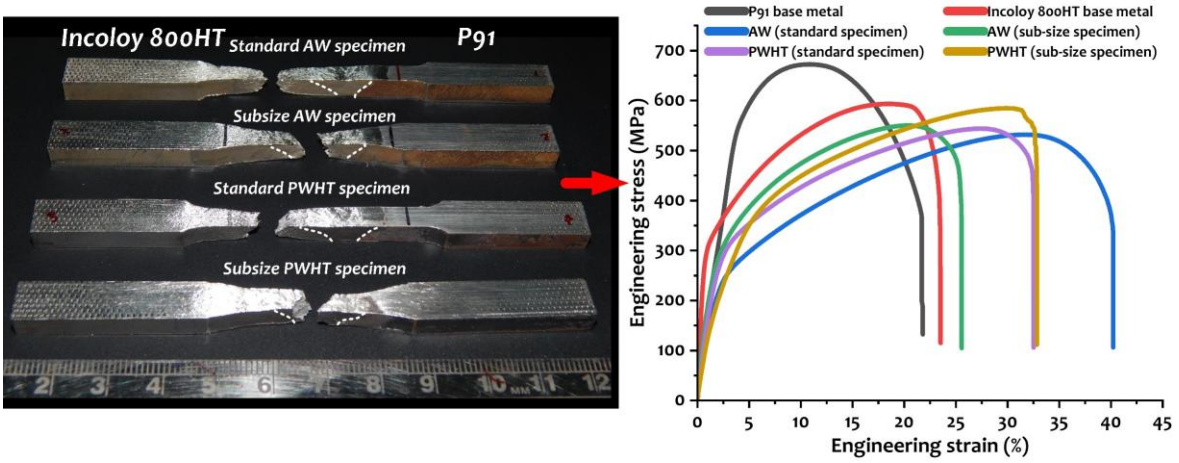


Figure 5.50 : Fractured tensile samples and engineering stress-strain curves for different specimens

A fractography investigation was done to determine the mode of failure in different tensile specimens broken. Figure 5.51(a,c) shows fractured surface AW and PWHT standard tensile specimens, respectively. Since the standard specimen failed from the ductile Incoloy 800HT base metal, both surfaces have a dominant formation of microvoids, macro voids, and different size dimples distributed non-uniformly. Cleavage facets were also visible, suggesting a mixed mode of failure. However, appreciable necking and elongation were observed in the broken standard AW and PWHT tensile specimen, suggesting the ductile

mode of failure dominance. Figure 5.51(b,d) shows the fractured surfaces of AW subsize tensile specimen and PWHT subsize tensile specimen, respectively. Both surfaces have a clear presence of cleavage facets, and tear ridges account for the brittle nature. Also, small size shallow dimples were spotted on the subsize specimen's broken surface. The presence of macro voids in both specimens confirms the shear ductile mode of fracture, in which band formation on inclusion was restricted, producing localized strain and void nucleation, as reported by (Abbasi et al., 2018).

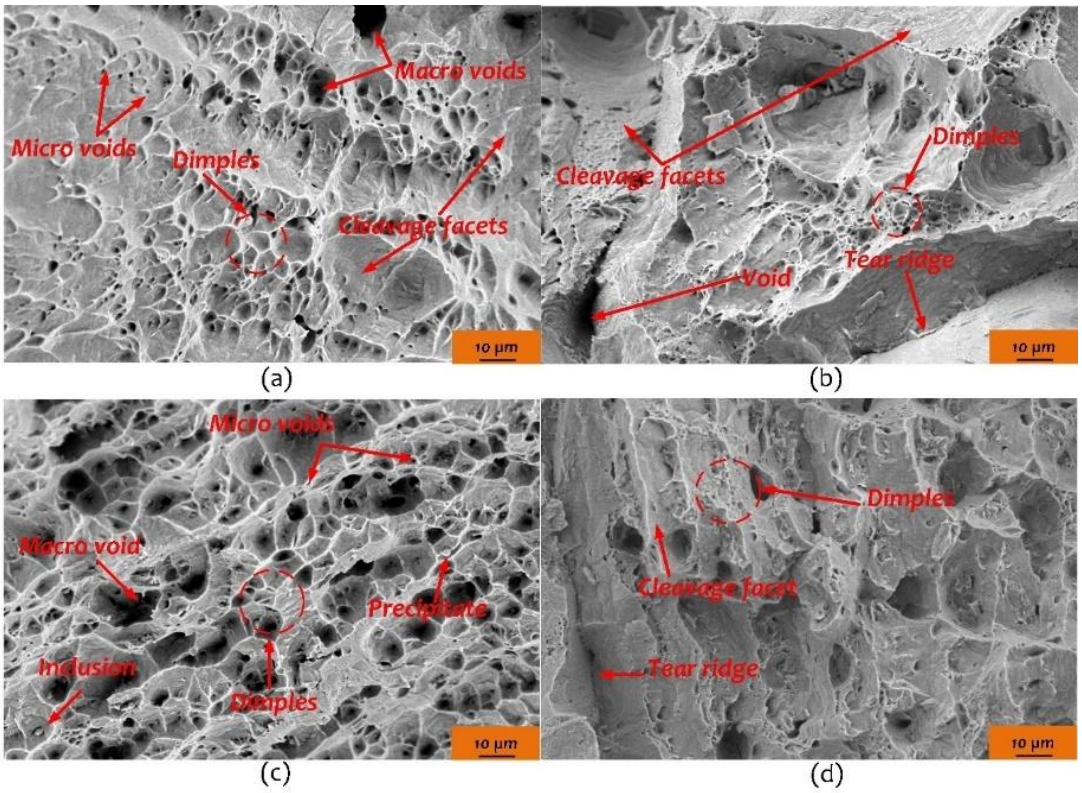


Figure 5.51 : Fractured tensile specimen surface of (a) standard AW tensile specimen (b) subsize AW tensile specimen (c) standard PWHT tensile specimen (d) subsize PWHT tensile specimen

5.4.6 Microhardness Properties

The average microhardness of the P91 base was 245 ± 15 HV, and for Incoloy 800HT base metal, it was 159 ± 20 HV. To assess the mechanical properties imparted by the formation of different phases in WFZ and base metal HAZs, microhardness indents were taken across the WFZ at a gap interval of 0.25 mm. The microhardness plot for the idents taken on the AW specimen has been shown in Figure 5.52. The average WFZ microhardness was 217 ± 30 HV. Though the observed microhardness for ERNiCrCoMo-1 filler metal WFZ was observed to be higher than Incoloy 800HT base and comparable to the observed microhardness of P91 base metal, it was quite low when compared to the microhardness of around 350 HV in the same filler WFZ reported by (Ranjbar et al., 2018). Since finer grain structure imparts higher microhardness, the observed lower microhardness of ERNiCrCoMo-1 filler WFZ could be attributed to the cellular and columnar mode of solidification and possible coarsening of grain boundaries. Also, in M-TIG, due to multiple welding thermal cycles, especially during the filling pass, coarse columnar grain structures could be formed in the center of WFZ, which impart significant anisotropy to the mechanical properties of the weld. However, it can be argued that the WFZ observed in the present study is attributed to lower microhardness due to austenitic structure. The grain boundaries in WFZ, such as SGBs and SSGBs, are high energy regions with high microhardness.

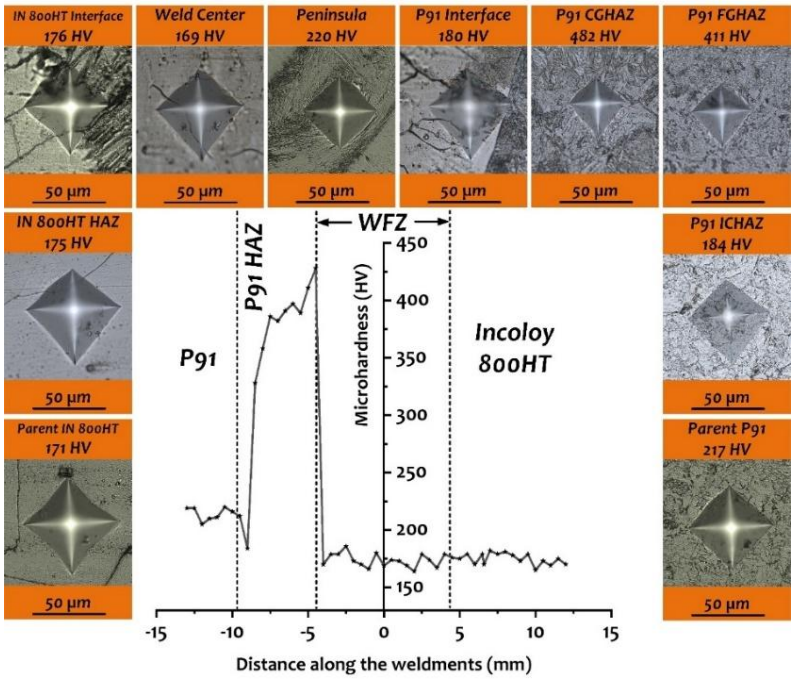


Figure 5.52 : Microhardness variation obtained for AW condition across the P91-Incoloy 800HT DWJ

Similarly, the interdendritic regions have the presence of harder phases, while dendritic cores have lower microhardness with nominal composition. Hence, the inhomogeneous distribution of SGBs, SSGBs, and interdendritic regions causes variations in WFZ microhardness. The Incoloy 800HT AW state HAZ had an average microhardness of 1624 HV; the slight increase can be due to the coarsening of grain boundaries and annealing twins. The P91 CGHAZ average microhardness was witnessed to be 420 ± 4 HV with a maximum microhardness indent of 424 HV. The dissolution of C and N imparts solid solution strengthening in P91; hence, the microhardness increase was observed. In the FGHAZ region, the average microhardness was 379 ± 27 HV, with a maximum of 406 HV microhardness observed in the region. FGHAZ also experiences solid solution strengthening due to partial dissolution of carbide precipitates at peak temperature experienced. The presence of untempered lath martensite also causes a sudden increase in microhardness. ICHAZ also had a similar experience as FGHAZ but was exposed to lower peak temperature, and with the partial dissolution of precipitates, it had over-tempered base metal lath martensite. This imparted the ICHAZ region a microhardness as low as 195 HV.
PWHT was carried out to reduce the variation observed in P91 HAZ. Figure 5.53 shows the microhardness plot observed for the PWHT specimen, and it confirms the reduction in microhardness. PWHT does not significantly affect WFZ as the average microhardness in the region observed was 228 ± 29 HV. A slight increase can be possibly due to fresh carbide precipitation. The Incoloy 800HT HAZ after PWHT shows an average microhardness of 160 ± 3 HV; again, Incoloy 800HT does not, as such, respond to PWHT at Ac_1 temperature. P91 CGHAZ, FGHAZ, and ICHAZ a, after tempering and fresh carbide precipitation on lath boundaries, and PAGBs reappeared from the matrix. Also, existing precipitates were coarsened. This caused the reduction and homogenization of average microhardness in the P91 HAZ region after PWHT. Also, as mentioned earlier, FGHAZ and ICHAZ experience more dense precipitation due to smaller grain size as compared to CGHAZ. Hence, the region did not achieve a uniform trend in microhardness variation. The CGHAZ after PWHT had an average microhardness of 238 ± 15 HV. FGHAZ and ICHAZ were observed with a microhardness of 210 ± 7 HV and 211 HV. It is also important to mention that since ICHAZ was a very narrow region, it was difficult to identify and map the microhardness in that narrow region.

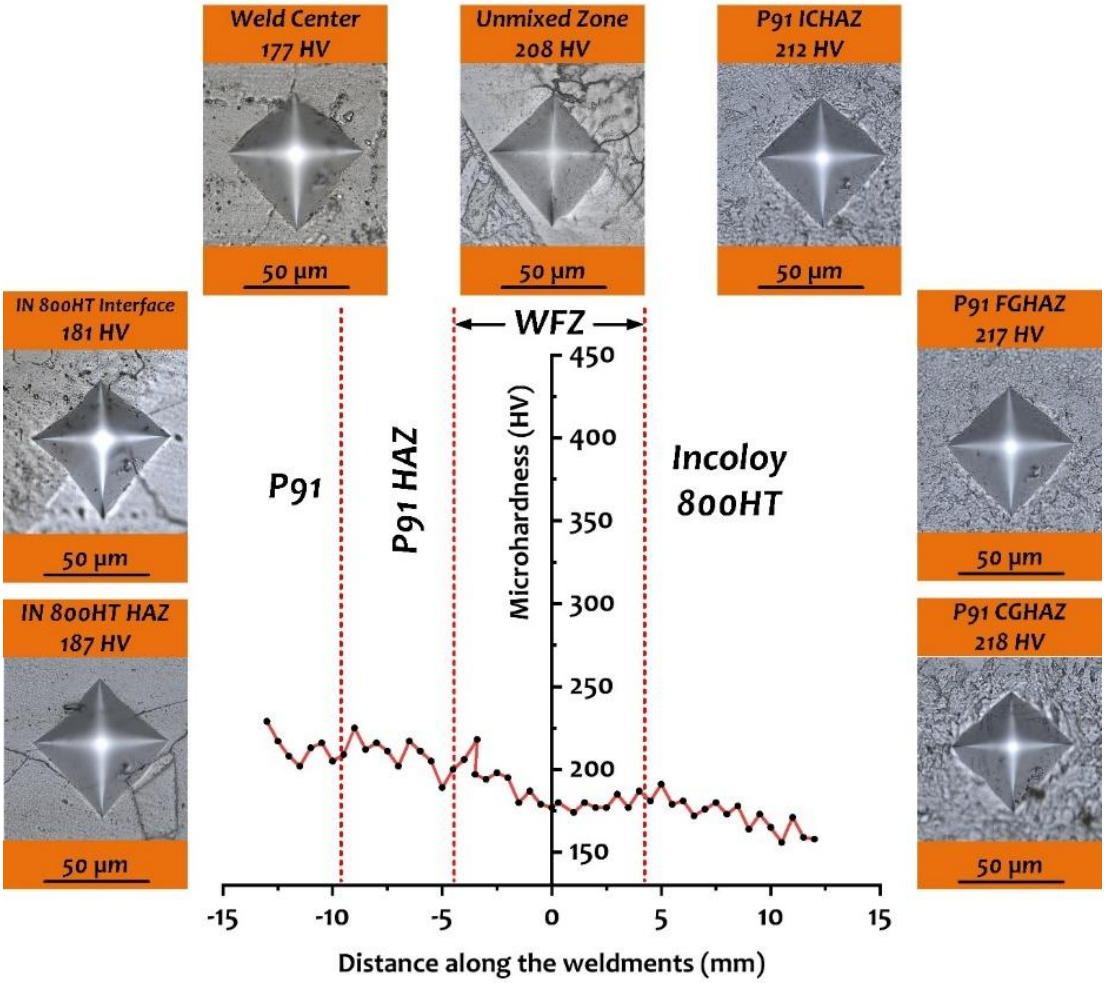


Figure 5.53 : Microhardness variation obtained for PWHT condition across the P91-Incoloy 800HT DWJ

5.4.7 Charpy Impact Toughness

The Charpy impact toughness testing was performed on standard V-notch Charpy specimens. The V-notch was machined along the WFZ to determine the WFZ toughness, as shown in Figure 5.54 (a-b). The toughness was compared for specimens in AW and PWHT states. The broken specimens are shown in Figure 5.54(a-b). The observed Charpy impact toughness for the AW state specimen was 117 ± 5 J (Figure 5.54(a)), and for the PWHT state, it was 102 ± 4 J (Figure 5.54(b)). (Ranjbar et al., 2018) also found the toughness of ERNiCrCoMo-1 filler WFZ of a DWJ and reported the Charpy impact toughness of more than 200 J. The Charpy impact toughness observed in the present study was well above the established benched marked toughness. The WFZ in the AW state produced a higher Charpy impact toughness than the base metal, which could be due to the superior mechanical strength of ERNiCrCoMo-1 filler metal. However, PWHT caused a reduction in Charpy impact toughness. The fractography of broken specimens was performed to analyze the fractured surface. In Figure 5.55(a,b), the uniform distribution of dimples confirms the ductile mode of fracture. However, cleavage facets and secondary intragranular cracks were also observed, suggesting a hybrid mode of failure. The dimple restricted fracture growth, but the fracture surface micrograph shows dimples isolated by planes. This caused the intergranular fracture and promoted quick fracture along the planes. Figure 5.55(c,d) shows the surface of the PWHT state specimen, and no significant changes were observed, but precipitation in WFZ and segregation may have imparted some brittleness in the microstructure, reducing the ductility.

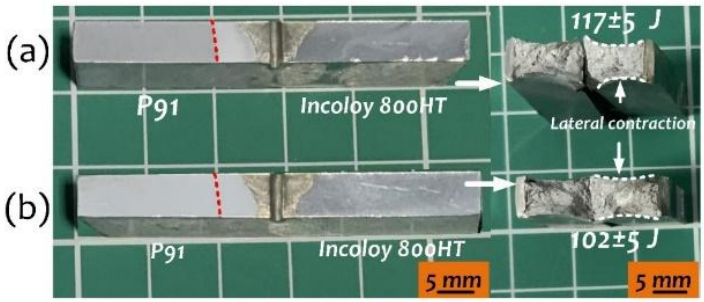


Figure 5.54 : (a) Position of the notch in WFZ in AW state specimen and after fracture specimen (b position of the notch in WFZ in PWHT state specimen and after fracture specimen

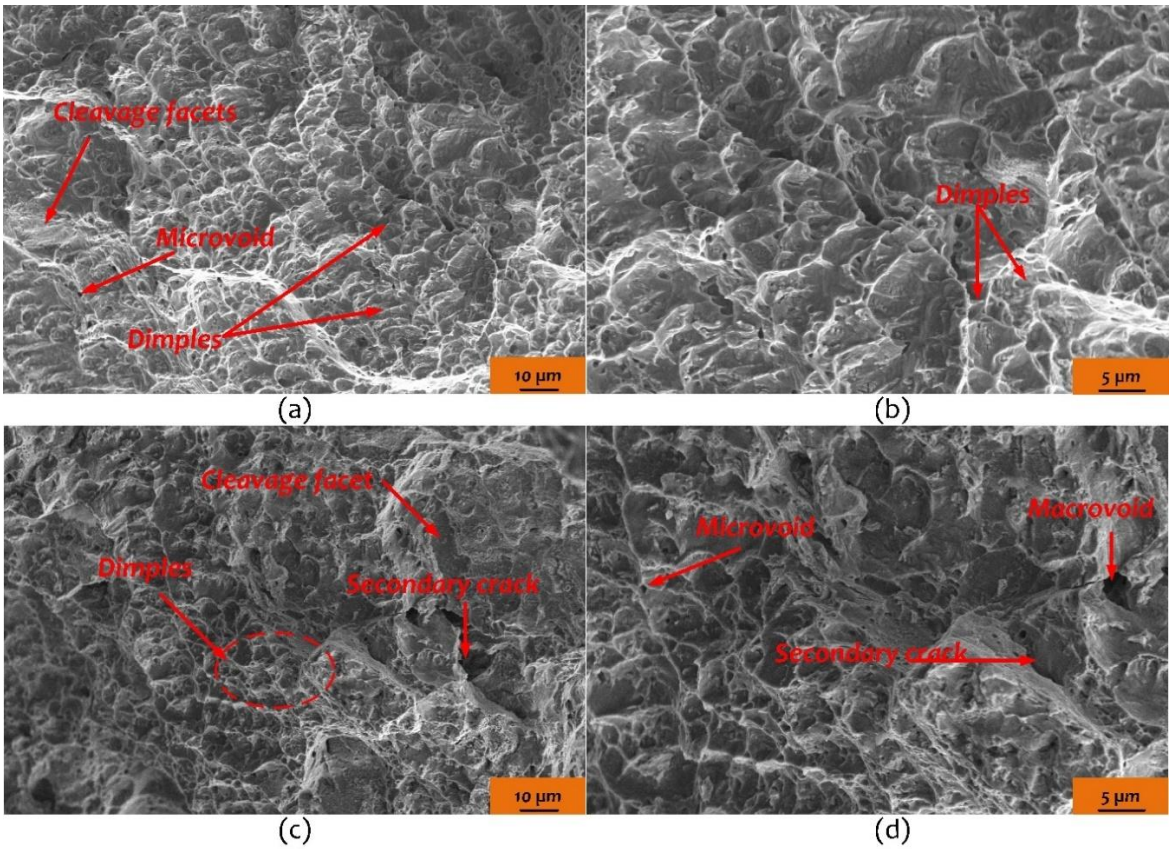


Figure 5.55 : (a) Fractured Charpy impact toughness specimens (a) fractured surface of AW specimen (b) fractured surface of AW specimen at higher magnification (c) fractured surface of PWHT specimen (d) fractured surface of PWHT specimen at a higher magnification

5.5 USING BUTTERING TECHNIQUE

Buttering in the GTAW technique affects steel weld strength differently. (Ramirez-Soto et al., 2019) discovered that welds without buttering differed from those with buttering. The welded joints with buttering had better corrosion resistance due to the formation of a passive layer of surface defects when exposed to alkaline conditions. (Shariatpanahi and Farhangi, 2009) reported that butter coating may improve the overall weld qualities, as the buttering width layer improved the tensile strength. Buttering with Inconel alloys is widely practiced in DWJs involving ferritic steels, as this technique minimizes the dilution effect. (Ghosh et al., 2015) argued that buttering material considerably affects weld strength and ductility. Buttering permits welding without weld heat treatment, according to (Das et al., 2009). Inconel 625 buttering layers were found to form brittle phases and carbides near the weld interface (Silva et al., 2022). These phases were highly prone to hydrogen embrittlement, which deteriorates the fracture toughness and ductility of the joint. During

high-temperature services, DWJs lack microstructural homogeneity and strength (Awale et al., 2020). (Rathod et al., 2016) studied the use of Ni-Fe alloy and Inconel 182 as buttering deposits on SA508 steel in nuclear power reactors. The study showed that buttering regulated carbon diffusion and reduced metallurgical deterioration. The Ni-Fe butter layer minimized carbon migration and metallurgical deterioration. The addition of the Inconel-182 buttering layer to ferritic-austenitic steel weld joints improved the mechanical properties and reduced base metal dilution. The buttering technique is ideal for joining metals with different expansion rates. Buttering the joint ensures a smooth composition and quality transition, ensuring its suitability. This method reduces cracking and strengthens the weld (Górka et al., 2024; Hwang et al., 2018). A buttering layer can be applied to material requiring post weld heat treatment (Ahmad et al., 2020; Olden et al., 2003).

5.5.1 Heat Affected Zone (HAZ) Microstructure Characterization

The HAZ of P91 steel welds is a critical region that experiences complex alterations in its microstructure due to the thermal cycles experienced during welding. By employing LOM and FESEM, the ICHAZ is analyzed to reveal different microstructural components (Figure 5.56(a)). Several phases were seen, such as untempered martensite, over-tempered martensite, and newly generated precipitates. The untempered martensite is identified as a rigid and fragile phase in the ICHAZ microstructure. The production of martensite in this location is a consequence of the partial re-austenitization and fast cooling that take place during the welding process. The ICHAZ exhibits diminished high-temperature yield and tensile strength when compared to the CGHAZ, FGHAZ, and base metal (Pandey et al., 2018a). Strain localization may have occurred in this location due to its unique microstructure and decreased strength (Kulkarni et al., 2020). This can render the P91 weldment highly susceptible, making it the most vulnerable component. Consequently, it may have led to the commencement of Type IV cracking over a prolonged duration of service (Paddea et al., 2012). Contrary to the ICHAZ, the FGHAZ of P91 steel, as shown in Figure 5.56(b) welds, exhibits a more consistent and improved tempered martensitic microstructure. During the thermal cycle of welding, the temperatures in this area are high enough to initiate the formation of austenite. This austenite subsequently undergoes rapid cooling and turns into a finely tempered martensite structure. The FGHAZ revealed an arrangement of tempered martensite laths and a notable abundance of carbide precipitates (Figure 5.56(b)). The examination of the CGHAZ reveals a uniform dispersion of large tempered martensite laths with a moderate quantity of carbide precipitates (Figure 5.56(c)). The primary phases discovered are $M_{23}C_6$ and MX-type carbonitrides, which bear resemblance to those present in the FGHAZ. The microstructure of the CGHAZ is characterized by larger tempered martensite laths and a lower density of precipitates compared to the FGHAZ. It has a coarse-grained nature. The CGHAZ has superior strength compared to other heat affected zones due to its large grain size and tempered martensitic structure, which effectively resists plastic deformation. The coarse microstructure also reduces the material's elongation capacity in comparison to the ICHAZ. The diverse changes in the microstructure across the various heat affected zones of P91 steel welds highlight the complex metallurgical transformations resulting from the welding process's thermal cycle. On the other side, the Incoloy 800HT HAZ (Figure 5.56(d)) region was very thin, and austenitic grain just adjacent to the weld interface was observed with a slight increase in grain size and precipitate coarsening from the energy dispersive x-ray spectroscopy (EDS) spectrum the matrix was found to be rich with Ti(C,N) cuboidal precipitates.

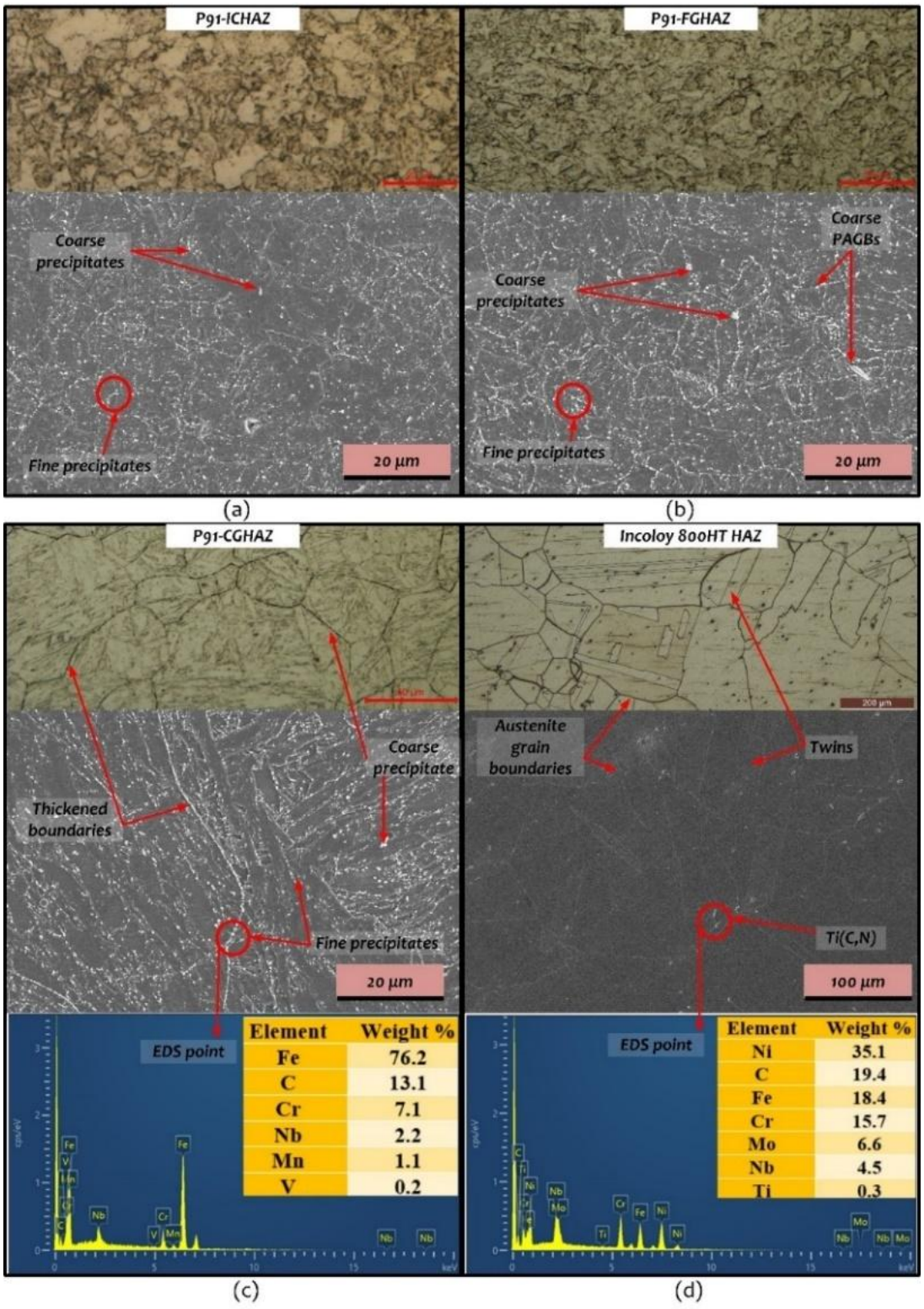


Figure 5.56 : Micrographs of (a) P91 ICHAZ (b) P91 FGHAZ (c) P91 CGHAZ with EDS spectrum (d) Incoloy 800HT HAZ with EDS spectrum

5.5.2 Weld Interface and Weld Fusion Zone (WFZ) Microstructure Characterization

Figure 5.57(a) depicts the WFZ microstructure, which consists of a dendritic structure. The WFZ was witnessed with cellular, columnar, and equiaxed dendrites. The distribution of these dendrite packets was homogenous and random. The packet boundaries were the SGBs, and the dendritic arm boundaries were the SSGBs. The buttering layers were clearly observed, as shown in Figure 5.57(b); the two different welding passes of the depositing buttering layer can be observed. The buttering layer region and WFZ both

showed an austenitic mode of solidification. The buttering region was dominant with columnar dendritic growth and cellular dendrites were also present. Figure 5.57(c) shows the macrograph of the weldment in which the weld bead geometry consisting of the buttering region and WFZ can be observed. Figure 5.57(d) shows the Incoloy 800HT weld interface with some macrosegregation features formed due to improper mixing of the base metal and WFZ. Similarly, Figure 5.57(e) shows the distinct interface between the WFZ and the buttering layer region with again some macrosegregation features, such as the formation of a peninsula. The P91weld interface shown in Figure 5.57(b) depicts the continuous weld interface without the formation of any unmixed zones. The elemental line mapping across the P91 weld interface and buttering layer/WFZ interface is shown in Figure 5.58(a), where variations of major alloying elements such as Fe, Ni, Cr, Co, Mn, and Mo can be clearly seen. However, no major diffusion of segregation of elements could be detected across either interface. The Incoloy 800HT weld interface (Figure 5.58(b)) also shows the major variation of certain elements across the weld interface due to obvious differences in the compositional elements such as Fe, Ni, Cr, Nb, and Co. The WFZ was characterized further, and the area mapping in Figure 5.59 shows the distribution of phases rich in Mo, Nb, C, Al, and Ti near the SGB. The phases were found to be randomly distributed in the WFZ. In Figure 5.60(a), the transmission electron microscopy (TEM) micrograph shows the SGB in WFZ decorated with C, Nb, and Ti-rich precipitates. Figure 5.60(b) shows a cuboidal precipitate in the WFZ, possibly TiC. The cuboidal particles were heavily surrounded by dislocations. The phases present in the solidified buttering layer region were found to be majorly rich in Ti, C, and possibly Nb, as shown in Figure 5.61, where precipitates were accumulated on the SGB.

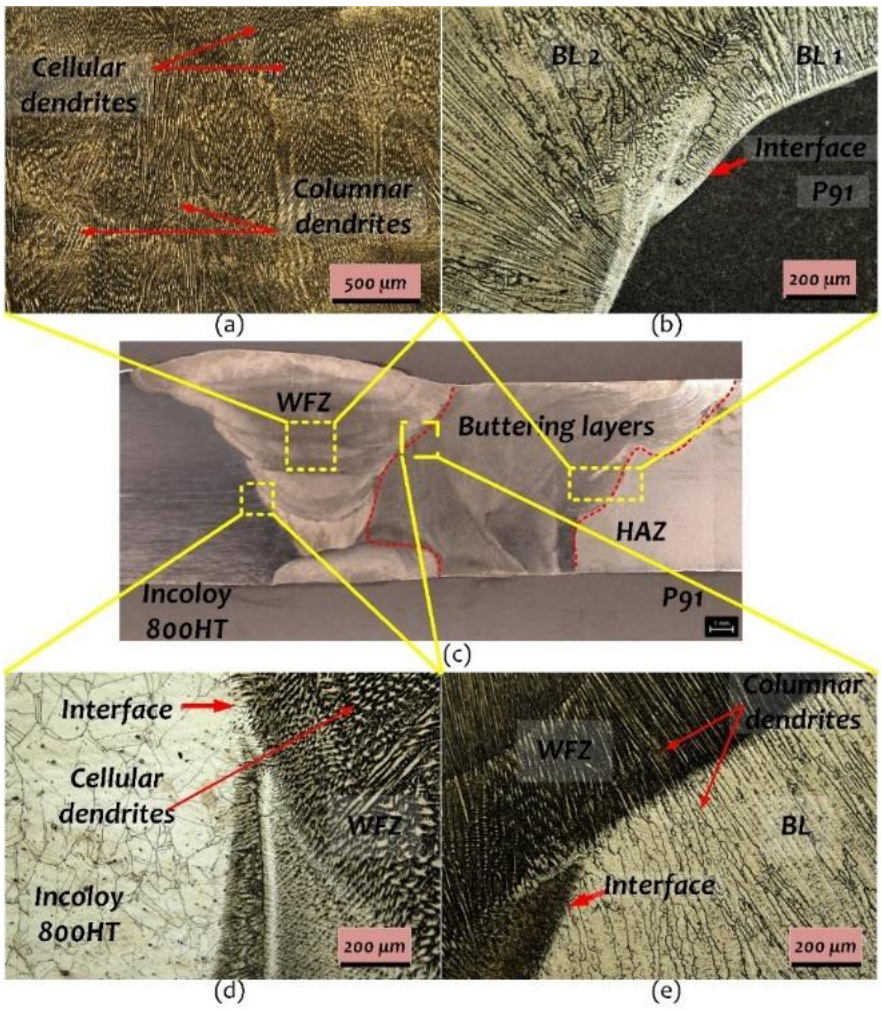


Figure 5.57 : Optical micrograph of (a) WFZ (b) P91 weld interface with buttering layers (c) weld bead macrograph (d) Incoloy 800HT weld interface with WFZ (e) WFZ and buttering interface

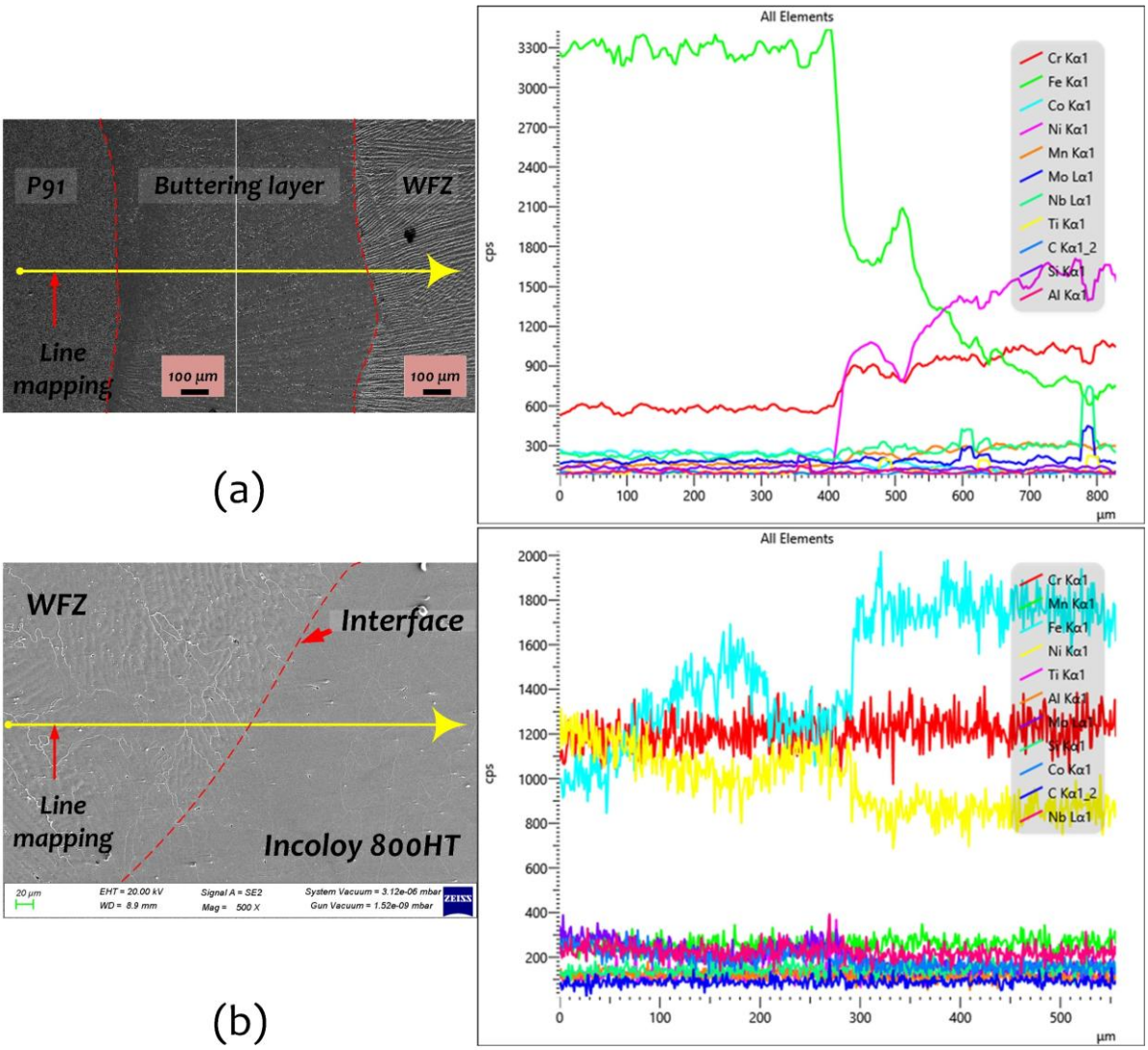


Figure 5.58 : (a) FESEM micrograph of P91 weld interface with line mapping spectrum across the two different interfaces (b) FESEM micrograph of Incoloy 800HT weld interface with line mapping spectrum across the interface

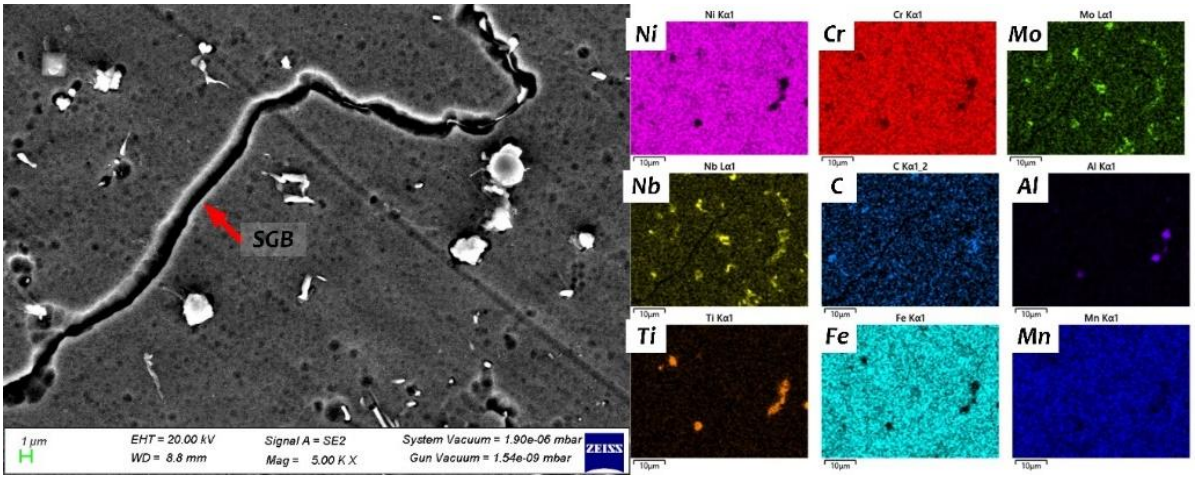


Figure 5.59 : FESEM micrograph of WFZ with area mapping

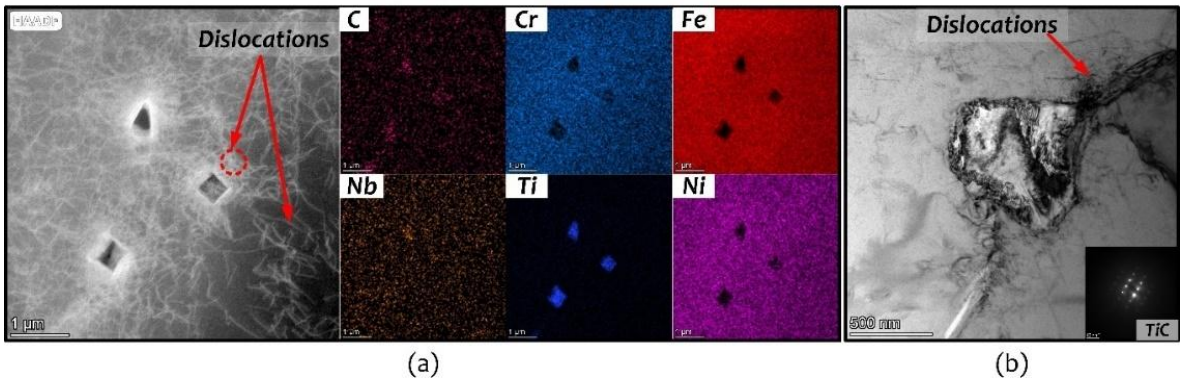


Figure 5.60 : (a) TEM micrograph of WFZ with area mapping (b) TiC precipitate

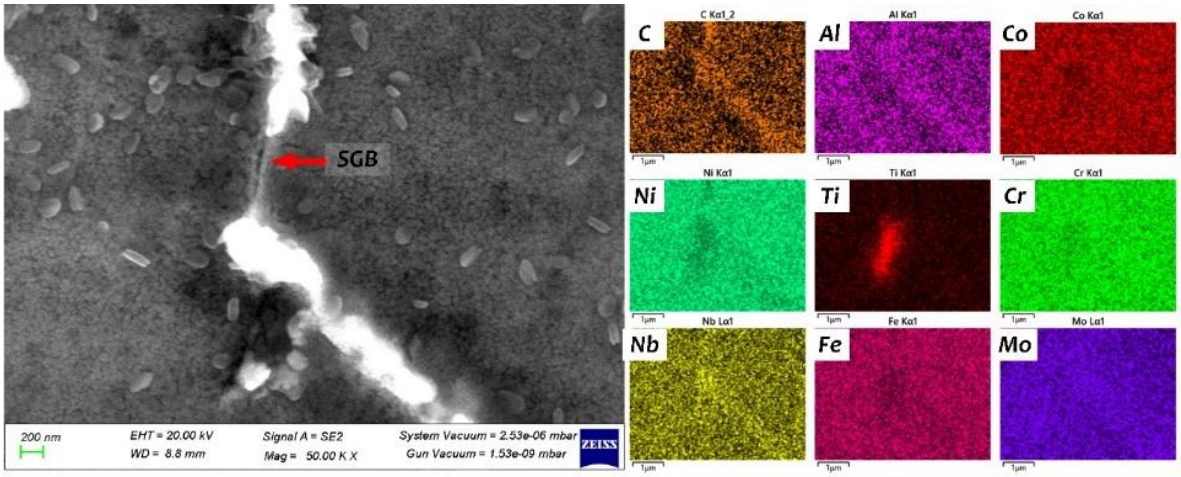


Figure 5.61 : FESEM micrograph of the SGB observed in the buttering region with area mapping

5.5.3 Electron Backscatter Diffraction (EBSD) Analysis

The DWJ was further characterized through the EBSD technique. The Incoloy 800HT HAZ region adjacent to the Incoloy 800HT weld interface had stable austenitic microstructure, as no overall change in the austenitic grain was observed in the HAZ region. From the EBSD scans, the IPF map in Figure 5.52(a) shows random orientations of the grain in the Incoloy 800HT HAZ region. Also, the dendritic packets in the WFZ near the Incoloy 800HT weld interface were arranged in random orientation, also suggesting extensive growth of the austenitic grain in some areas of the weld interface. In the grain boundary map in Figure 5.52(b), it is necessary to observe that the significant grain boundaries are high-angle grain boundaries (HAGBs) both in the HAZ region and the WFZ region near the Incoloy 800HT weld interface. HAGBs are familiar to alloys with composition including nickel, chromium, and iron as they have a strong affinity for a specific crystallographic orientation, which leads to preferential formation of HAGBs during solidification and processing of Incoloy and Inconel alloys. Though HAGBs may act as barriers to grain boundary migration and recrystallization process, they might also promote segregation of microalloying elements. Figure 5.52(c) shows the kernel average misorientation (KAM) map, which depicts the presence of dislocation debris in the HAZ grains and grain boundaries, which may be due to the segregation of some microalloying elements such as Ti, C, Nb, and Mo. The phase map in Figure 5.52(d) shows the complete presence of the fcc phase while a very minor fraction of precipitates is bcc. Figure 5.52(e) shows the grain orientation spread (GOS) map, which hints at the formation of recrystallized grain in the Incoloy 800HT HAZ region near the WFZ due to the accumulation of dislocation and plastic deformation during the solidification of the WFZ. It was observed that columnar grains were growing from the

Incoloy 800HT HAZ grain at the interface without any interruptions and had a preferred orientation at the interface. This is because of the competitive mechanism of grain growth, where grains the preferably orientated along the thermal gradient to grow rapidly. As a result, fcc grain in the WFZ at the weld interface shows <001> growth direction (Figure 5.52(f)) nearly parallel to the flow direction gradient of the heat. The WFZ has the dominant presence of HAGBs (Figure 5.52(g)). The KAM map (Figure 5.52(h)) for WFZ shows the presence of dislocation in the matrix distributed in some regions, which could be formed with the deposition of consequent welding passes leading to uneven solidification of the WFZ. Further, in Figure 5.52(i), WFZ shows the complete FCC phase presence. The GOS map for the WFZ in Figure 5.52(j) hints at the recrystallization of a few grains near the interface of the consecutive welding pass deposited during welding. Further the EBSD analysis was also performed for the WFZ/BL interface region. Figure 5.52(k) depicts the random orientation of grain packets across the interface. The HAGBs were dominant in Figure 5.52(l) for the interface region, with the presence of medium angle grain boundaries (MAGB) in some grain packets. Figure 5.52(m) shows the presence of dislocation distributed along a certain region uniformly. The WFZ/BL interface region was dominantly FCC, as shown in Figure 5.52(n). The GOS map (Figure 5.52(o)) for the WFZ/BL interface region again shows the recrystallization of a low fraction of grains near the interface.

Figure 5.52(p) shows an inverse pole figure (IPF) showing a random orientation of grains in the HAZ region, while in the WFZ, dendrites have grown into packets, and individual packets seem to have a preferred average grain orientation of <001>. The grain boundary map in Figure 5.52(q) shows the presence of low angle grain boundaries 1˚-5˚ (LAGBs), 5˚-10˚ MAGBs, and 15˚-180˚ HAGBs. The P91 HAZ region dominant the presence of LAGBs and then HAGBs. HAGBs have resulted from the grain growth in the CGHAZ region and the dissolution of Cr-rich precipitates. The major presence of LAGBs assures the mechanical performance of the DWJ. The KAM map in Figure 5.52(r) again shows the presence of the high dislocation density in the P91 HAZ region due to thermal stresses experienced during welding. These dislocations in the HAZ region tend to interact with each other, forming a network with the grains and leading to changes in mechanical properties, such as an increase in the microhardness of the region. The phase map (Figure 5.52(s)) shows WFZ near the P91 weld interface being completely fcc due to the austenitic mode of solidification, with a minor presence in the P91 HAZ region just near the interface due to the formation of minor unmixed zones. The presence of HAGB near the weld interface also infers that the formation of migrated grain boundaries (MGBs) may have originated from a parent solidified grain boundary in the WFZ. The GOS map in Figure 5.52(t) shows the presence of recrystallized grain packets in the WFZ region adjacent to the P91 weld interface. This could be due to the occurrence of heavy plastic deformation during solidification and phase transformation near the weld interface, which could have led to the accumulation of dislocations in the region.

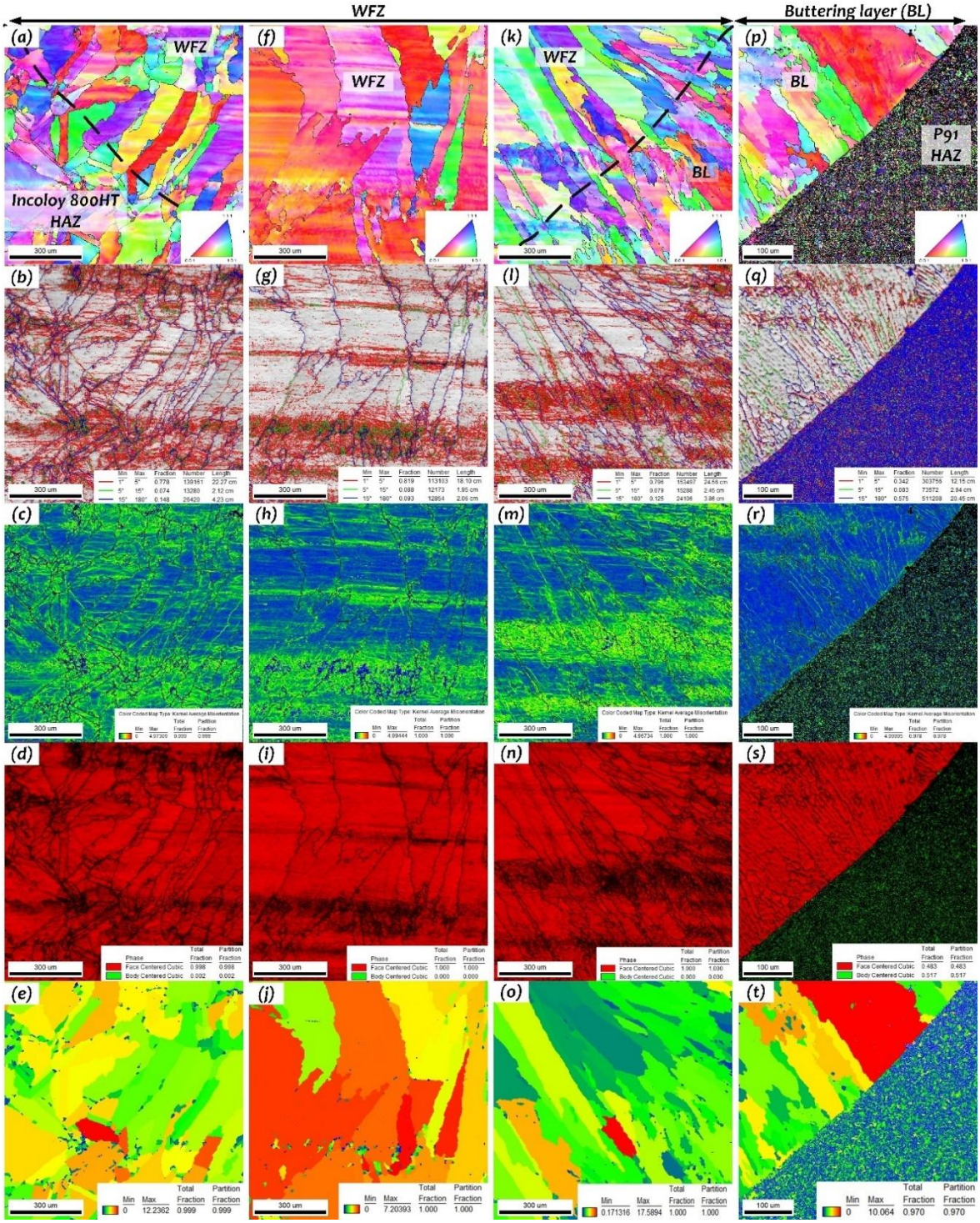


Figure 5.62 : Incoloy 800HT weld interface (a) IPF map (b) IQ+grain boundary map (c) KAM map (d) phase map (e) GOS map; WFZ/buttering interface region (f) IPF map (g) IQ+grain boundary map (h) KAM map (i) phase map (j) GOS map; WFZ (k) IPF map (l) IQ+grain boundary map (m) KAM map (n) phase map (o) GOS map; P91 weld interface (p) IPF map (q) IQ+grain boundary map (r) KAM map (s) phase map (t) GOS map

5.5.4 Tensile Properties

Tensile tests were conducted on specimens manufactured according to the American Society for Testing and Materials (ASTM) A370 standards (ASTM, 2014) for both room-temperature and high-temperature conditions. The specimens were prepared as per the schematic in Figure 5.63(a), where standard specimens for room temperature tensile testing were prepared such that for one specimen, WFZ was kept at the center of the gauge length,

and for the others, the buttering layer region was kept at the center. Figure 5.63(b) also shows the specimens in a fractured state after the testing. Table 5.9 provides a concise overview of the tensile properties observed throughout the conducted tests. The flat AW standard BL-1 specimen experienced failure at the weakest point of the DWJ, specifically the Incoloy 800HT base metal side. The ultimate tensile strength (UTS) of the AW standard BL-1 specimen was measured to be 671 ± 5 MPa. The BL-2 AW specimen experienced failure from the WFZ, exhibiting an impressive ultimate tensile strength (UTS) of 458 ± 5 MPa. The specimens were examined with elongation measurements of 34% and 19% respectively. The high-temperature tests were conducted to examine the behavior of DWJ at increased temperatures. During the tests conducted at a temperature of 650℃, failure was observed from the P91 base metal side. The primary cause of this failure was determined to be the restricted working temperature range of the P91 material. The specimen tested at a temperature of 650℃ exhibited a UTS of 151 ± 5 MPa and an elongation of 27 ± 2%. The reduction in strength is attributed to the softening influence of the over-tempered martensite and the non-uniformity of the microstructure. The enhanced ductility is a result of the softened, over-tempered martensite and the incorporation of freshly generated precipitates. Precipitates can impede the movement of dislocations and improve the material's ability to undergo plastic deformation. Having a comprehensive comprehension of the local metallurgical changes resulting from the welding thermal cycle is of utmost importance, as demonstrated by the intricate microstructure and fluctuations in mechanical properties inside the martensite. The reason for this is the existence of finely-grained tempered martensite and a high concentration of precipitates, which effectively impede the motion of dislocations and boost the material's capacity to withstand plastic deformation. At a temperature of 550℃, the round high-temperature specimen experienced failure from the Incoloy 800HT side, resulting in an ultimate tensile strength (UTS) of 340 ± 5 MPa and elongation of 43 ± 2%. Both specimens subjected to high temperatures exhibited the flow stress anomaly (Hagihara et al., 2003). At high temperatures, micro-alloying elements like Cr tend to concentrate along dissociated dislocations in order to reduce the stacking fault energy. The matrix's low stacking fault energy enables the onset of deformation twins at elevated temperatures. At a temperature of 550℃, serrations of Type B were found. Type B serrations refer to the occurrence where the motion of dislocations is impeded, leading to a reduction in flow stress when the dislocations become unpinned (Liu et al., 2022). At a temperature of 650℃, the specimen had serrations of Type A. The serrations seen were a consequence of regular deformations occurring over the gauge length of the specimen, leading to the production of Type A serrations that exhibit locking behavior (Liu et al., 2022). Figure 5.64 displays the engineering stress-strain curves of the tested specimens. Figure 5.65(a) displays the fracture surface of the flat AW standard BL-1 specimen in the fractography analysis, exhibiting the presence of dimples and voids. The specimen exhibits full ductile behavior, which is also evident from the cracked surface. The BL-2 specimen with a flat AW configuration (as shown in Figure 5.65(b)) exhibits a fracture that is a combination of both ductile and brittle fractures, with ductile fracture being the predominant mode (Mittal and Sidhu, 2015). Additionally, it was noted that cleavage facets were present. The brittleness of the material may be attributed to the concentration of stress around any secondary phases that have formed in the WFZ. These secondary phases could have acted as nucleation sites for the formation of microcracks. At a temperature of 550℃ (Figure 5.65(c)), the failure surface of Incoloy 800HT specimens with a round shape exhibits a mix of failure modes, with ductile failure being the dominant one. At high temperatures, the Incoloy 800HT matrix exhibited the formation of small-sized precipitates. Additionally, the coarsening of secondary phases in the matrix facilitated the propagation of cracks along the crystal lattice's weak planes. At a temperature of 650℃ (as shown in Figure 5.65(d)), a cup-cone-type failure surface was seen, indicating the occurrence of ductile failure from the P91 side. The P91 is known to undergo carbide precipitation at both the grain boundaries and matrix at this temperature. As a result, there is an increase in grain size and migration of the

grain boundaries. Moreover, as grain size increases due to coarsening, grain boundaries serve as sites where void formation is initiated. Comparable findings were documented while employing the buttering P92-IN 617 buttering welds, as the ultimate tensile strength (UTS) of the weld fusion zone (WFZ) exhibited a notable increase (Kumar et al., 2024).

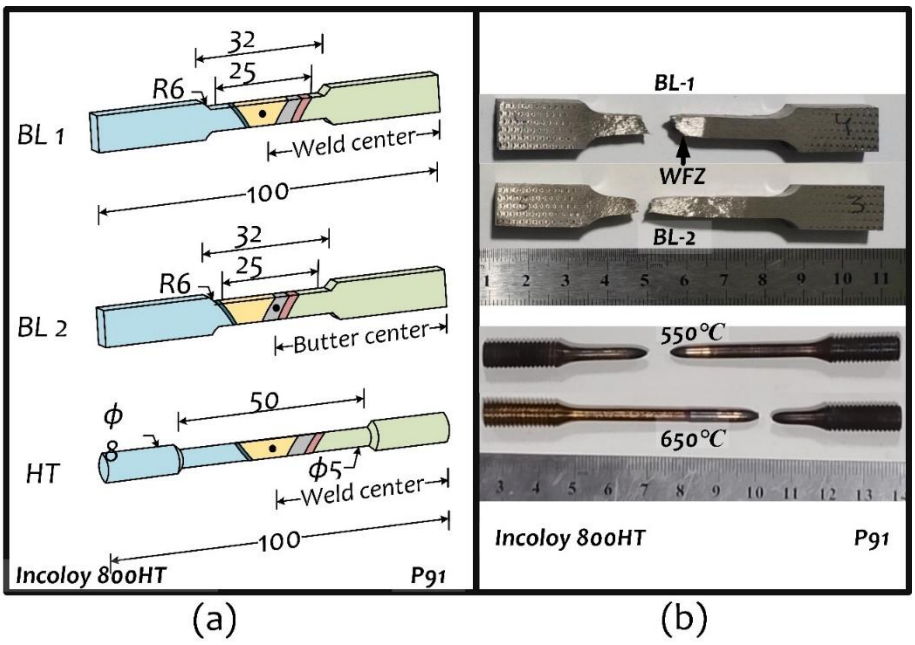


Figure 5.63 : (a) Schematics of the specimens prepared (b) fractured specimens

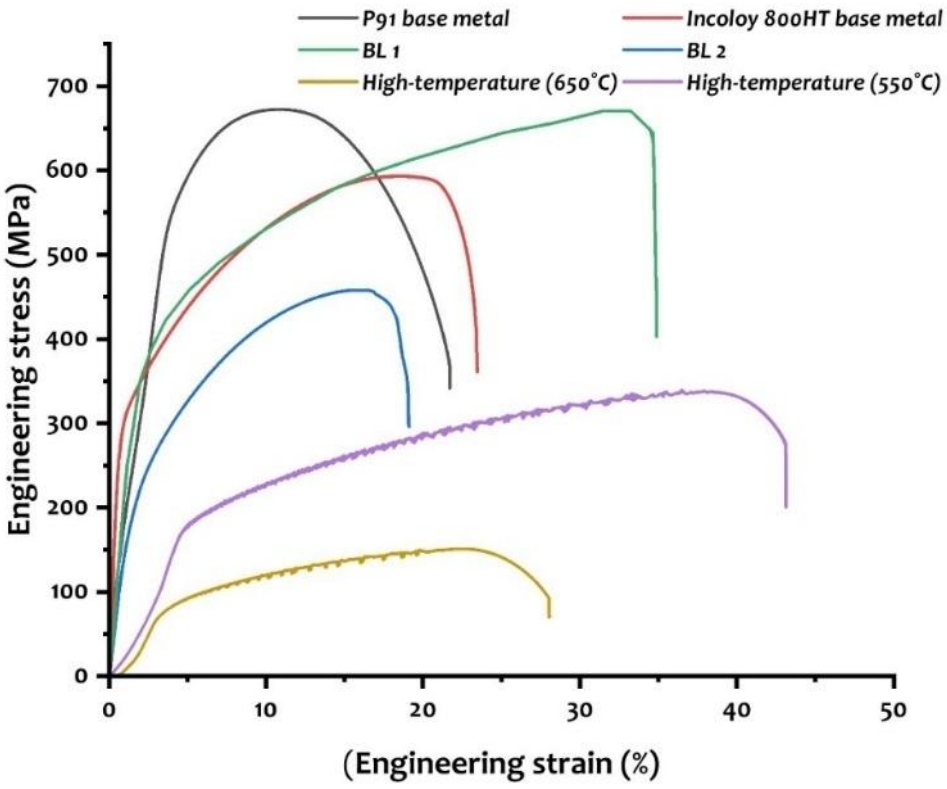


Figure 5.64 Engineering stress-strain curves for tested tensile specimens

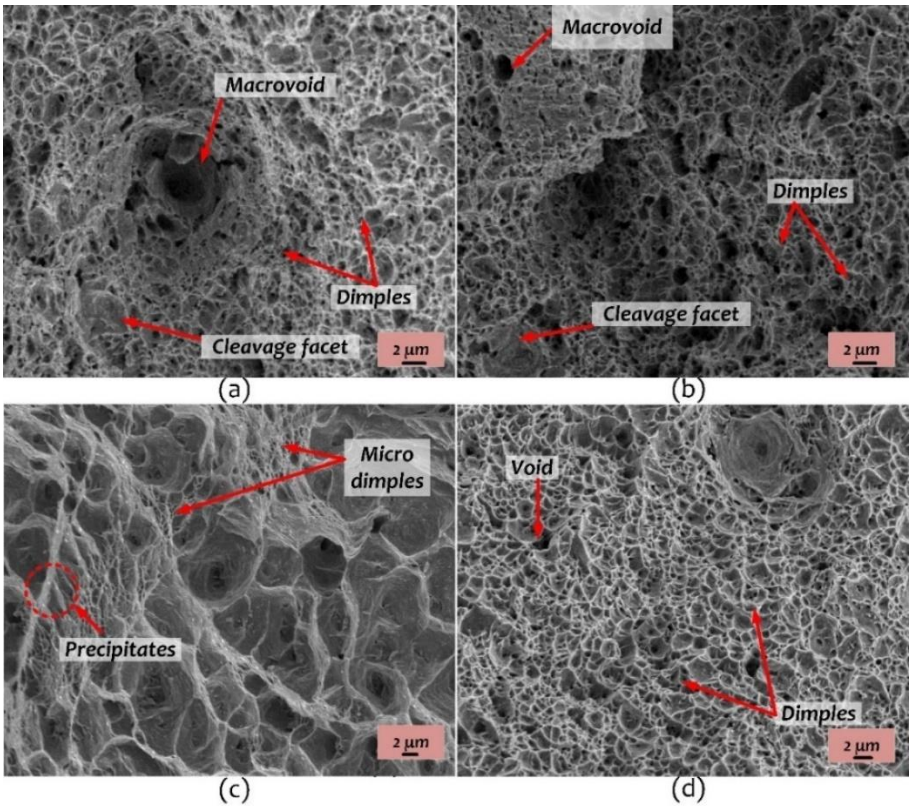


Figure 5.65 : Fractography micrograph of (a) BL-1 specimen fractured surface (b) BL-2 specimen fractured surface (c) HT (550°C) specimen fractured surface (d) HT (650°C) specimen fractured surface

Table 5.9 : Tensile properties observed for different specimens

Specimens	*UTS (MPa)*	*Elongation (%)*	*Reduction in the area (%)*	*Failure site*
BL 1 (weld centered)	671 ± 5	34 ± 2	24 ± 2	Incoloy 800HT base metal
BL 2 (Butter layer centered)	458 ± 5	19 ± 2	21 ± 3	WFZ
High-temperature (650°C)	151 ± 5	27 ± 2	47 ± 3	P91 base metal
High-temperature (550°C)	340 ± 5	43 ± 3	39 ± 3	Incoloy 800HT base metal

5.5.5 Microhardness Properties

The Vickers microhardness tests were conducted along the weldment of the DWJ. The indents were measured with a 0.5 mm spacing and at 0.5 kgf load, as seen in the schematic diagram presented in Figure 5.66. Furthermore, a notable disparity in the microhardness was observed in the P91 HAZ of the DWJ. The highest microhardness of 279 HV was observed in the CGHAZ region, while the lowest microhardness of 220 HV was recorded in the ICHAZ zone. The region in P91 HAZ, known as FGHAZ, exhibited an average microhardness of 235 ± 10 HV. The WFZ had an average microhardness of 246 ± 10 HV. The highest recorded value of 260 HV was reported near the center of the WFZ. The buttering layer region has an average of 239 HV. The Incoloy 800HT HAZ exhibited a consistent microstructure, resulting in an average microhardness variation of 179 ± 10 HV throughout the region. This is comparable to the average microhardness of 170 ± 10HV recorded on the 800HT base metal side. The CGHAZ in the P91 HAZ exhibited elevated microhardness levels because of the creation of untempered martensite, but as anticipated because of tempering from the buttering process, a certain level of homogeneity was achieved (Kumar et al., 2024; Tomków et al., 2020). The ICHAZ drop occurred because of the

presence of excessively heat-treated martensite in the area. The exposure to the elevated temperatures during the deposition of multiple weld layers in the buttering and welding process has helped in homogenizing the microhardness variation up to a certain extent. However, compared with the results obtained from a dedicated PWHT for the DWJ, PWHT in the buttering technique can still be suggested. The WFZ also experiences an unusual variation in microhardness near its center, perhaps caused by the development of secondary phases in the dendritic cores. In comparison to traditional welding procedures, the buttering technique resulted in less significant fluctuation in microhardness in the HAZ region. The peak microhardness observed in the CGHAZ region was also significantly lower, complete homogeneity was not observed, and the effect of post weld heat treatment in the buttering technique could still be explored.

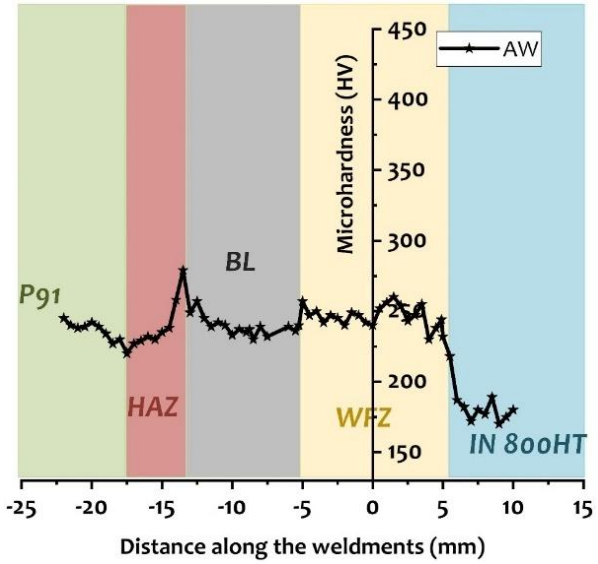


Figure 5.66 : Microhardness variation plot for the P91 and Incoloy 800HT DWJ

5.5.6 Charpy Impact Toughness

The specimens in as-welded (AW) condition were prepared for the Charpy impact toughness testing at room temperature. The V-notch was machined in the specimens as per the schematic shown in Figure 5.67(a). The specimens were prepared according to the ASTM A370 standard. Furthermore, Figure 5.67(b) displays the fractured samples following the impact. The AW specimen was found to have undergone a ductile failure process, as evidenced by the presence of shear lips and lateral expansion. The fracture propagated entirely along the WFZ or buttering region. The BL-1 specimen exhibited a Charpy impact toughness rating of 98 ± 5 J. The BL-2 specimen also showed a highly ductile mode of fracture with a Charpy impact toughness rating of 88 ± 5 J. This indicates that the DWJ between P91 and Incoloy 800HT exhibited a notable Charpy impact toughness that exceeded the established toughness norms. The fractography analysis of the WFZ fractured surface revealed a hybrid failure mode, as shown in Figure 5.67(c). The same was observed for the other specimen (Figure 5.67(d)), where ductile dominant behavior was reflected due to the presence of lateral contraction and dimples. While the presence of cleavage facets confirms the hybrid failure mode on impact. The results align with the observations made for a comparable DWJ, where the same filler and buttering technique gave similar results (Singh and Arora, 2022). The high Charpy impact toughness and predominant ductile behavior were attributed to the development of an austenitic structure and the presence of several slip systems in the face centered cubic (fcc) phase observed in the WFZ.

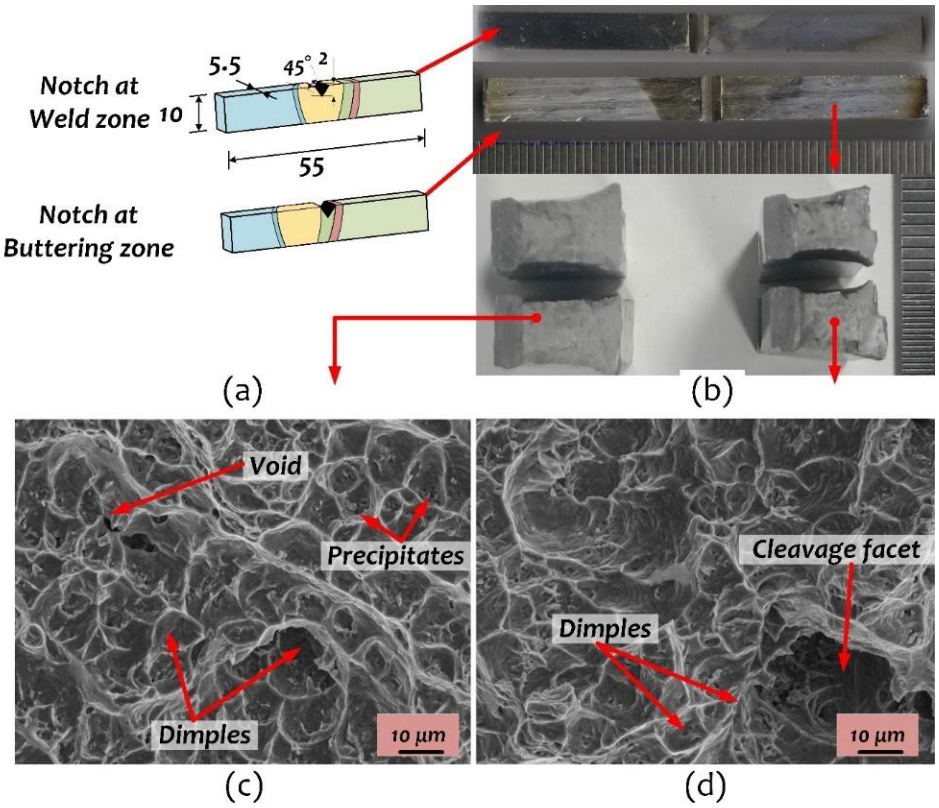


Figure 5.67 : (a)Schematics of Charpy impact toughness specimens prepared (b) V-notch specimens after fracture (c) micrographs of specimen failed from the WFZ (d) micrographs of specimen failed from the buttering region